NASA Technical Memorandum 81728

Combustion of Solid Carbon Rods in Zero and Normal Gravity

Charles M. Spuckler
Lewis Research Center
Cleveland, Ohio

May 1981

NASA

TABLE OF CONTENTS

NOMENCLATURE

A	proportionality factor in Table 1
a	constant in Table 1
B	constant in Table 1
B_1	constant in Table 1
B_2	constant in Table 1
C_i	molar concentration of species i
c	constant in Table 1
c_1	constant in Table 1
c_2	constant in Table 1
c_p	specific heat of mixture
D	effective binary diffusivity or diffusivity in Table 1
$D_{CO_2-N_2}$	diffusivity of CO_2 through N_2 at 273° K in Table 1
$D_{O_2-N_2}$	diffusivity of O_2 through N_2 at 273° K in Table 1
D_i	effective binary diffusivity or diffusivity at 273° K in Table 1
D_{ij}	effective binary diffusivity
d	diameter
E	activation energy
E_A	activation energy for absorption in Table 1
E_D	activation energy for desorption in Table 1
f	steric factor
H_{CO}	heat of combustion of two moles of carbon monoxide

H_{CO_2}	heat required for one mole of carbon dioxide to react with carbon to produce carbon monoxide
H_{O_2}	heat evolved by one mole of oxygen reacting with carbon to produce carbon monoxide
J_c	molar specific combustion rate
$\bar{k}$	pre-exponential factor
k_1	reaction coefficient
k_i	reaction rate constant for species i
k_g	pre-exponential factor for gas phase reaction
M_C	molecular weight of carbon
M_i	molecular weight of species i
$\dot{m}$	constant defined in equation (1)
$\dot{m}_o$	mass combustion rate
$\dot{m}_1$	specific mass combustion rate
n	micromoles of gas impinging on unit surface in Table 1
n_{ir}	mass flux of species i in the radial direction
P	total pressure
P_{N_2}	partial pressure of nitrogen in ambient gas
P_n	partial pressure of inert
P_{O_2}	partial pressure of oxygen
Pr	Prandtl number
q'	heat generated by combustion of carbon monoxide
R	universal gas constant
R_i	gas phase mass reaction rate of species i
Re	Reynolds number
$\mathscr{R}_{CO}$	gas phase molar reaction rate of carbon monoxide

$\mathscr{R}_{CO_{2S}}$	surface molar reaction rate of carbon dioxide
$\mathscr{R}_{O_{2S}}$	surface molar reaction rate of oxygen
r	radial distance from center of rod or sphere
T	temperature
T_m	average temperature
T_o	273° K
t	time
u	free stream axial velocity
v	radial velocity
X_i	mole fraction of species i
Y_i	mass fraction of species i
δ	film thickness
λ	thermal conductivity
ρ	density or total mass concentration
ρ_i	mass concentration of species i
τ	nondimensional temperature
ϕ_1	mechanism factor 1 if CO_2 formed, 2 if CO formed

Subscripts:

b	at the edge of the stagnant film or ambient gas
i	CO, CO_2, or O_2
S	surface

COMBUSTION OF SOLID CARBON RODS IN ZERO AND NORMAL GRAVITY

Charles M. Spuckler

National Aeronautics and Space Administration

Lewis Research Center

Cleveland, Ohio 44135

I. INTRODUCTION

In recent years, a new emphasis has been placed on research involving the production of energy from new or existing sources. One of in areas of interest is solid combustion oriented toward an understanding of the true mechanisms involved in the combustion of coal. The chemical and physical processes involved in the combustion of a solid depend in part on the nature of the solid. Many solids burn in a manner similar to liquid fuels, in that the surface of the solid sublimates and the burning takes place away from the surface in a flame zone surrounding the solid. Other solids burn with a surface reaction. If the surface reaction results in complete combustion, no flame zone will appear but the surface will glow. If combustable gases are formed by the surface reaction, they can burn in a gas phase reaction producing a flame zone away from the surface.

Combustion of carbonaceous solids, such as coal, is complex because it takes place in two stages. The coal first pyrolyzes on being heated, with the volatile gases being driven from the solid through pores and cracks to the outside environment where they mix with oxygen and burn via a gas phase reaction. After all volatiles have been driven off, mainly solid carbon remains, which then burns via reactions on the surface and in the pores. During this latter process, various chemical reactions can occur. The carbon surface reacts with oxygen to form either carbon monoxide, carbon dioxide, or a combination of both. If carbon monoxide is formed at the surface, a gas phase reaction of the carbon monoxide with oxygen to form carbon dioxide is possible.

To gain a better understanding of the mechanism of coal combustion, it was decided that the process by which carbon ignites and burns should be examined. If the carbon combustion process can be understood, the results should aid in the analysis of the larger problem of coal combustion.

In this study, zero and normal gravity experiments were conducted to determine the correct combustion model for carbon burning supported only by its own combustion. Species concentration profiles were measured to determine the mechanism controlling the process and the primary products of combustion. The zero and normal gravity data were then compared to ascertain the effects of free convection.

II. LITERATURE SURVEY

A. General Discussion

The term heterogeneous combustion is applied to any combustion process in which a fuel in the condensed phase is burned. This definition covers the following combustion processes (1) tne fuel is vaporized at the surface and the chemical reaction occurs in the gaseous phase; and (2) the chemical reaction occurs on the surface of the condensed phase with possible secondary reactions occurring in the gaseous phase. Liquids and some solid fuels fall into the first category. The fuel is vaporized at the surface and moves outward, meeting oxygen which is moving inward toward the surface, with the combustion occurring in the gas phase away from the surface. For ease of solving this problem analytically, the chemical reactions in the gas phase are generally assumed to occur infinitely fast, so that analytically the combustion occurs in a very thin flame sheet. The products of combustion move both inward toward the fuel surface and outward from the flame zone. Some of the heat produced by the reaction is transferred to the surface where it vaporizes more fuel, while the rest of the heat is transferred away. A schematic of the process is shown in Figure 1.

For solids which fall into the second category, the combustion process consists of oxygen first being transferred to the surface,

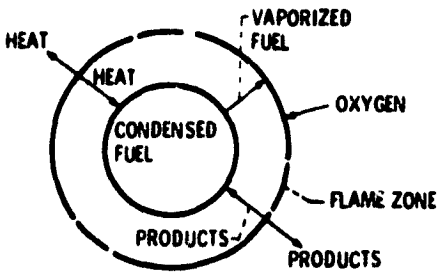

Figure 1. - Schematic of heterogeneous combustion.

where it is chemisorbed and where it reacts with the fuel. The products are then desorbed and move away from the surface. If the chemisorption, the surface reaction, and the desorption processes are lumped into one overall chemical process, solid combustion can be said to consist of a mass transfer process and a chemical process.

Carbon is one of the solids that burns with a surface reaction and, therefore, falls into the second category. Various models for carbon combustion have been proposed. The products of combustion and the mechanism of the combustion process depend upon the carbon surface temperature.

B. Theoretical Analysis

The various models proposed for carbon combustion can be classified as a low temperature model, a mid-temperature model, and a high temperature model. Most of the models found in the literature are for a quiesent atmosphere and neglect buoyancy effects.

At low surface temperatures, below approximately 500° C, carbon is oxidized at the surface to carbon dioxide through the reaction $C + O_2 \rightarrow CO_2$. This model along with the assumed concentration and temperature profiles is presented in Figure 2. Fendell [1] presents a general solution for this model along with limiting solutions for mass transfer control and chemical process control. Also, solutions for equilibrium and nonequilibrium reactions at the surface are presented.

At moderate temperatures, between 500° C and 1100° C, a complex reaction takes place in which both carbon dioxide and carbon monoxide are formed at the surface through two surface reactions, $C + O_2 \rightarrow$

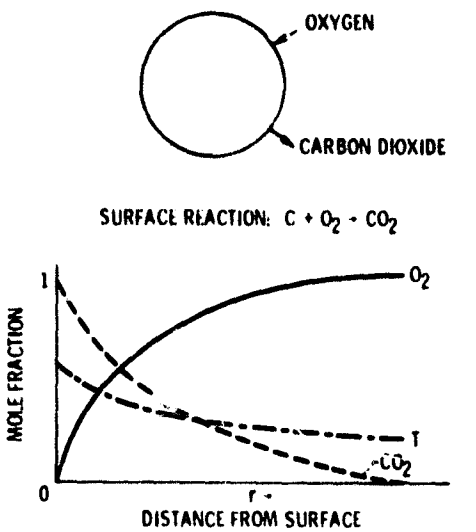

Figure 2. - Low temperature model. ($T_s < 500^0$ C.)

CO_2 and $2C + O_2 \rightarrow 2CO$. There is no oxidation of carbon monoxide in the gas phase. There is no known theoretical analysis of this model, which is illustrated in Figure 3.

For high surface temperatures, above 1100° C, four high temperature models have been proposed. Ubhayahar and Williams [2, 3] proposed a model in which oxygen reacts with carbon at the surface to form carbon monoxide through the reaction $2C + O_2 \rightarrow 2CO$, with no further reaction of carbon monoxide occurring in the gas phase. This model is based on extinction experiments in which carbon particles were burned in oxygen, and oxygen and nitrogen mixtures. In their theoretical analysis, atomic oxygen in equilibrium with molecular oxygen or just molecular oxygen reacting at the surface were considered. This model, neglecting the dissociation of oxygen, is presented in Figure 4a.

Fendell [1] proposed a complex high temperature model in which two surface reactions take place. Carbon is oxidized to carbon monoxide through the reaction $2C + O_2 \rightarrow 2CO$, and ambient carbon dioxide is reduced to carbon monoxide through the reaction $CO_2 + C \rightarrow 2CO$. There is no gas phase oxidation of carbon monoxide. Fendell presents the general solution along with the limiting solutions of mass transfer control and chemical process control. This model is presented in Figure 4b. A third high temperature model has been proposed. In this model carbon monoxide is formed at the surface through two surface reactions, $C + CO_2 \rightarrow 2CO$ and $2C + O_2 \rightarrow 2CO$. The carbon monoxide is then burned to carbon dioxide through the homogeneous gas phase reaction, $2CO + O_2 \rightarrow 2CO_2$. This model is presented in Figure 4c. Hugo, Wicke, and Wurzbacher [4] obtained an approximate solution for a

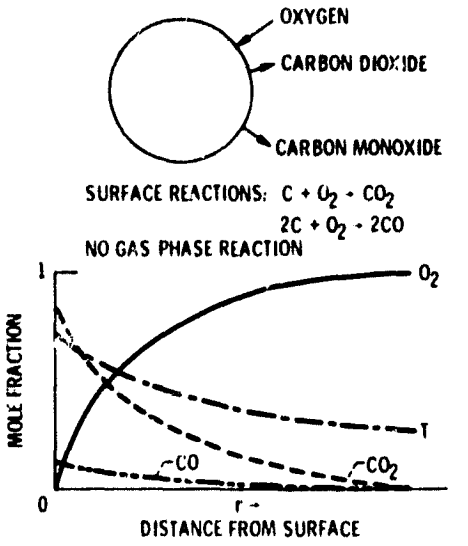

Figure 3. - Mid temperature model. (500^{0} C < T_s < 1100^{0} C.)

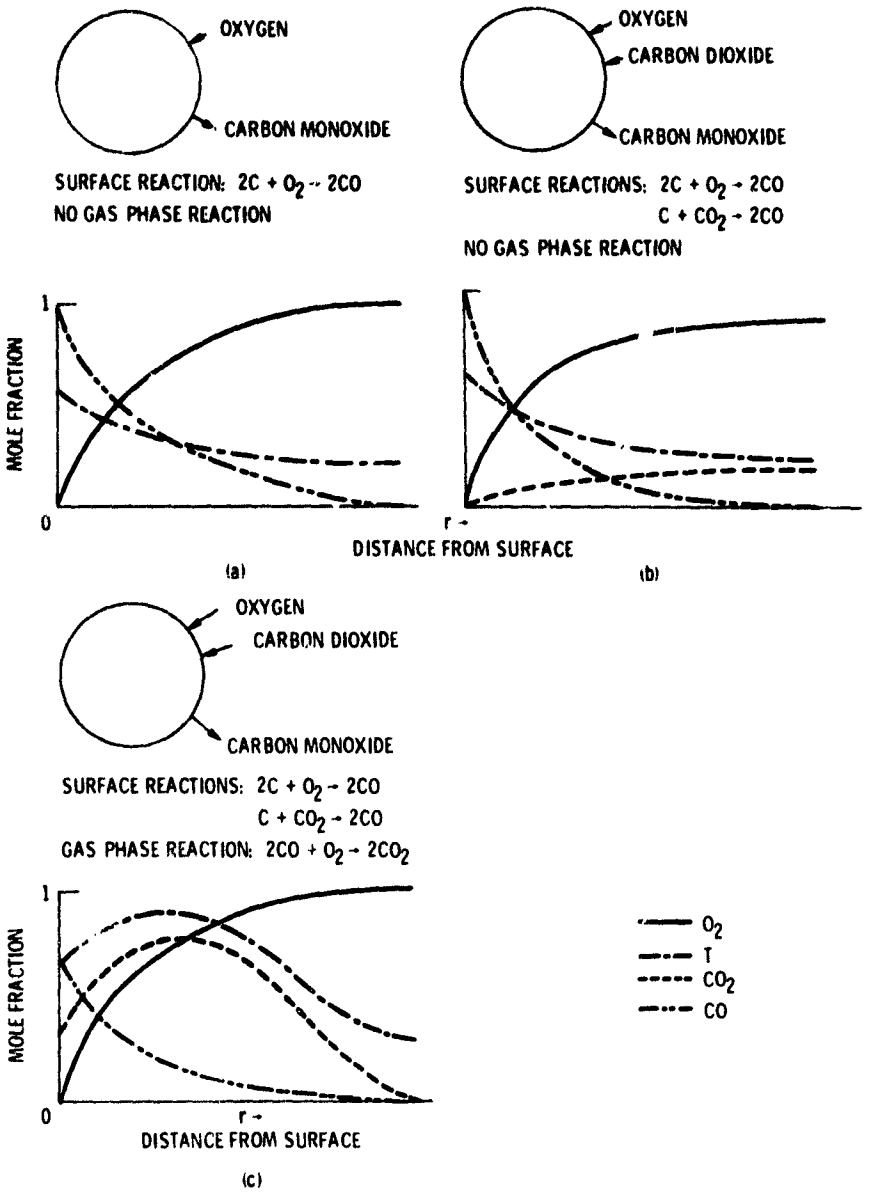

Figure 4. - High temperature models. ($T_s > 1100^0$ C.)

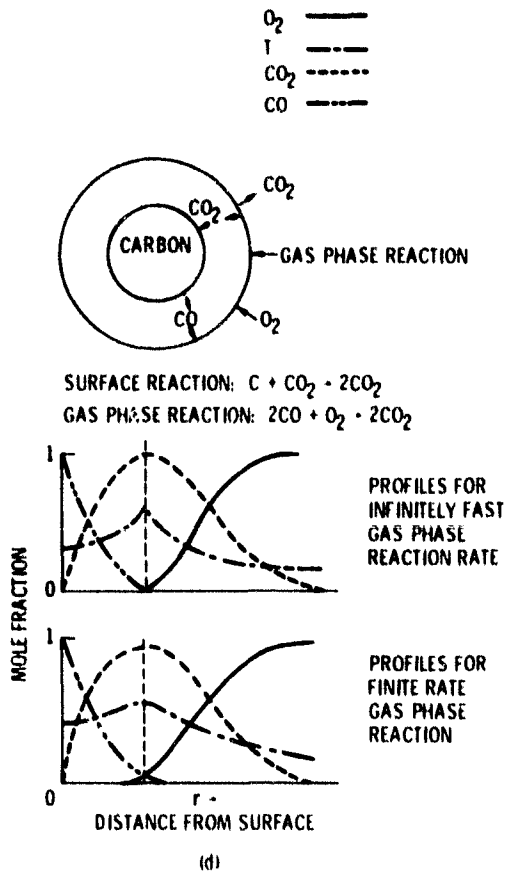

(d)

Figure 4. - Concluded.

cylindrical carbon rod burning according to this model. The gas phase burning was assumed to be a first order reaction with respect to carbon monoxide. The two simplifying assumptions that made the solution approximate were that the carbon monoxide concentration in the boundary layer was small and that the boundary layer was thin so that an average boundary layer thickness could be used. The theoretial carbon monoxide concentration profiles showed good agreement with the experimental data obtained by Wicke and Wurzbacher [5], who burned vertical carbon rods in oxygen. Caram and Amundson [6] obtained numerical solutions for carbon slabs and spheres burning according to this model. They assumed that the gas phase reaction was first order with respect to carbon monoxide, one-half order with respect to oxygen and one-half order with respect to water vapor. The ambient concentration of water vapor, which was considered small enough so that other possible reactions could be neglected, was considered a parameter of the model. They also determined feasible surface temperatures. The feasible surface temperatures were those that allowed the mass fractions to be equal to or greater than zero and less than or equal to one.

A fourth high temperature model has been proposed. In this model, carbon dioxide is reduced to carbon monoxide at the surface through the reaction $CO_2 + C \rightarrow 2CO$. The carbon monoxide moves outward, meeting oxygen, and is burned to carbon dioxide through the gas phase reaction $2CO + C_2 \rightarrow 2CO_2$. Analytically, the gas phase reaction can be considered to occur either with an infinitely fast reaction rate so that a very thin flame sheet forms, or with a finite rate so that a flame zone appears. This model is presented in Figure 4d. Spalding [7] presents a solution for this model using the assumption

that thermodynamic equilibirum exists at the surface and throughout the gas phase. Fendell [1] also considered this model and presents solutions for two different cases: (1) mass transfer controlled, equilibrium, irreversible surface and gas phase reactions; and (2) a finite rate surface reaction and a mass transfer controlled gas phase reaction. Van der Held [8] presents a solution for this model for a one dimensional carbon surface burning in flowing gas. He considered the case of an equilibrium surface carbon dioxide reduction reaction with a homogeneous carbon monoxide oxidation reaction of either 2/3 order, second order, or third order.

The burning rate equations that are generally used for carbon combustion are derived by first solving the continuity equation for the flux of oxygen at the carbon surface. The partial pressure of oxygen at the surface is eliminated from the oxygen flux equation using an Arrhenius rate equation. This results in a burning rate equation. Burning rate equations that have been obtained for carbon spheres and cylinders are presented in Table 1. The definition of the variables in the equations can be found in the Nomenclature Section.

C. Controlling Mechanism

The general burning equations for carbon, such as those in Table 1, are of the form: Combustion Rate = $1/(R_D + R_C)$ where R_D refers to the mass transfer resistance and R_C refers to the chemical process resistance. Therefore, the combustion process can be considered to consist of two processes, a chemical process and a mass transfer process. The mass transfer process consists of convective mass trans-

Table 1. - Combustion rate equations
spheres

$$\dot{m}_1 = \frac{1}{\frac{1}{k_{diff}} + \frac{1}{k}} = \frac{P_{O_{2b}}}{\frac{r_s R T_m}{12\Phi_1 D} + \frac{1}{ke^{-E/RT_s}}}$$ Reference [9]

$\dot{m}_1$ = specific mass combustion rate
Φ_1 = mechanism factor: 1 if CO_2 formed, 2 if CO formed

$$\dot{m}_1 = \frac{12\Phi_1 P_{O_{2s}} A}{\frac{P_n}{\pi T_m^{n-1}} B_1 \frac{(du_\infty \rho)^c}{dT_m^{c/2}} + \frac{2}{d_s}} + a\sqrt{T_s}\, e^{E/RT_s}}$$ Reference [10]

A = proportionality factor
P_n = partial pressure of inert
n = $9720P/\sqrt{MT}$, micromoles of gas impinging on unit surface
M = molecular weight
B_1 = constant
c = constant
a = constant

$$\dot{m}_o = \frac{48\pi r_s^2 P_{O_{2b}}}{\frac{0.1267 T^{1/2} e^{E/RT_s}}{f} + 205160 \frac{r_s}{T^{1/2}}}$$ Reference [11]

$\dot{m}_o$ = mass combustion rate
f = steric factor

Table 1. - C .nued
spheres

$\dot{m}_1^2 - (k_{diff}P_{O_{2b}} + k_d + k_{diff}k_d/k_A)\dot{m}_1 + (k_{diff}P_{O_{2b}})k_D = 0$

$k_{diff} = (\rho_{O_2}M_C/M_{O_2})(D_{O_2}/d)(T/T_o)^{c-1}(2 + B_2Re^{c_1}Pr^{c_2})$

Reference [12]

k_{diff} = velocity constant for diffusion

$k_A = \bar{k}\exp(-E_A/RT)$ = velocity constant for absorption

$k_D = \bar{k}\exp(-E_D/RT)$ = velocity constsnt for desorption

D_{O_2} = diffusion coefficient of oxygen through nitrogen at standard temperature and pressure.

T_o = 273°K

c = constant with a value between 1.5 and 2

B_2 = constant with a value between 0.18 and 0.7

c_1 = constant usually equal to 1/3

c_2 = constant with a value between 0.5 and 0.8

For large k_D $\quad 1/\dot{m}_1 = 1/k_{diff}P_{O_2} + 1/k_AP_{O_{2b}}$

For large k_A $\quad (\dot{m}_1 - k_d)(\dot{m}_1 - k_{diff}P_{O_{2b}}) = 0$

For large k_{diff} $\quad 1/\dot{m}_1 = 1/k_AP_{O_{2b}} + 1/k_D$

k_D controlling at low temperature, and $k_{diff}P_{O_{2b}}$ and $k_AP_{O_{2b}}$ controlling at high temperature.

Table 1. - Continued
spheres

$$\dot{m}_1 = B \frac{\rho_{O_2}}{\frac{1}{k_1} + \frac{1}{\frac{D}{d} Nu_{diff}}}$$

Reference [13]

B = constant that depends on hydrodynamic and temperature conditions

k_1 = reaction coefficient of gas exchange

$Nu_{diff} = 0.7\sqrt{Re}$

Table 1. - Combustion rate equations
cylinders

$$10^3 \dot{m}_1 = \frac{P_{O_{2b}}}{0.032 B_4 P\sqrt{T_s}\left[\frac{117}{dT_s^{0.185}}(d\rho u_\infty)^{0.37} + \frac{2}{d}\right] + 1.05^{-10}\sqrt{T_s}\, e^{-\frac{44000}{RT_s}}}$$

$$B_4 = \frac{D_{O_2-N_2} D_{CO_2-N_2}}{P D_{O_2-N_2} - P_{N_2}(D_{O_2-N_2} - D_{CO_2-N_2})}$$ Reference [14]

D = diffusivity at 273°K

Constants obtained from experimental data on burning of 2.5 cm. dia. brush carbon rods

$$J_c = \frac{P_{O_{2b}}}{\frac{r_s RT \ln(\delta/r_s + 1)}{D_{O_2}} + 2.5\times10^{-3}\sqrt{M_{O_2} RT}\, e^{E/RT}}$$

J_c = molar specific combustion rate

δ = film thickness Reference [15]

For diffusion controlled reaction

$$J_c = \frac{P_{O_{2b}} D_{O_2}}{r_s RT \ln(\delta/r_s + 1)}$$

For film thickness << radius

$$J_c = \frac{P_{O_{2b}} D_{O_2} T^{0.5}}{T_o^{1.5} \delta R}$$

fer and molecular diffusion, and the chemical process consists of chemisorption, the surface reaction, and desorption. The overall combustion rate of a solid particle will thus be determined by the slower of the two processes, that is, either the chemical process or the mass transfer process will control the burning rate.

Various parameters affect both the chemical process rate and the mass transfer rate. The chemical process rate is a function of the material, the surface temperature, and, if the reaction is not zero order, the oxygen partial pressure. The mass transfer rate is a function of ambient gas velocity and temperature, diameter and temperature of the particle, and oxygen partial pressure. As the particle diameter decreases, the mass transfer resistance decreases and a critical diameter is reached where the chemical process controls the combustion rate. Similarly, for a given diameter particle, as the gas velocity increases the mass transfer resistance decreases, and at some critical velocity the chemical process will control the combustion rate. Mulcahy and Smith [16] state that for a fixed size particle, increasing the temperature increases the chemical reaction rate and therefore the chemical process rate, and at some critical temperature the mass transfer will control the rate of combustion. Ubhayakar and Williams [2, 3] conducted extinction experiments and stated that extinction was caused by a change from mass transfer control to chemical process control. They found that as the partial pressure of oxygen was increased, the particles burned to smaller diameters. Therefore, it can be concluded that as the partial pressure of oxygen increases, the critical diameter at which the chemical process controls the combustion rate decreases.

The temperature and particle size, at which a change from chemical process control to mass transfer control has been found to occur, are presented in Table 2. From this table, it can be concluded in agreement with Nettleton [17] and Mulcahy and Smith [16] that the exact conditions, such as temperature, particle size, oxygen partial pressure, and ambient gas velocity, under which the chemical process or the mass transfer process control the carbon combustion rate, are unknown.

D. Experimental Work

1. Functional Dependencies - Experimental investigations to determine the effects of the surface temperature, oxygen partial pressure, and gas velocity and temperature on the combustion rate of carbon have been conducted. Parker and Hottel [14] ran experiments with 2.5 cm diameter rods and found that the specific combustion rate was proportional to the 0.37 power of the mass velocity of the gas. Kuchta, Kent, and Damon [15], using carbon cylinders in air with a velocity range of 8.6 to 165 m/sec and an air temperature range of 900° to 1200° C, found that the absolute reaction rate was proportional to the 0.47 power of the gas velocity. Froberg [19], using 1.27 cm diameter spheres in air and oxygen flows of 0.1 to 1.0 cm/sec and above 760° C, found that the reaction rate was directly proportional to the 0.5 power of the gas velocity. Tu, Davis, and Hottel [10], using 2.5 cm diameter spheres in the temperature range of 680° C to 1430° C and a flow rate of 3.51 to 54.3 cm/sec, found the combustion rate varied as the 0.4 to 0.5 power of the mass velocity. Matsui,

Table 2. - Controlling mechanism

Temperature °C	Control	$\%O_2$	Flow Rate cm/sec	Geometry	Ref.
<727	chemical	21	3.0 - 150	2.5 cm diam. cylinder	[14]
>800	mass transfer	21	853 - 16459	0.307 cm diam. cylinder	[15]
>1000	mass transfer	21	60	1.5 cm diam. sphere	[13]
<727	chemical			particle	[12]
>727	chemical& mass transfer			particle	[12]
927 - 2027	mass transfer			>100μm particle	[16]
>1000	mass transfer			particle	[11]
	chemical			<100μm	[12]
	chemical			<10μm	[18]
	mass transfer			> 1mm	[18]

Koyama, and Uehara [20] impinged a jet of oxygen on a flat carbon disk and found that the combustion rate was proportional to the 0.5 power of the velocity gradient for surface temperatures above 1227° C. All investigators agree that the combustion rate increases with increasing gas velocity when the process is controlled by mass transfer of oxidant to the surface. The combustion rate was found to increase proportionally to the mass velocity of the gas raised to the 0.37 to 0.7 power.

Investigators agree that when the combustion process is controlled by the chemical process, the combustion rate is strongly dependent on the surface temperature, and increases with increasing surface temperature. However, when mass transfer controls the reaction process, the combustion rate was found to be less dependent on temperature. Kuchta, Kant, and Damon [15] found that for a flow rate of approximately 97.5 m/sec, the combustion rate increased proportionally to the 0.20 to 0.25 power of the air temperature, which they state is of the order of magnitude set by theory. They also state that the effect of surface temperature is greater than that of the air temperature, but they were unable to quantitatively determine its effect. Tu, Davis, and Hottel [10] found that the combustion rate varied with the arithmetic mean boundary layer temperature raised to the 0.6 to 1.1 power, which is within the limits of their theory.

Arthur [21] and Tu, Davis, and Hottel [10] found that the combustion rate was proportional to the partial pressure of oxygen raised to a power slightly less than unity. However, Rheed and Wheeler [22] found that the combustion rate was directly proportional to the partial pressure of oxygen.

Mulcahy and Smith [16] state that for mass transfer controlled combustion, a correction factor of approximately 5 was needed to bring the theoretical and experimental burning times of particles into agreement. When the chemical process was controlling the combustion, the prediction of the burning time was dependent on how accurate the pre-exponential factor, the activation energy, and the order of reaction were known.

2. Primary Combustion Products - In the combustion of carbon, the primary products of combustion, i.e., the products at the surface of the solid, are of major importance. The primary products can be CO, CO_2, or a combination of CO and CO_2. The products occurring at the surface of the particle can significantly affect the combustion rate, because one molecule of oxygen can remove either one carbon atom as CO_2, or two carbon atoms as CO. Therefore, to accurately model the process and determine the reaction rate in carbon combustion, the primary products of combustion must be known.

A summary of the work performed to determine the primary products of carbon combustion is presented in Table 3, and Table 4 presents the work done to determine the ratio CO/CO_2 or $CO/(CO + CO_2)$ formed during combustion. In all except four of the investigations, the gas analysis was performed on the end products of combustion. Experimenters in some cases have used either a very fast flow rate to quench secondary reactions or a retardant to try to eliminate CO oxidizing to CO_2. Four of the investigators used a probe to sample the gases in the combustion zone. Two of the investigators used uncooled probes and state that there may have been secondary reactions occurring in the probe. The other two investigators, Arthur [31] and Wicke and

Table 3 - Combustion products

Product mole fraction	Temperature °C	$\%O_2$	Pressure atm	Flow rate	Comments	Ref
0.2% CO 0.6% CO 9.1% CO 0.6% CO 54.4% CO	350 400 500 250 500	21 21 21 100 100	0.52 0.51 0.57 0.50 0.35		Samples taken at end of run.	[22]
CO primary product	600 - 800	100	3.57×10^5		Fast flow rate to prevent secondary reactions. Samples taken at end.	[23]
5% CO_2 no CO	<650	100	1.32×10^{-2}		Gas samples taken from inside carbon ball. Uncooled probe may not have quenched reaction.	[24]
40 -62% CO_2 7 -15% CO	700 - 750	100	1.32×10^{-2}			
1% CO_2 no CO	700	100	1.32×10^{-2}		Sample taken 3 cm above sphere with uncooled probe.	[24]
30 -64% CO_2 no CO	~ 1050	100	1.32×10^{-2}			
CO_2 main product CO negligible	678 - 1149	21		0.53 to 150 cm/sec	Samples taken with uncooled probe; May not have quenched reaction.	[14]

Table 3.- Continued

Product mole fraction	Temperature °C	$\%O_2$	Pressure atm	Flow rate	Comments	Ref.
CO_2 main product	~ 927	21		60 cm/sec	15 mm diam. sphere electrod carbon	[13]
CO main product	>1427	21		60 cm/sec		
CO primary product	1604 - 1623	100	1	80 & 330 cm^3/sec	6.0 to 6.8 cm diam. carbon sphere. CO as primary product determined through calculations.	[25]
CO_2 reduction begins	1100	21		60 cm/sec	15 mm diam. sphere electrode carbon	[13]
CO_2 reduction increases sharply	>1100	21		60 cm/sec		
CO_2 reduction	> 700					[26]
CO_2 reduction	>~ 1000					[5]

Table 3. - Concluded

Product mole fraction		Temperature °C	$\%O_2$	Pressure atm	Flow rate cm^3/sec	R*	Comments	ref.
CO_2	CO							
0.587	0.325	1100	100	1	102	0.043		
0.311	0.028	1100	100	1	102	0.43	Dry air < 2.6×10^{-6}	
0.582	0.374	1180	100	1	102	0.043	percent water	
0.368	0.035	1180	100	1	102	0.43	vapor. Sample	[5]
0.573	0.386	1230	100	1	102	0.043	taken with water	
0.572	0.055	1230	100	1	102	0.43	cooled probe.	
0.717	0.185	1180	100	1	102	0.043	0.02 percent	
0.379	0.005	1180	100	1	102	0.43	water vapor in	
0.792	0.097	1180	100	1	102	0.043	oxygen. Samples	[5]
0.307	0.001	1180	100	1	102	0.43	taken with water	
0.860	0.095	1180	100	1	102	0.043	cooled probe.	
0.301	0.002	1180	100	1	102	0.43		

R* = distance from surface where sample was taken, cm.

Table 4. - CO/CO_2 and $CO/(CO + CO_2)$ product ratio

Product ratio	Temperature °C	$\%O_2$	Pressure atm.	Flow rate	Comments	Ref.
CO/CO_2=0.24 $CO/(CO+CO_2)$ drops off	371 to 483 > 544	2.9 to 100 2.9 to 100	1.1 1.1	15.24 cm/sec 15.24 cm/sec	Coke, charcoal bed.	[27]
$CO/CO_2=10^{3.4}\exp(-12400/RT)$ CO/CO_2=1	480 to 700 530	21		2.5 to 7.0 cm^3/sec	Artifical graphite and coal char; 0.5 to 1.0% volume of $POCl_3$ added to retard CO_2 formation.	[21]
$CO/CO_2=A\exp(-6.4/RT)$ A = surface function	525 to 675	100	$1.3x10^{-5}$ to $2.6x10^{-3}$		Carbon (pure Graphite)	[28]
CO/CO_2=0.7	575	100	$5.13x10^{-5}$		0% burn off Carbon bed	[29]
CO/CO_2=1.1	625	100	$5.13x10^{-5}$		0% burn off	
CO/CO_2=1.4	675	100	$5.13x10^{-5}$		0% burn off	
CO/CO_2=4.2	575	100	$5.13x10^{-5}$		25.8% burn off	
CO/CO_2=5.0	625	100	$5.13x10^{-5}$		25.8% burn off	
CO/CO_2=6.5	675	100	$5.13x10^{-5}$		25.8% burn off	
CO/CO_2=1.56	647			4.4 cm^3/sec	Electrode carbon	[30]
CO/CO_2=3.58	827			4.4 cm^3/sec		
CO/CO_2=0.03	775	21			Carbon tube. Samples taken with cooled probe within a fraction of a millimeter of the surface.	[31]
CO/CO_2=0.04	805	21				
CO/CO_2=0.05	815	21				
CO/CO_2=0.32 to 7.3 increases with velocity	1300 to 1600	100		2697 to 14722 cm^3/sec	Particle in vortex chamber.	[32]

Wurzbacher [5], used a water cooled probe in order to quench any such secondary reactions.

The experiments listed in Tables 3 and 4 were conducted under various test conditions, which had an effect on the primary products formed. Arthur [21] found that the gas velocity had no effect on the CO/CO_2 ratios at low temperatures, but at high temperatures the CO/CO_2 ratio increased rapidly with gas velocity. The temperature at which this transition occurred was dependent on the type of carbon. Phillips, Vastola, and Walker [28, 33] found that as the oxygen partial pressure increased, the CO/CO_2 ratio decreased. Lewis, Gilliland, and Paxton [27] agree with this result for partial pressures below 0.2 atm. Arthur [21] found the CO/CO_2 ratio to be independent of initial oxygen partial pressure in the range of 0.05 atm to 0.25 atm. Phillips et al. [33] and Laine, Vastola, and Walker [29] found that the CO/CO_2 ratio increased with burn-off, but the effect was small except in the early stages where it increased substantially. Lewis et al. [27] state that the $CO/(CO + CO_2)$ ratio is relatively independent of the type of carbon while Walker, Rusinko, and Austin [34], Laine et al. [29], and Phillips et al. [33] state the CO/CO_2 ratio does depend on the nature of the carbon. Wicke and Wurzbacher [5] found that moisture in the air promoted the oxidation of CO to CO_2. For moisture contents greater than 1%, CO hardly played a role in the oxidation process.

Even though the experiments listed in Tables 3 and 4 were conducted under various test conditions, it can be concluded that the CO/CO_2 ratio increases with temperature, which is generally accepted as being the case. And it can be seen that above 1100° C, a CO_2

reduction at the surface can occur and play a part in the combustion process. However, the temperature at which the primary products change from CO_2 to CO cannot be determined from these tables.

Fendell [1], from his literature search, concludes that there are three zones of heterogeneous combustion of carbon. A low temperature range (approximately 395° C to 700° C) in which CO_2 is the primary product of combustion; a mid-temperature range (approximately 700° C to 1100° C) in which CO and CO_2 are the products with a CO_2 reduction at the surface occurring at approximately 895° C; and a high temperature range (approximately 1100° C to 2500° C) in which the following two different mechanisms for the combustion process have been proposed: (1) CO is formed at the carbon surface by direct oxidation and by the reduction of ambient CO_2, and no gas phase reaction of CO occurs; and (2) CO_2 is reduced at the surface to form CO, which is burned in a gas phase reaction.

3. Concentration and Temperature Profile Measurements - Wicke and Wurzbacher [5] experimentally obtained concentration profiles using a water cooled probe for vertical carbon tubes burning in dry and moist oxygen flows in the temperature range of 1100° C - 1230° C. Internally heated high purity spectal carbon tubes, 60 mm long, 15 mm outside diameter, and 3.5 mm wall thickness were used. Gas samples were taken on the outside of the tube, 30 mm from either end. It was found that the concentration profiles obtained when dry oxygen (less than 2.6×10^{-6} percent water vapor present) was used were affected by the reduction reaction, $C + CO_2 \rightarrow 2CO$ (Boudouard reaction), at the surface and the gas phase oxidation of CO to CO_2. With a dry oxygen flow and at the lower surface temperatures, the O_2 concentra-

tion was nearly linear and extrapolated to near zero at the surface. As the surface temperature was increased, the O_2 concentration profiles became less steep and slightly curved. The CO profile was found to be independent of temperature and fell with distance due to homogeneous burning of CO. The CO_2 concentration profile passed through a maximum, which moved to greater distances from the carbon surface and became more pronounced as the temperature increased. Also, in dry oxygen, there was a 8 mm thick blue zone around the carbon tube, which was a result of CO being oxidized to CO_2. With a 0.21% moisture content in the oxygen, the blue flame zone was reduced to a thickness of 1 or 2 mm. With a 1% moisture content in the oxygen, CO hardly played a role in the combustion process.

Kisch [35], using spectrum line reversal and Pt Rh - 10% Pt thermocouples, was able to obtain temperature profiles for burning graphite. Graphite blocks, 20 x 20 x 50 mm, were internally heated and burned in dry oxygen flowing at 30 cm/sec. Both the line reversal and thermocouple measurements showed that there was a maximum temperature between 1 and 2 mm in front of the burning graphite surface. For a 1127° C graphite surface temperature, the maximum gas phase temperature was 1627° C.

Temperature profiles in front of small carbon rods, positioned vertically in a horizontal 6 cm diameter electric pipe furnace, were obtained by deGraaf [36] using the method of spectrum line reversal. The burning rates of the rods were changed by inclining the pipe furnace slightly. At a furnace temperature of 700° C, the carbon flared up and a blue flame zone formed around it. At 800° C, the blue flame zone was approximately 2.5 mm thick. A spectrum of the blue reaction

zone was recorded, and it was identical to the spectrum of a carbon monoxide-air flame. For a furnace temperature of 1000° C, it was found that as the burning rate increased, both the rod surface temperature and the difference between the maximum gas phase temperature and the rod surface temperature increased. The maximum temperature occurred approximately 1.25 mm from the surface. Gas phase temperature profiles were also obtained for different furnace temperatures. The difference between the maximum gas phase temperature and the rod surface temperature was found to decrease as the furnace temperature increased from 950° C to 1100° C. When the furnace temperature was increased from 1100° C to 1180° C, the difference between the maximum gas phase temperature and the carbon surface temperature increased. In this series of tests, the maximum gas phase temperature occurred between 1.0 mm to 1.5 mm from the carbon surface. Also, at the highest furnace temperatures the maximum temperature differences were less pronounced than at the lower furnace temperatures.

In summary, investigators have studied carbon combustion both theoretically and experimentally. The theoretical work has been concerned with the mathematical modeling of the combustion process, while the experimental work has been concerned with determining whether the combustion process is controlled by the mass transfer or by the chemical process. In addition, the effects of particle diameter, surface temperature, oxygen partial pressure, and gas velocity and temperature on the carbon combustion rate have been studied, and experiments have been conducted to determine the species concentration and temperature profiles.

The wide variation in the results of the previously mentioned investigations, along with their generally macroscopic nature, served as the motivating reasons for conducting the present study. It was felt that a series of carefully conducted carbon combustion experiments under both zero and normal gravity conditions would more clearly quantify convective effects, illustrate a possible mechanism dependence on surface position, and provide data more in line with the assumptions made in the mathematical models.

III. ZERO GRAVITY EXPERIMENTATION

A. Test Facility

The experimental data for this part of the study were obtained in the Zero-Gravity Facility at the Lewis Research Center. A schematic diagram of this facility is shown in Figure 5. The facility consists of a concrete-lined 8.5 meter (28 ft) diameter shaft that extends 155 meters (510 ft) below ground level. A steel vacuum chamber, 6.1 meters (20 ft) in diameter and 143 meters (470 ft) high, is contained within the concrete shaft. The pressure in this vacuum chamber is reduced to 13.3 newtons per square meter (1.3×10^{-4} atm) by utilizing the center's wind tunnel exhaust system and an exhauster system located in the facility.

The ground-level service building has, as its major elements, a shop area, a control room, and a clean room. Assembly, servicing, and balancing of the experiment vehicle are accomplished in the shop area. Tests are conducted from the control room, Figure 6, which contains the exhauster control system, the experiment vehicle predrop checkout and control system, and the data retrieval system.

1. Mode of Operation - In the Zero-Gravity Facility, the experiment vehicle is allowed to fall freely from the top of the vacuum chamber, resulting in nominally 5 seconds of free-fall time. By

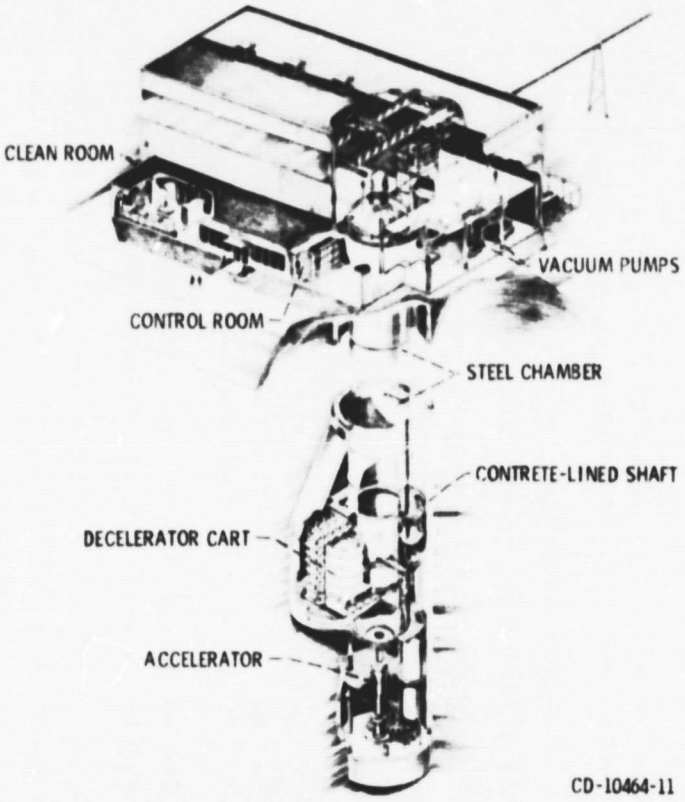

Figure 5. - Schematic diagram of zero-gravity facility.

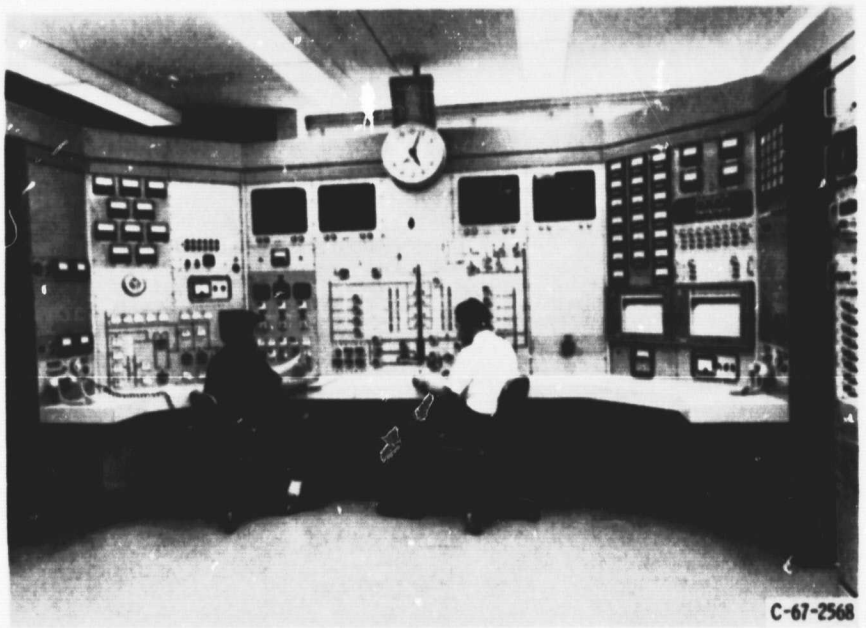

Figure 6. - Control room of zero-gravity facility.

free-fall is meant that there are no guide wires, electrical lines, etc., connected to the vehicle. Therefore, the only force (aside from gravity) acting on the freely falling experiment is due to residual air drag. This results in an equivalent gravitational acceleration acting on the experiment which is estimated to be on the order of 10^{-5} g maximum.

2. Recovery System - After the experiment vehicle has traversed the total length of the vacuum chamber, it is decelerated in a 3.6 meter (12 ft) diameter, 6.1 meter (20 ft) deep container which is located on the vertical axis of the chamber and filled with small pellets of expanded polystyrene. The deceleration rate (averaging 32 g's) is controlled by the flow of pellets through the area between the experiment vehicle and the wall of the deceleration container. The deceleration container is shown in the photograph of Figure 7.

B. Experimental Vehicle

The experiment vehicle used to obtain the data for this study is shown in Figure 8. The overall height (exclusive of the support shaft) was 3.0 meters (9.85 ft), and the largest diameter was 1.06 meters (3.5 ft). The vehicle consisted of a telemetry section contained in the aft fairing and an experimental section housed in the cylindrical midsection.

1. Telemetry System - The on-board telemetry system which was used to record pressure data was a standard Inter-Range Instrumentation Group (IRIG) FM/FM 2200-megahertz telemeter. It was used during a test drop to record up to 18 channels of continuous data. The sys-

Figure 7. - Deceleration system.

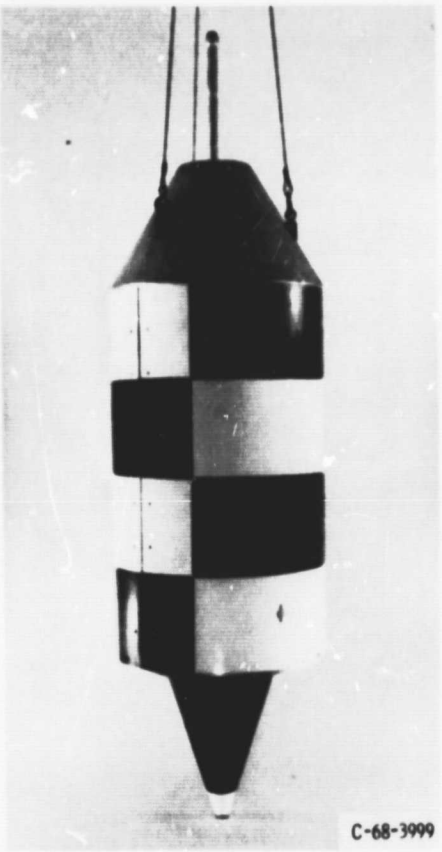

Figure 8. - Experiment vehicle.

tem had a frequency range up to 2100 hertz. The telemetered data were recorded on two high-response recording oscillographs located in the control room.

2. Experimental Section - The details of the experimental section are shown in Figure 9. The spherical tanks at the top section were part of a gaseous nitrogen fire extinguishment system which was used as a safety precaution at the completion of each test. The bulk of the experimental equipment was contained in the central portion of the drop module and consisted of a combustion chamber with a carbon rod holder, two high-speed cameras, power supplies, electrical control box, and plumbing used to fill and evacuate the chamber.

A cross-sectional schematic of the combustion chamber is shown in Figure 10. The combustion chamber was a 78.74 cm (31 in.) long by 39.62 cm (15.6 in.) diameter cylinder with a 19.81 cm (7.8 in.) radius spherical cap. The internal volume of the chamber was approximately 1.1×10^5 cm^3 (6,900 in.^{3}). The walls of the chamber were 0.478 cm (0.188 in.) thick stainless steel. There were four ports for electrical and instrumentation wires. Three of the ports were 12.70 cm (5 in.) from the bottom of the chamber and were 90° apart. The fourth port was 66.04 cm (26 in.) from the bottom of the chamber. There were also two viewing ports that were used to photograph the combustion process. One viewing port was 12.70 cm (5 in.) from the bottom of the chamber and the other one was at the top of the spherical cap. The chamber was split 25.40 cm (10 in.) from the bottom so that the top part of the chamber could be removed for replacement of the experiment. The drop module was equipped with rails and rollers so the top portion of the chamber could be easily moved.

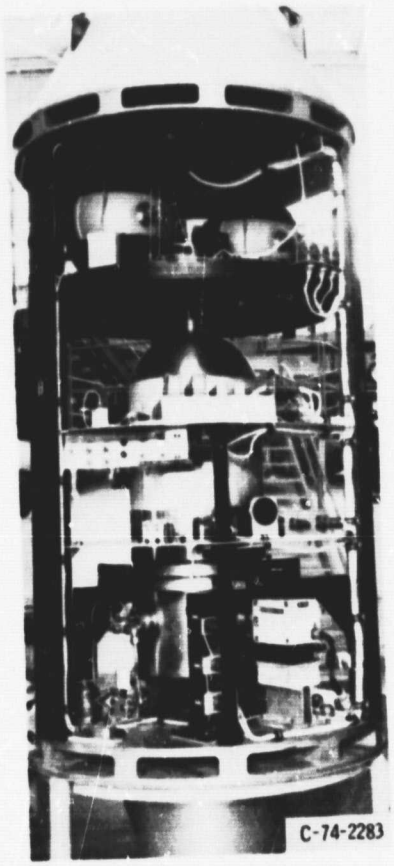

Figure 9. - Test rig.

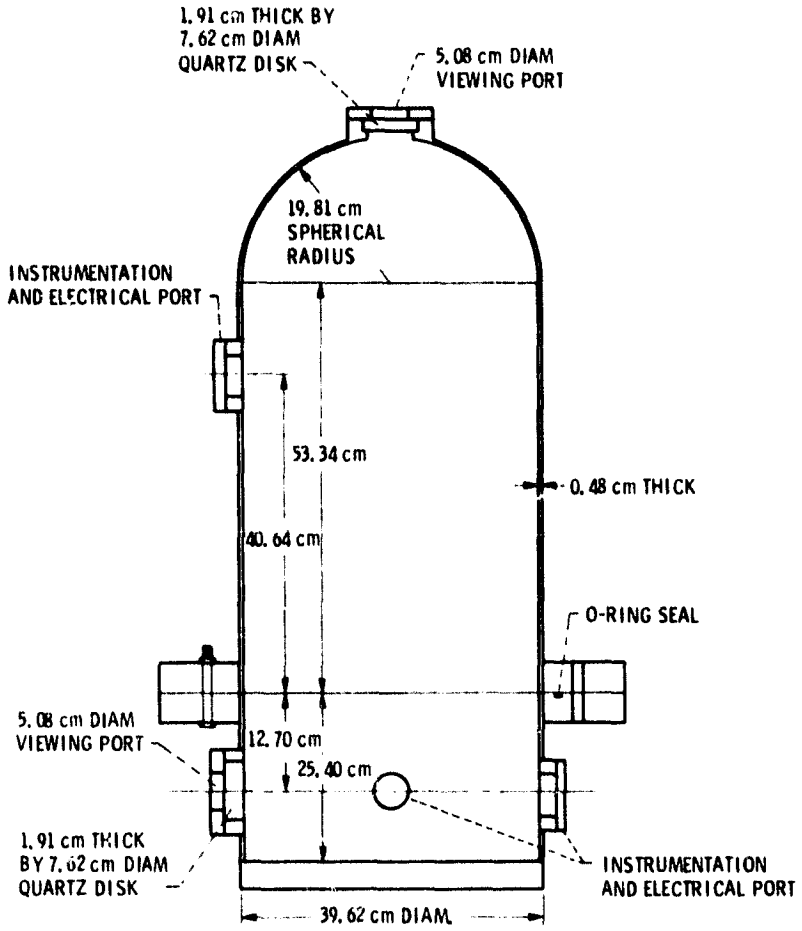

Figure 10. - Cross-sectional schematic of combustion chamber.

The carbon rod burning apparatus was inside the combustion chamber as shown in Figure 11. The carbon rod holder, Figure 12, consisted of a 22.86 cm (9 in.) square by 0.478 cm (0.188 in.) thick stainless steel plate with two 0.478 cm (0.188 in.) diameter bolts 3.81 cm (1.5 in.) long in it. The two bolts were 7.62 cm (3 in.) apart. Lead wires were held to the bolts by tie downs. At the end of the lead wires were junctions that connected to tungsten electrodes. These electrodes were pushed into the ends of the carbon rods. The diameter of the electrodes varied depending upon the diameter of the carbon rod used in the test. When a 0.615 cm (0.242 in.) diameter or 0.457 cm (0.180 in.) diameter carbon rod was used, the electrodes were 0.160 cm (0.063 in.) in diameter. When a 0.305 cm (0.120 in.) diameter carbon rod was used, the electrodes were 0.102 cm (0.040 in.) in diameter.

Two cameras were used to photograph the combustion process. One camera was located at the side viewing port and photographed the end of the carbon rod. This camera ran at 400 frames/sec. The other camera was positioned at the top of the combustion chamber and photographed the length of the rod from the top. This camera ran at 200 frames/sec. A time mark every 0.01 sec was put on the edge of the film. Also, a continuous mark was put on the edge of the film before the package was released. At release, this mark was cut off giving a reference for the start of zero-gravity.

Power to ignite the carbon rod was supplied by rechargeable lead acid battery packs. For the tests using a 0.615 cm (0.242 in.) diameter rod, 48 volts were used and the current draw was approximately 220 amps. For tests using a 0.457 cm (0.180 in.) diameter rod, 32 volts were used with a current draw of approximately 140 amps. Fin-

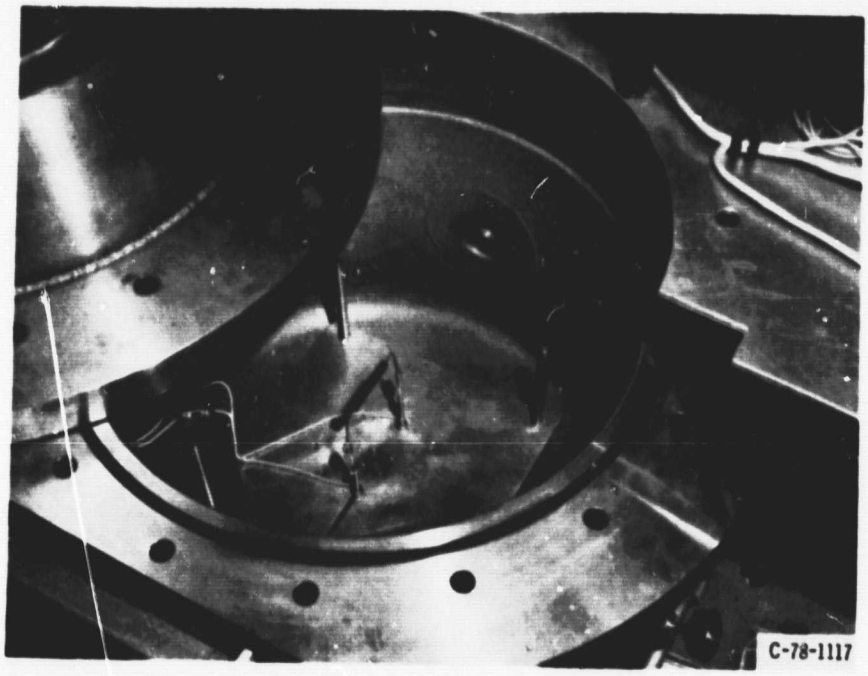

Figure 11. - Carbon rod in burning chamber.

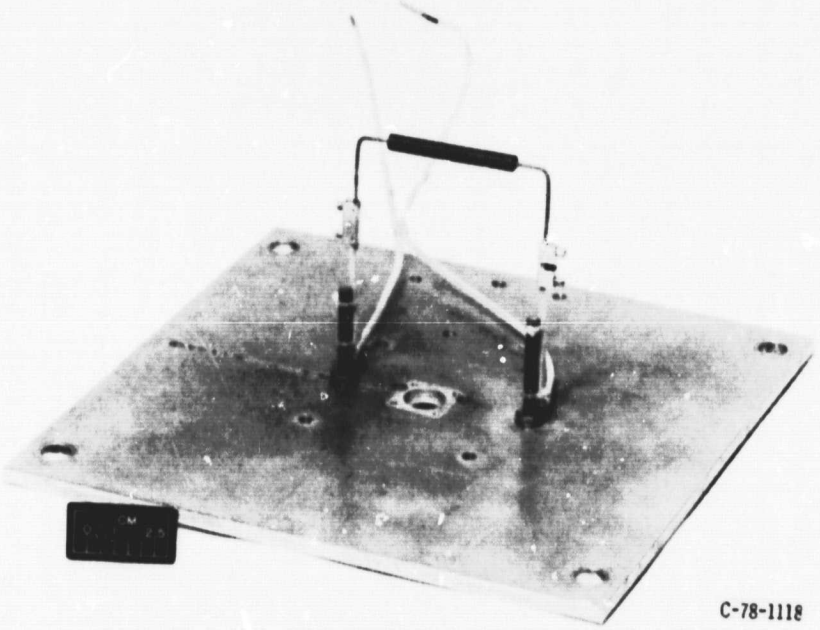

C-78-1118

Figure 12. - Carbon rod holder.

ally, for tests using a 0.305 cm (120 in.) diameter rod, 16 volts were used with a current draw of approximately 50 amps. A separate power supply using rechargeable nickel-cadmium batteries was used to power the other equipment in the drop vehicle.

C. Test Materials

The carbon rods used in the tests were Ultra-Carbon grade U-5 petroleum coke-based spectrographic carbon rods and were, as stated, 0.615 cm, 0.457 cm, or 0.305 cm in diameter. The rods were cut into 5.08 cm (2.0 in.) lengths. Holes of the diameter of the electrodes to be used for a certain sized rod were drilled 0.396 cm (0.156 in.) into the ends of the rod. The atmosphere for the tests was 99.996% pure oxygen with a maximum water vapor content of 0.5 ppm.

D. Test Procedure

Prior to each run, the combustion chamber was wiped clean. Before the carbon rods were inserted into the holder, the holes in the ends of the rods were filled with silver brazing powder. The powder was used to reduce the contact resistance between the rod and the electrode in order to provide a more uniform heating of the rod. After the rod was on the electrode, it was lined up along the axis of the camera that photographed its end. The combustion chamber was then closed and sealed. The chamber was evacuated and purged with dry nitrogen three times before it was filled with dry oxygen.

The proper voltage for ignition of the size rod used in the test was set, along with the length of time power would be supplied to the electrodes. Power to ignite the carbon rods was set to go on 0.045 sec after the vehicle was released. This prevented free convection currents due to the heated rod from being set up inside the combustion chamber.

The vehicle was positioned at the top of the vacuum chamber as shown in Figure 13. It was suspended by the support shaft on a hinged-plate release mechanism. During the vacuum chamber pump-down and prior to release, monitoring of experiment vehicle systems was accomplished through an umbilical cord attached to the top of the support shaft. Electrical power was supplied from ground equipment, with the system being switched to internal power a few minutes before release. The vehicle was released by pneumatically shearing a bolt that was holding the hinged plate in the closed position. No measurable disturbances were imparted to the experiment vehicle by this release procedure.

The total free fall test time obtained was 5.16 sec. During the test drop, the vehicle's trajectory and deceleration were monitored on closed circuit television. Following the drop, the vacuum chamber was vented to the atmosphere and the experiment was returned to ground level.

E. Data Reduction

The burning rods were photographed on high-speed film which was examined on a motion picture analyzer. Flame diameters were measured

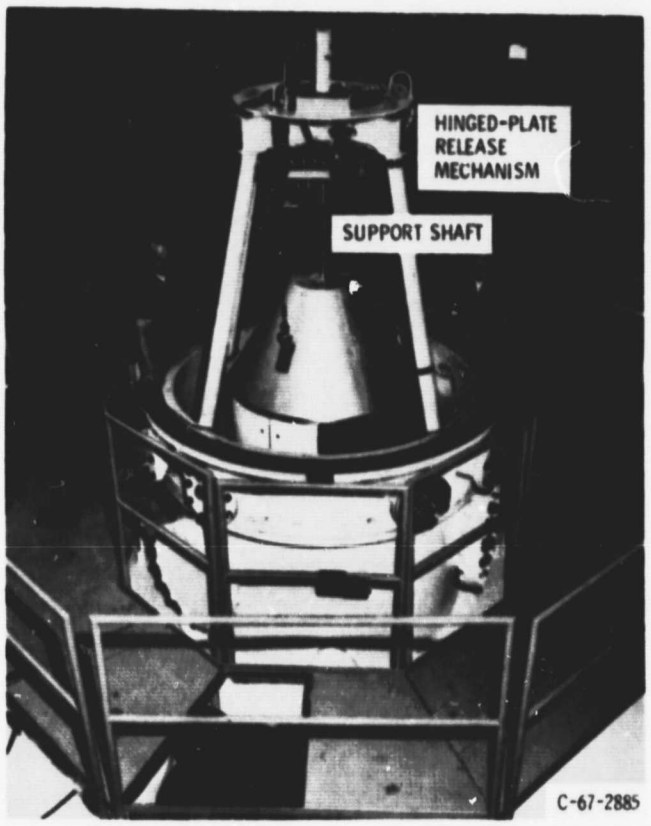

Figure 13. - Typical vehicle positioning prior to release.

as a function of time from the film showing the end view of the rod. No data on the flame could be obtained from the film showing the length of the rod from above because the brightness of the glowing rod obscured the pale blue flame that surrounded the rod. Also, the distance the camera was away from the rod made photographing of the flame difficult even though this camera ran half as fast as the camera photographing the end of the rod.

F. Experimental Results and Discussion

Tests burning 0.615 cm (0.242 in.), 0.457 cm (0.180 in.), and 0.305 cm (0.120 in.) diameter by 5.08 cm (2.0 in.) long carbon rods in 3.45×10^4 N/m^2 (5 psia), 6.89×10^4 N/m^2 (10 psia), 1.03×10^5 N/m^2 (15 psia), and 1.38×10^5 N/m^2 (20 psia) dry oxygen environments were conducted under zero-gravity conditions. The rods were ignited by passing an electric current through them for a set time. The average times for the 0.615 cm, 0.457 cm, and 0.305 cm rods were 1.04 sec, 0.823 sec, and 1.348 sec, respectively. The rods were allowed to burn, supported by their own combustion, for the remainder of the zero-gravity time. In some tests, the power to the carbon rod was not left on long enough to completely ignite the rod. In all except one of the incomplete ignition tests, there was no flame but the rod glowed and decreased in intensity throughout the duration of the test, indicating that the reaction was being quenched. In the other incomplete ignition test which involved a 0.615 cm (0.242 in.) diameter rod in 1.38×10^5 N/m^2 (20 psia) oxygen, the flame flickered and went out as the rod cooled during the test. In all

other tests where sustained burning occurred in zero-gravity, a blue flame surrounded the rod. Photographs of the end of the burning rod for two tests are shown in Figures 14 and 15. In Figure 14, a 0.615 cm (0.242 in.) diameter rod in 1.38×10^5 N/m^2 (20 psia) oxygen is shown, and the same diameter rod in 3.45×10^4 N/m^2 (5 psia) oxygen is shown in Figure 15. From these photographs it can be seen that a symmetrical blue flame extending from the surface surrounded the rod, indicating that the CO formed at the surface was being burned to CO_2 in a gas phase reaction throughout the region. This means the carbon rod was burning according to one of the high temperature models that allows a gas phase reaction. Because the flame extended from the surface of the rod, the carbon was burning according to the models presented by Hugo, Wicke, and Wurzbacher [4] or Caram and Amundson [6]. If the flame did not extend from the surface, that is, if it stood off from the surface, the carbon would be burning according to the models presented by Spalding [7] or van der Held [8]. To obtain the surface temperature, an optical technique would have had to be used, but this was not possible in the zero-gravity facility.

1. Measured Data - The data obtained for the 0.615 cm (0.242 in.), 0.457 cm (0.180 in.), and 0.305 cm (0.120 in.) diameter rods, at four different pressures of 1.38×10^5 N/m^2 (20 psia), 1.03×10^5 N/m^2 (15 psia), 6.89×10^4 N/m^2 (10 psia), and 3.45×10^4 N/m^2 (5 psia) are presented in Figures 16, 17, and 18, respectively. The data presented in the figures were averaged for the tests that were conducted more than once. These figures show the effect of pressure on the ratio of flame diameter to rod diameter. For the three rod diameters, the ratio of flame diameter to rod diameter

Figure 14. - Carbon rod (0.615 cm diam.) burning in 1.38×10^5 N/m^2 (20 psia) oxygen environment.

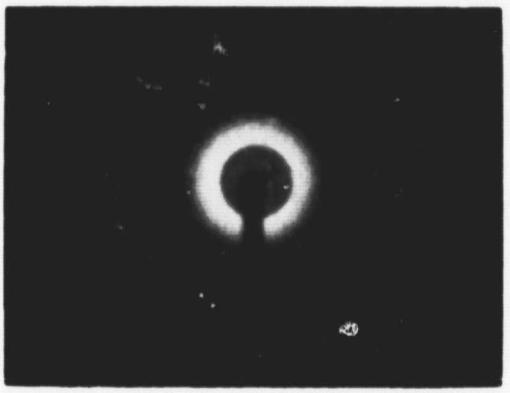

Figure 15. - Carbon rod (0.615 cm diam.) burning in 3.45×10^4 N/m^2 (5 psia) oxygen environment.

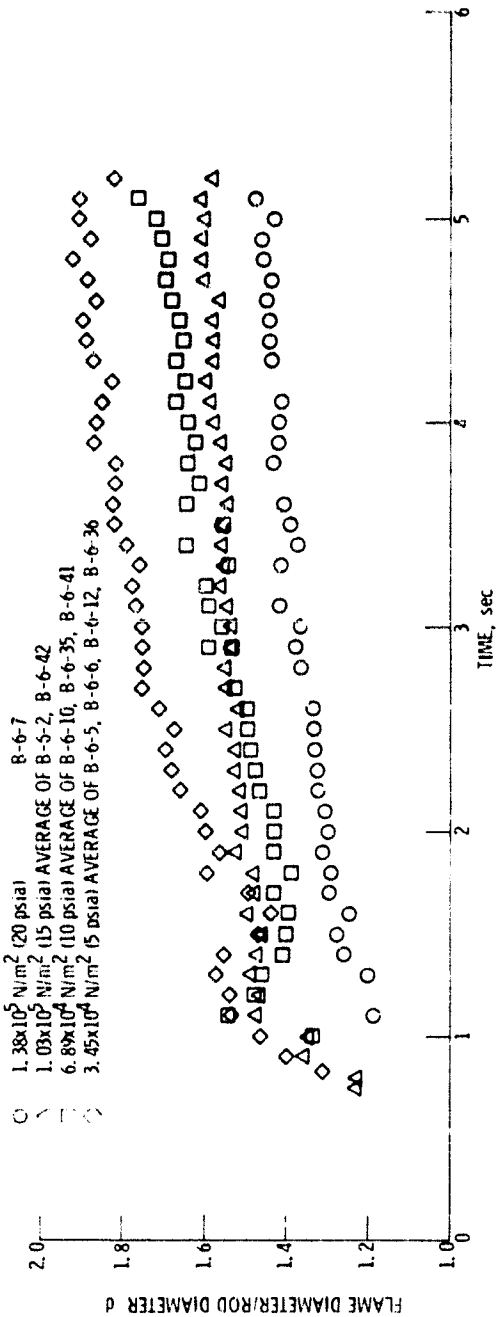

Figure 16. - Effect of pressure on the ratio of flame diameter to rod diameter for 0.615 cm (0.242 in.) diameter rods.

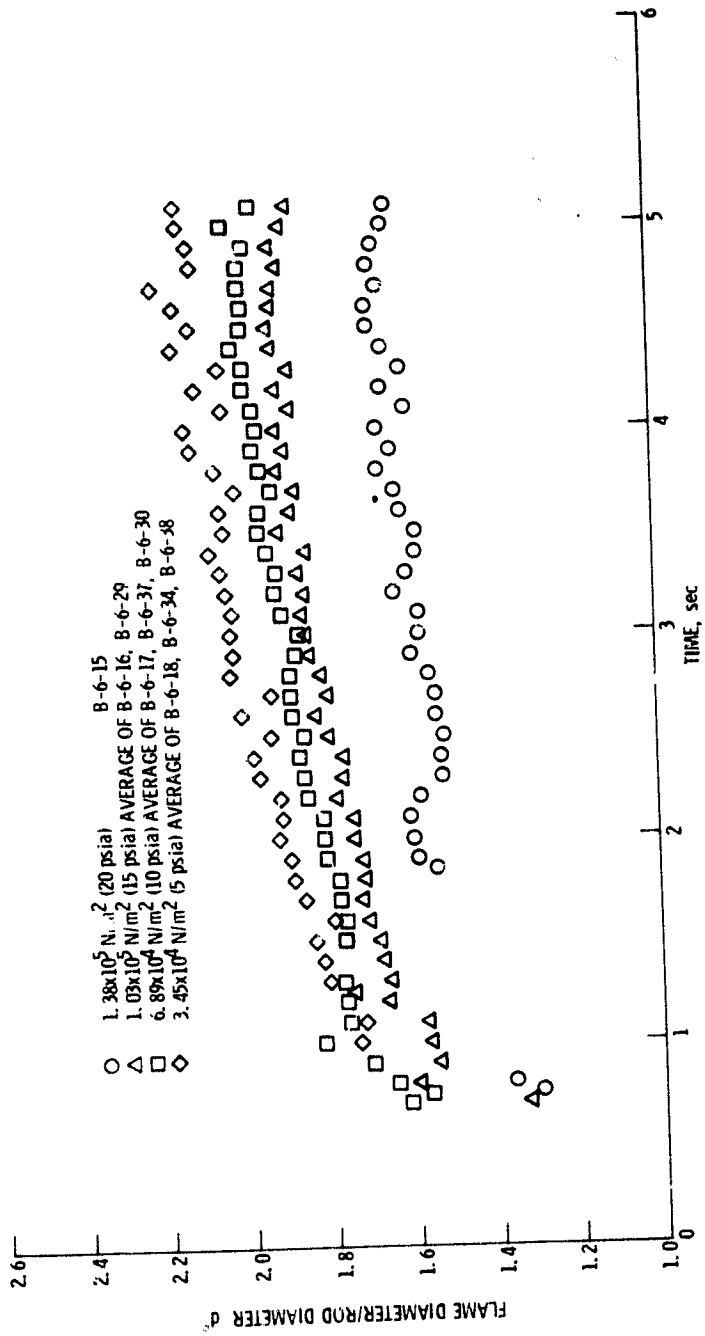

Figure 17. - Effect of pressure on the ratio of flame diameter to rod diameter for 0.457 cm (0.180 in.) diameter rods.

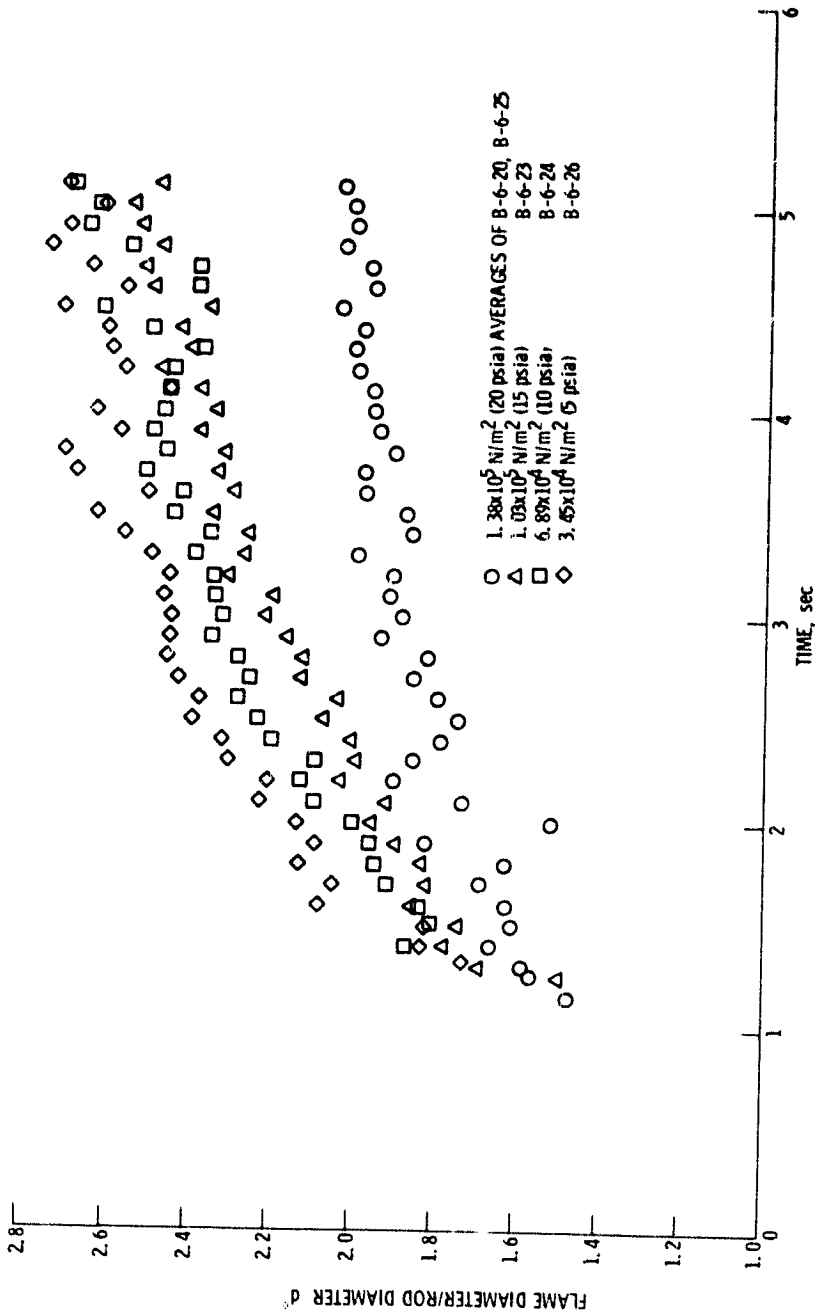

Figure 18. - Effect of pressure on the ratio of flame diameter to rod diameter for 0.305 cm (0.120 in.) diameter rods.

increased as the pressure decreased. Also, the ratio of flame diameter to rod diameter increased less rapidly as the burning time increased. From Figures 16 and 17, it can be seen that for the 0.615 cm (0.242 in.) and 0.457 cm (0.180 in.) diameter rods at times greater than 4 sec, the data generally tends to level off which seems to indicate the ratio may have been approaching a steady value.

The average data for the 1.38×10^5 N/m^2 (20 psia), 1.03×10^5 N/m^2 (15 psia), 6.89×10^4 N/m^2 (10 psia), and 3.45×10^4 N/m^2 (5 psia) runs for the three rods used are presented in Figures 19, 20, 21, and 22. From these figures it can be seen that the ratio of flame diameter to rod diameter decreased as the rod diameter increased. Figures 19 and 20 show that the ratio of flame diameter to rod diameter tends to level off for times greater than 4 sec for the 0.615 cm (0.242 in.) and 0.457 cm (0.180 in.) diameter rods for pressures of 1.38×10^5 N/m^2 (20 psia) and 1.03×10^5 N/m^2 (15 psia).

Figures 16 through 22 show that the ratio of flame diameter to rod diameter increased less rapidly as the burning time increased. As the flame diameter increases, the area for diffusion as well as the volume over which the flame occurs increases, making more oxygen molecules available for the gas phase reaction. This means the flame will grow less rapidly with time because there is more oxygen available for the reaction.

2. Statistical Analysis - The data obtained from each zero-gravity test was curve-fitted numerically using an exponential fit. The equations obtained along with the sum of residuals squared (Σ residuals^2), the total sum of squares (total SSQ), R squared (R^2) val-

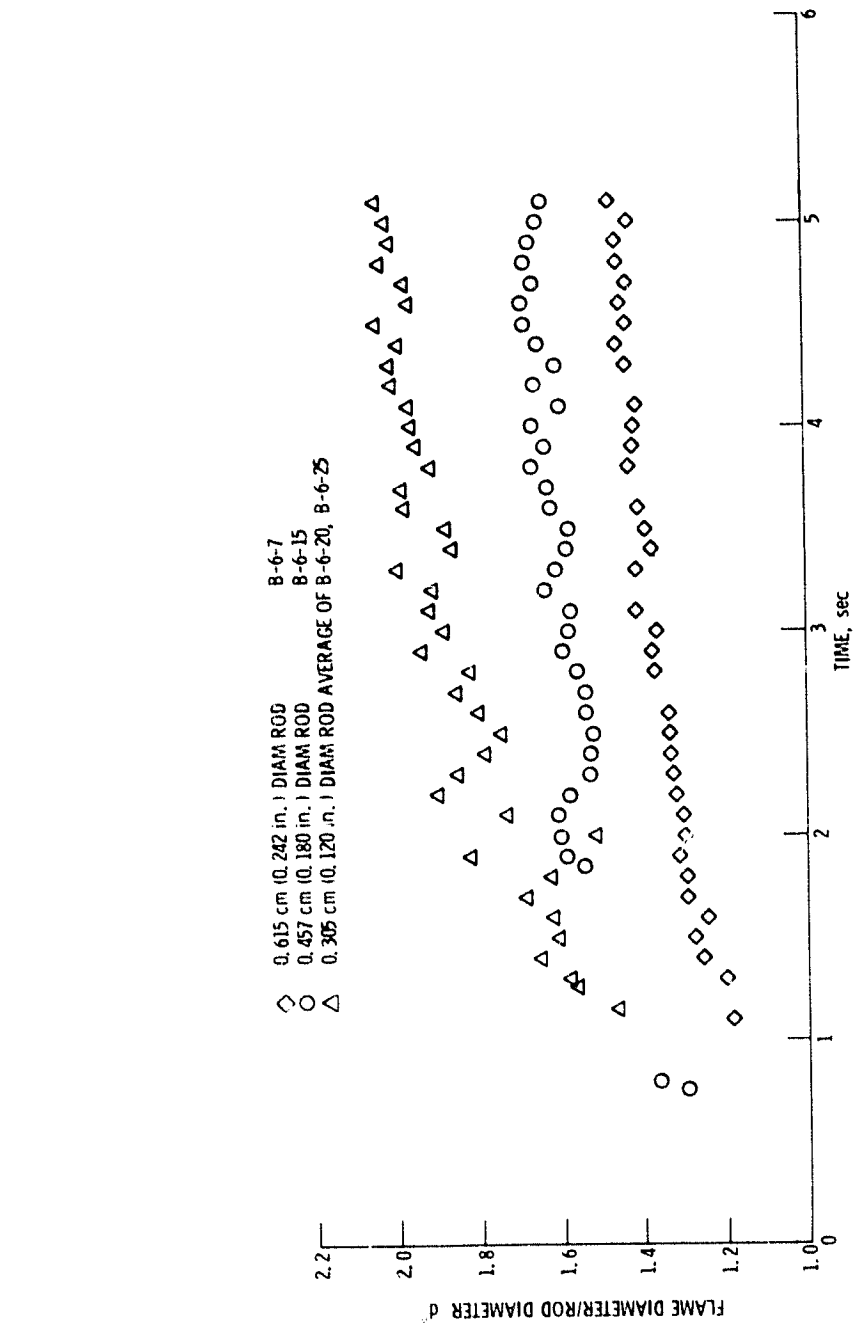

Figure 19. - Effect of rod diameter on the ratio of flame diameter to rod diameter for 1.38x10^5 N/m^2 (20 psia) pressure.

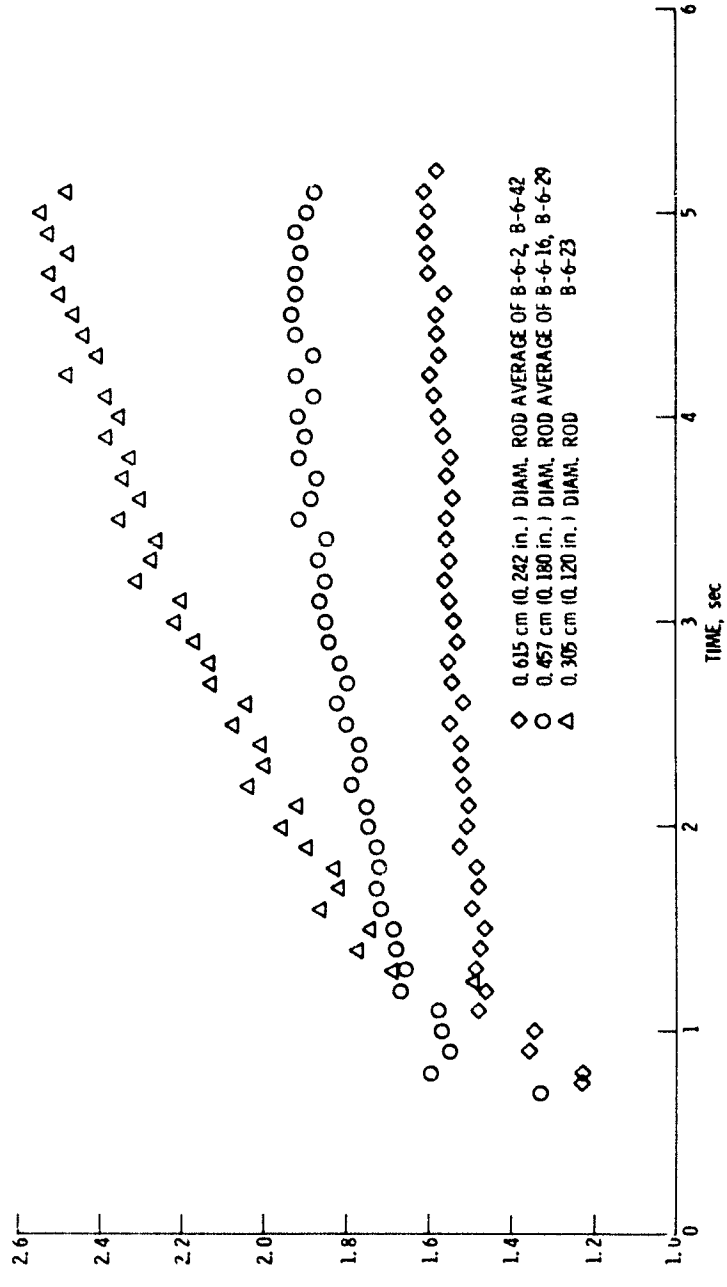

Figure 20. - Effect of rod diameter on the ratio of flame diameter to rod diameter for 1.03×10^5 N/m^2 (15 psia) pressure.

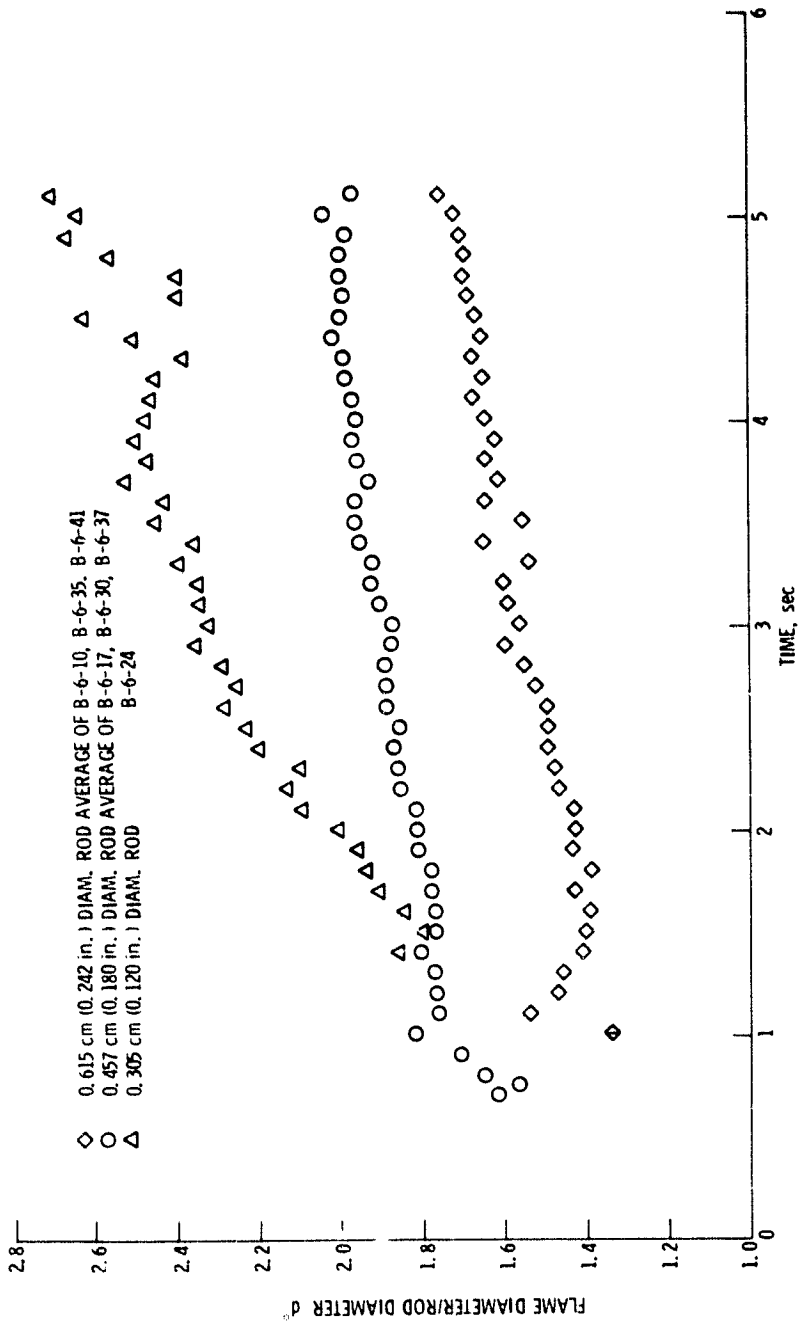

Figure 21. - Effect of rod diameter on the ratio of flame diameter to rod diameter for 6.89x10^4 N/m^2 (10 psia) pressure.

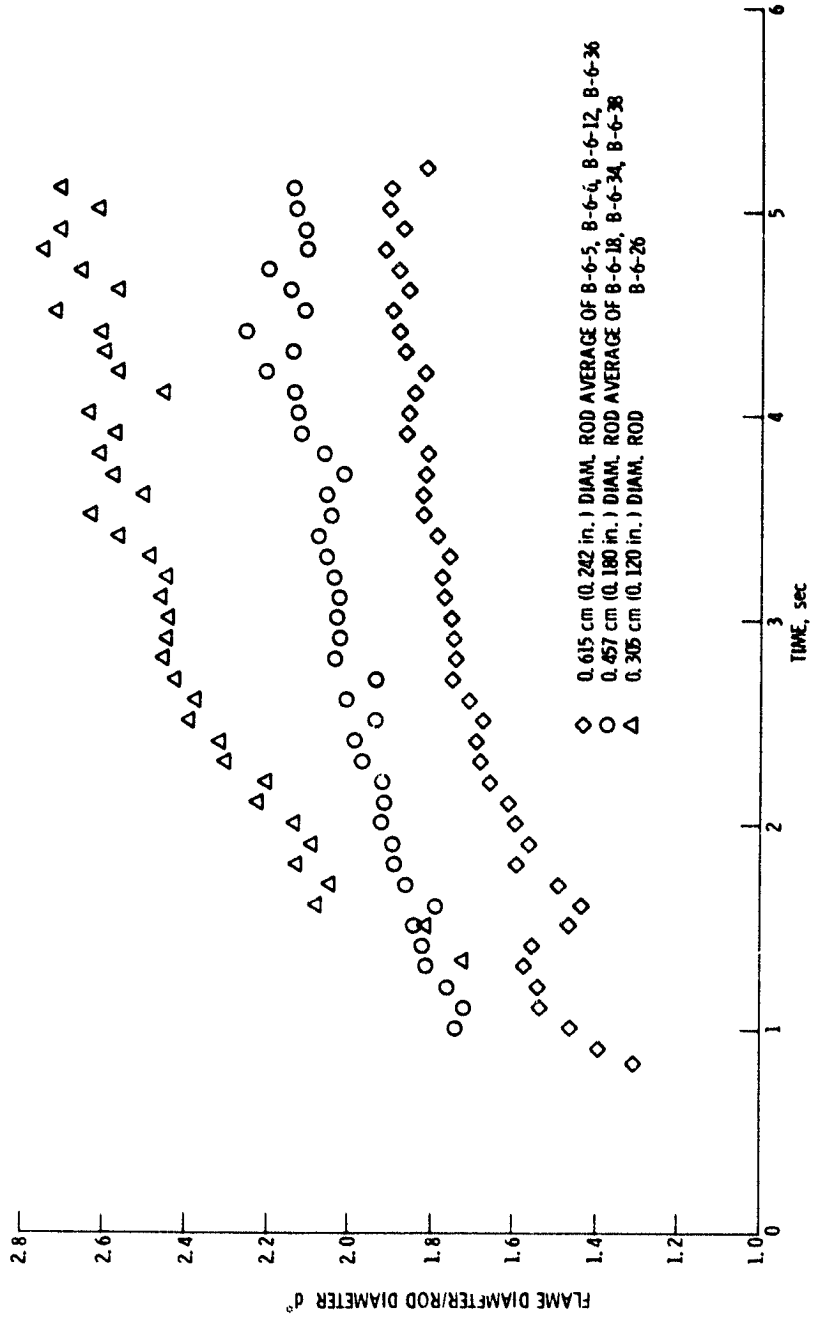

Figure 22. - Effect of rod diameter on the ratio of flame diameter to rod diameter for 3.45×10^4 N/m^2 (5 psia) pressure.

ues, the number of data points (n) used in the curve fit, the variance around the fitted line (MSE) and the standard deviations (S) are presented in Table 5. The sum of residuals squared is $\Sigma(d_i^* - \hat{d}_i^*)^2$, where $\hat{d}^*$ is the value obtained from the curve fit and d^* is the actual ratio of flame diameter to rod diameter. The total sum of squares is $\Sigma(d_i^* - \bar{d}^*)^2$ and is equal to $\Sigma(d_i^* - \hat{d}_i^*)^2 + \Sigma(\hat{d}_i^* - \bar{d}^*)^2$ where $\bar{d}^*$ is the mean value of d^*. The R^2 is equal to (total SSQ $-$ Σ residuals^2)/total SSQ or $\Sigma(\hat{d}^* - \bar{d}^*)^2 / \Sigma(d_i^* - \bar{d}^*)^2$. According to Reference [37], the R^2 value is a measure of the proportion of the total variation about the mean explained by regression. Therefore the R^2 value is a measure of the goodness of fit; if $R^2 = 1$ there is a good fit and if it is zero there is no fit. The R^2 values obtained for the curve fits ranged from 0.974 to 0.577 which means, in general, that the fits are fairly good. The variance around the fitted line is the sum of the residuals squared, divided by the number of points used in the fit. The standard deviation is the square root of the variance around the fitted line.

The experimental data along with the curve fits are presented in Figures 23 to 34. These figures show that the curve fits do fit the data well. Also, Figures 26, 27, 28, 29, 31, 32, and 33 show that, in general, the variation within a test was less than the variation between tests that were conducted with the same diameter rods and at the same pressure. The differences between tests are attributed to the surface temperature of the rod, which could not be controlled or measured. If sufficient time were available so that the rods could have reached an equilibrium burning temperature, they would be expected to

Table 5. - Curve fit equations

Test#	Diameter, d cm	(in.)	Pressure, P N/m^2	(psia)	Curve fit equation $\hat{d}^* = \alpha(1-\exp(-\phi_1 t - \phi_2 t))$	ΣResiduals^2	Total SS	R^2	n	MSE	S
B-6-26	0.305	(0.120)	1.45×10^4	(5)	$\hat{d}^*=2.718(1-\exp(-0.799t-0.003))$	0.1118	2.682	0.958	39	0.0034	0.059
B-6-24	0.305	(0.120)	6.89×10^4	(10)	$\hat{d}^*=2.662(1-\exp(-0.814t-0.210))$	0.1270	1.922	0.934	37	0.0034	0.059
B-6-21	0.305	(0.120)	1.03×10^5	(15)	$\hat{d}^*=2.760(1-\exp(-0.397t-0.396))$	0.0739	1.380	0.974	40	0.0018	0.043
B-6-20	0.305	(0.120)	1.38×10^5	(20)	$\hat{d}^*=1.900(1-\exp(-0.652t-0.644))$	0.1966	0.726	0.729	37	0.0051	0.073
B-6-28	0.305	(0.120)	1.38×10^5	(20)	$\hat{d}^*=2.228(1-\exp(-0.579t-0.588))$	0.0680	1.052	0.935	40	0.0017	0.041
B-6-18	0.475	(0.180)	3.45×10^4	(5)	$\hat{d}^*=2.402(1-\exp(-0.651t-0.610))$	0.0647	1.417	0.954	42	0.0015	0.039
B-6-18	0.475	(0.180)	3.45×10^4	(5)	$\hat{d}^*=1.852(1-\exp(-0.879t-0.819))$	0.0847	0.142	0.567	35	0.0018	0.043
B-6-14	0.475	(0.180)	3.45×10^4	(5)	$\hat{d}^*=2.178(1-\exp(-0.803t-0.879))$	0.1612	0.674	0.761	42	0.0038	0.062
B-6-17	0.475	(0.180)	6.89×10^4	(10)	$\hat{d}^*=2.736(1-\exp(-0.434t-0.936))$	0.0554	0.764	0.927	41	0.0014	0.037
B-6-37	0.475	(0.180)	6.89×10^4	(10)	$\hat{d}^*=1.945(1-\exp(-0.993t-1.278))$	0.0874	0.332	0.736	45	0.0019	0.044
B-6-30	0.475	(0.180)	6.89×10^4	(10)	$\hat{d}^*=1.863(1-\exp(-0.951t-1.219))$	0.1121	0.265	0.577	43	0.0026	0.051
B-6-29	0.475	(0.180)	1.03×10^5	(15)	$\hat{d}^*=2.108(1-\exp(-0.414t-0.911))$	0.0666	1.139	0.942	45	0.0015	0.038
B-6-16	0.475	(0.180)	1.03×10^5	(15)	$\hat{d}^*=1.841(1-\exp(-1.022t-0.864))$	0.0159	0.044	0.637	33	0.00048	0.022
B-6-15	0.475	(0.180)	1.38×10^5	(20)	$\hat{d}^*=1.683(1-\exp(-0.625t-1.132))$	0.0403	0.223	0.818	33	0.00122	0.035
B-6-36	0.615	(0.242)	1.45×10^4	(5)	$\hat{d}^*=2.016(1-\exp(-0.649t-0.683))$	0.0530	1.229	0.957	44	0.0012	0.035
B-6-6	0.615	(0.242)	3.45×10^4	(5)	$\hat{d}^*=1.734(1-\exp(-0.787t-0.903))$	0.1235	0.371	0.667	40	0.0031	0.056
B-6-12	0.615	(0.242)	3.45×10^4	(5)	$\hat{d}^*=2.021(1-\exp(-0.425t-0.434))$	0.0563	0.466	0.879	30	0.0019	0.043
B-6-5	0.615	(0.242)	3.45×10^4	(5)	$\hat{d}^*=2.164(1-\exp(-0.527t-0.403))$	0.0362	0.803	0.880	32	0.0030	0.055
B-6-35	0.615	(0.242)	6.89×10^4	(10)	$\hat{d}^*=2.031(1-\exp(-0.252t-0.747))$	0.0169	0.634	0.973	39	0.00043	0.021
B-6-41	0.615	(0.242)	6.89×10^4	(10)	$\hat{d}^*=1.509(1-\exp(-0.895t-0.905))$	0.0279	0.098	0.716	38	0.00073	0.027
B-6-10	0.615	(0.242)	6.89×10^4	(10)	$\hat{d}^*=1.926(1-\exp(-0.479t-0.472))$	0.0647	0.514	0.874	31	0.0021	0.046
B-6-2	0.615	(0.242)	1.03×10^5	(15)	$\hat{d}^*=1.577(1-\exp(-0.978t-1.201))$	0.0991	0.273	0.637	39	0.0025	0.050
B-6-42	0.615	(0.242)	1.03×10^5	(15)	$\hat{d}^*=1.583(1-\exp(-0.903t-0.992))$	0.0139	0.186	0.925	42	0.00033	0.018
B-6-7	0.615	(0.242)	1.38×10^5	(20)	$\hat{d}^*=1.448(1-\exp(-0.783t-0.816))$	0.0116	0.201	0.943	36	0.00032	0.018

d^* = flame diameter/ rod diameter

t = time, sec.

α, ϕ_1, ϕ_2, are coefficients

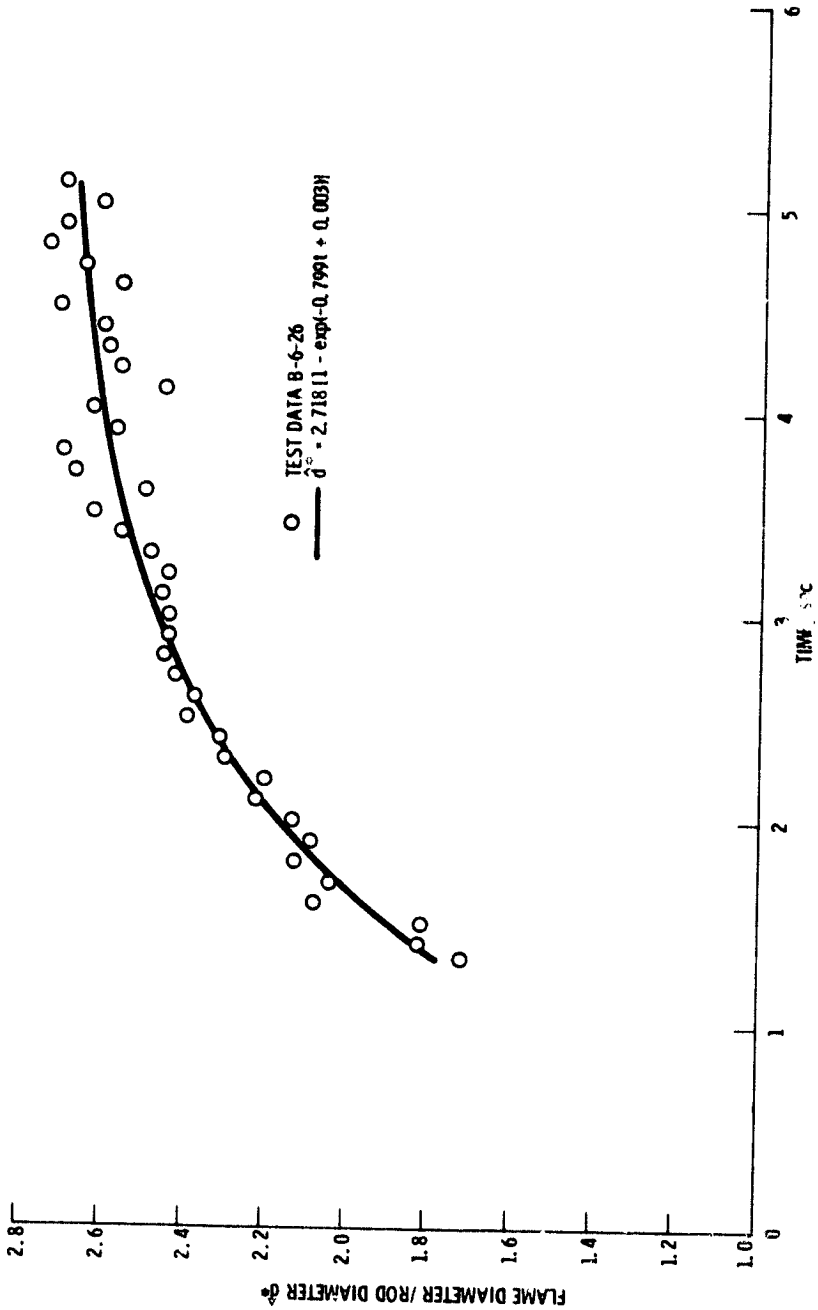

Figure 23. - Comparison of experimental data and curve fit for 0.305 cm (0.120 in.) diameter rod burned in 3.45x10^4 N/m^2 (5 psia) oxygen.

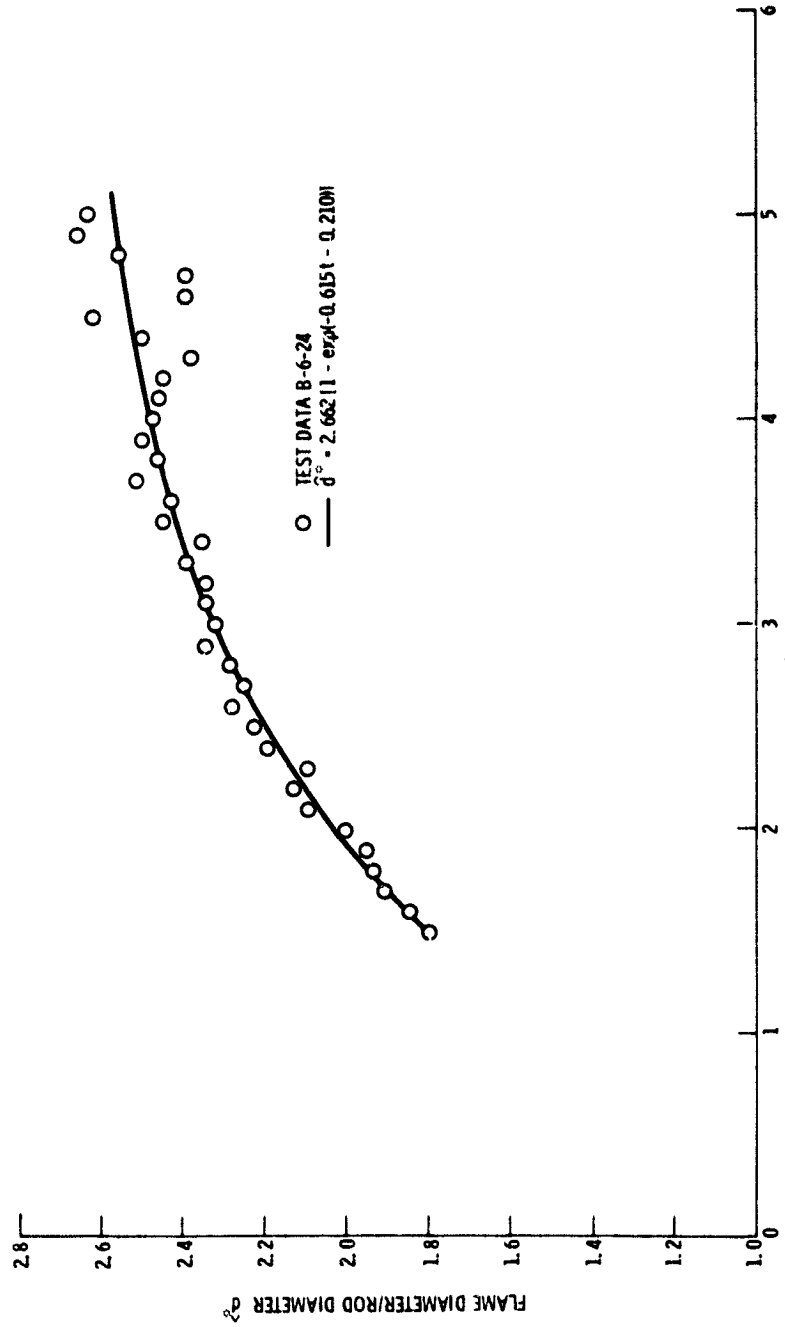

Figure 24. - Comparison of experimental data and curve fit for 0.305 cm (0.120 in.) diameter rod burned in 6.89×10^6 N/m^2 (10 psia) oxygen.

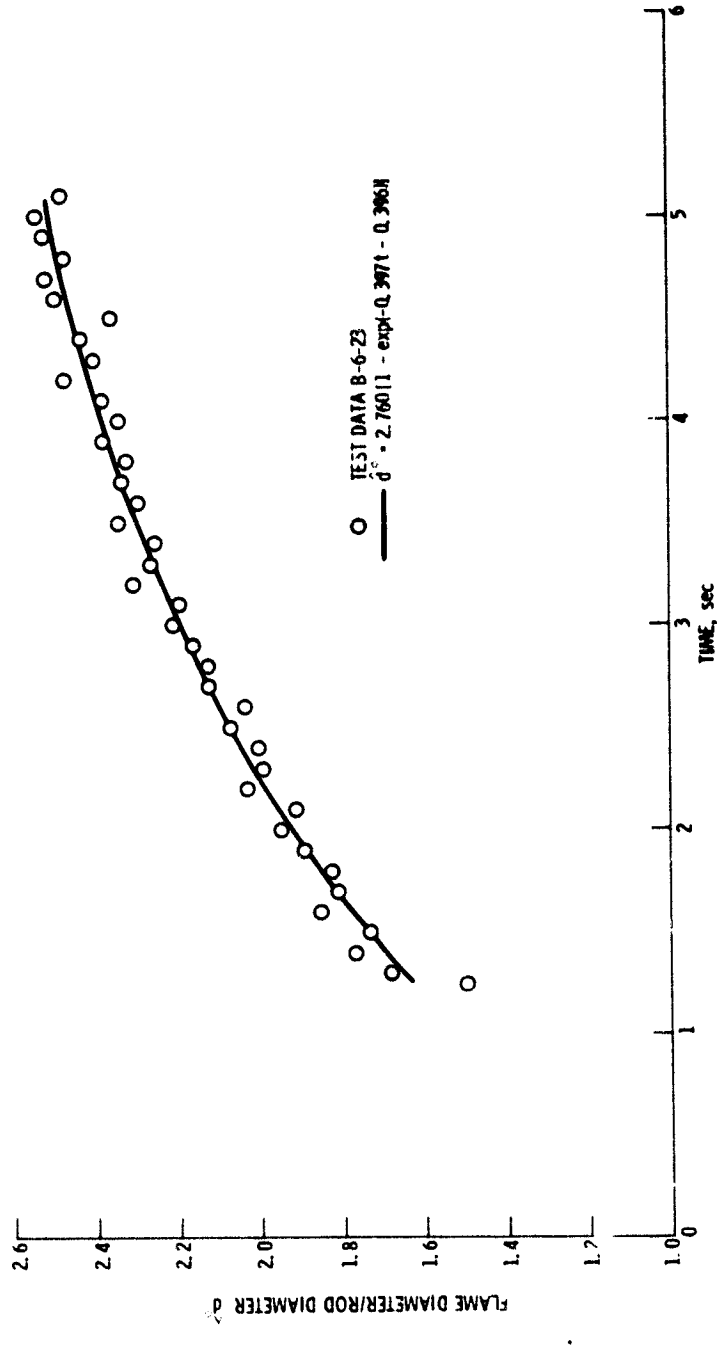

Figure 25. - Comparison of experimental data and curve fit for 0.305 cm (0.120 in.) diameter rod burned in 1.03×10^5 N/m^2 (15 psia) oxygen.

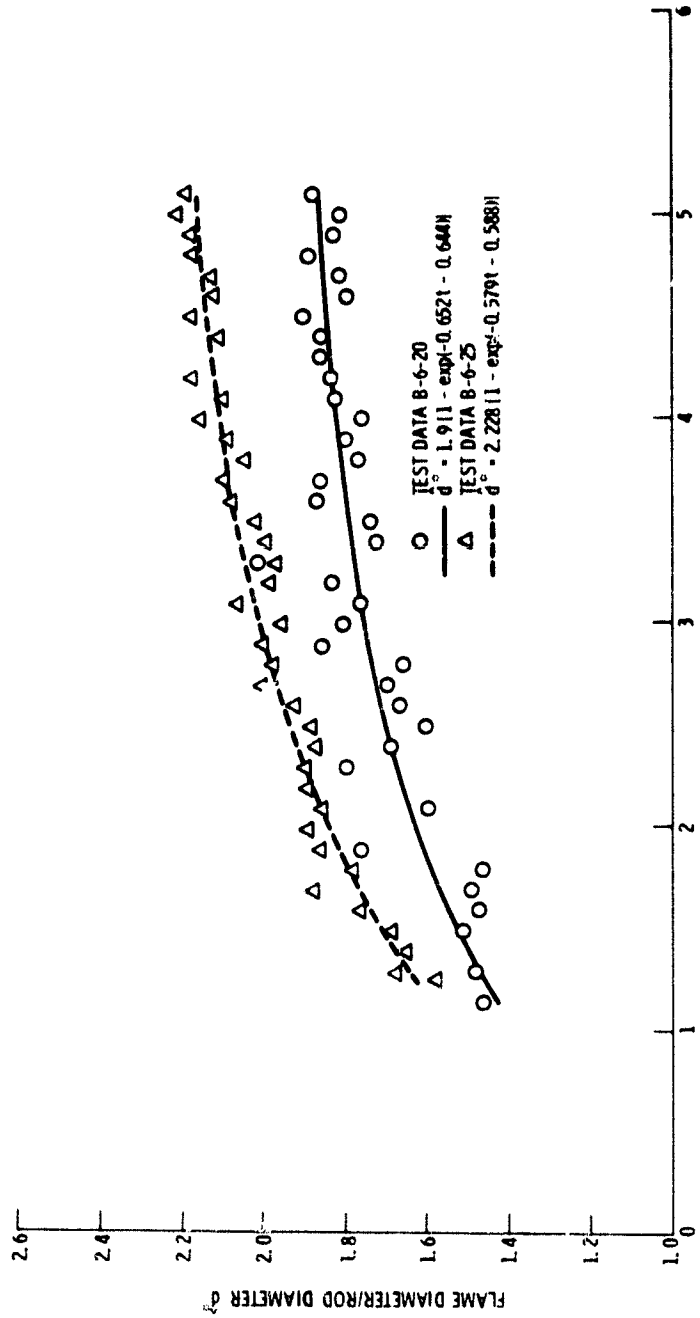

Figure 26. - Comparison of experimental data and curve fit for 0.305 cm (0.120 in.) diameter rod burned in 1.38x10^5 N/m^2 (20 psia) oxygen.

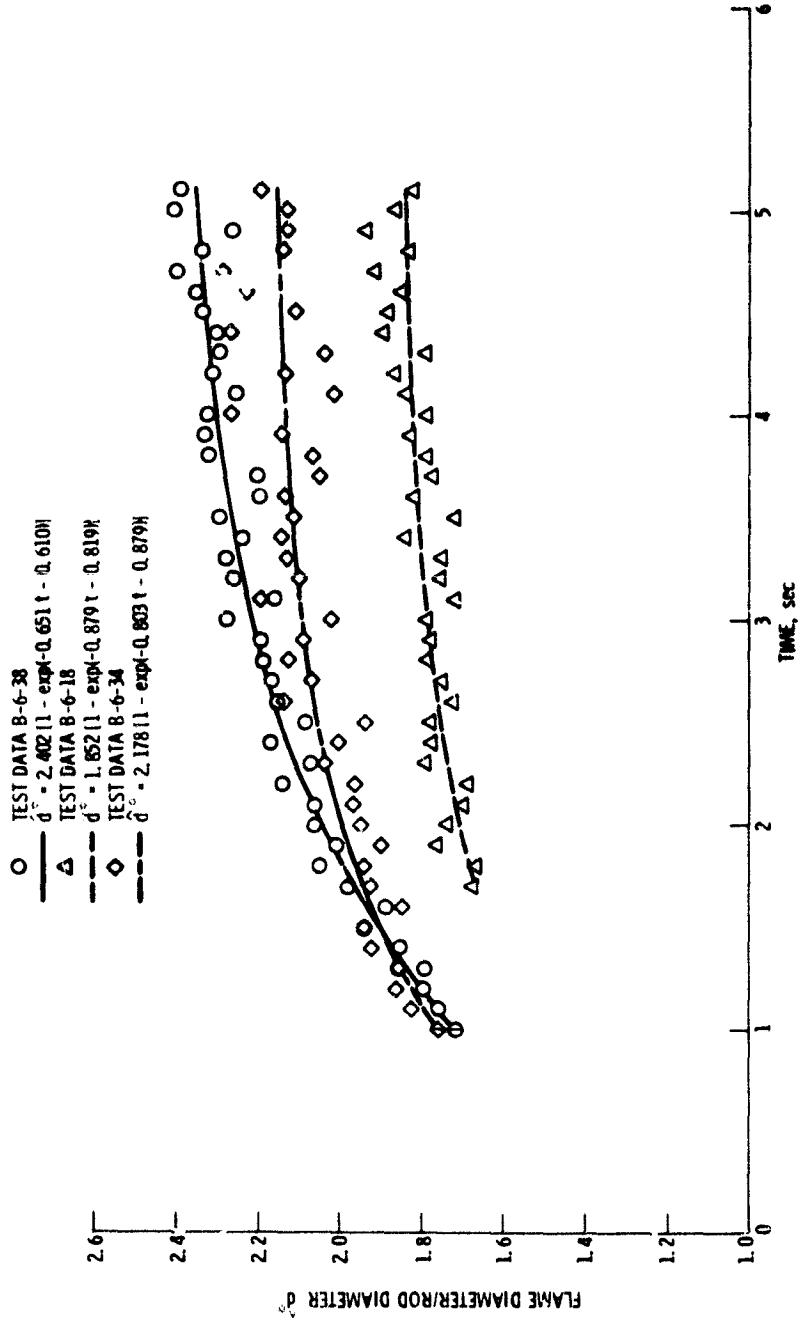

Figure 27. - Comparison of experimental data and curve fit for 0.457 cm (0.180 in.) diameter rod burned in 3.45×10^6 N/m^2 (5 psia) oxygen.

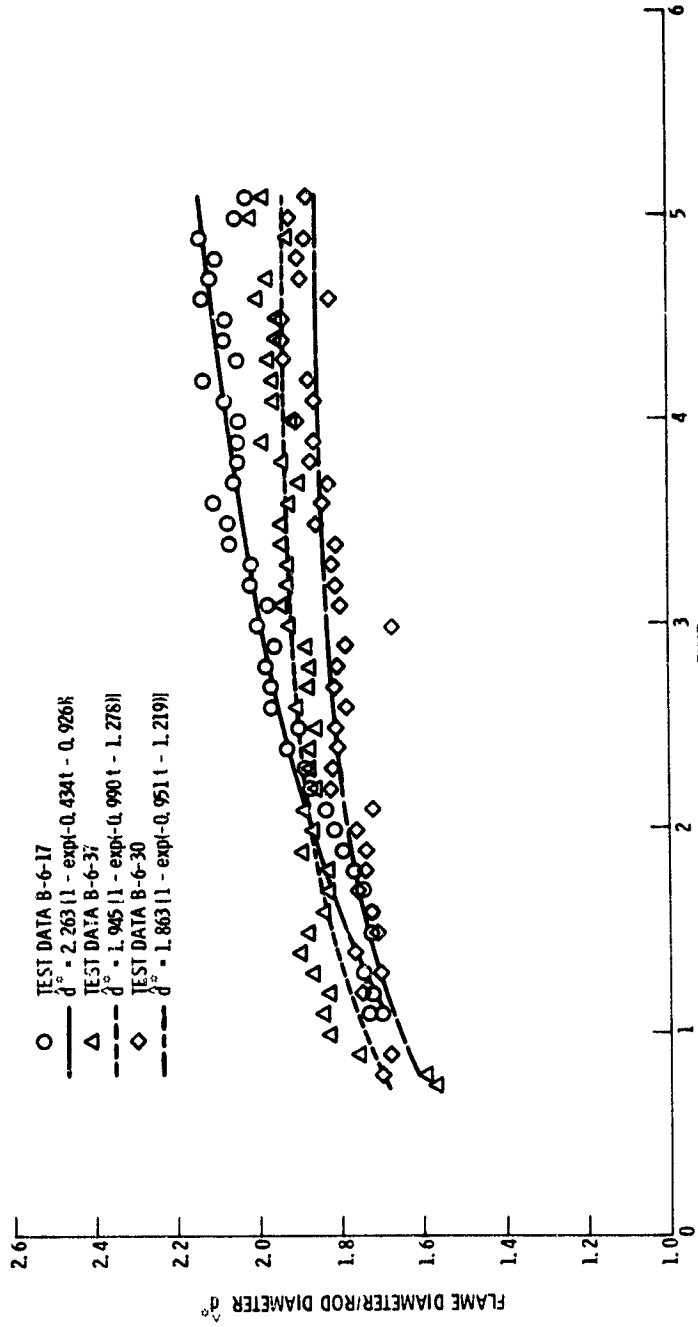

Figure 26. - Comparison of experimental data and curve fit for 0.457 cm (0.180 in.) diameter rod burned in 6.89×10^4 N/m^2 (10 psia) oxygen.

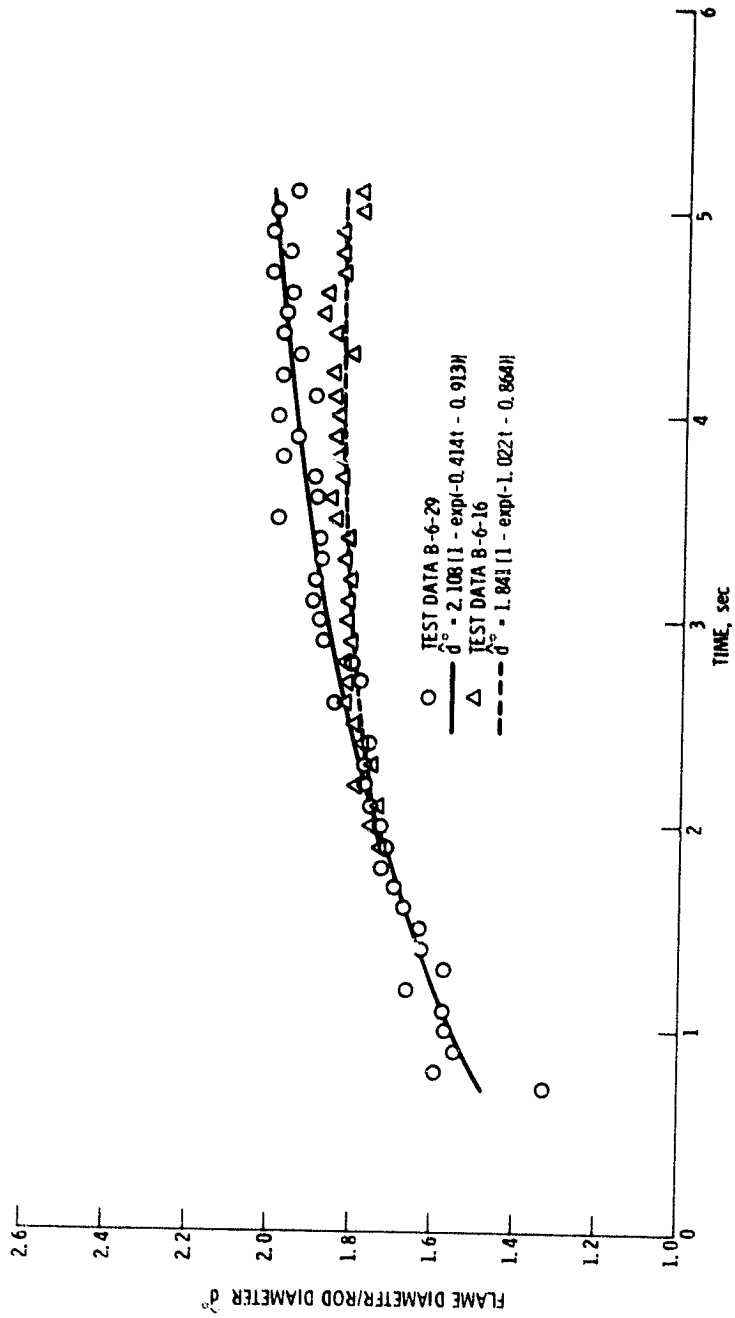

Figure 29. - Comparison of experimental data and curve fit for 0.457 cm (0.180 in.) diameter rod burned in 1.03×10^5 N/m^2 (15 psia) oxygen.

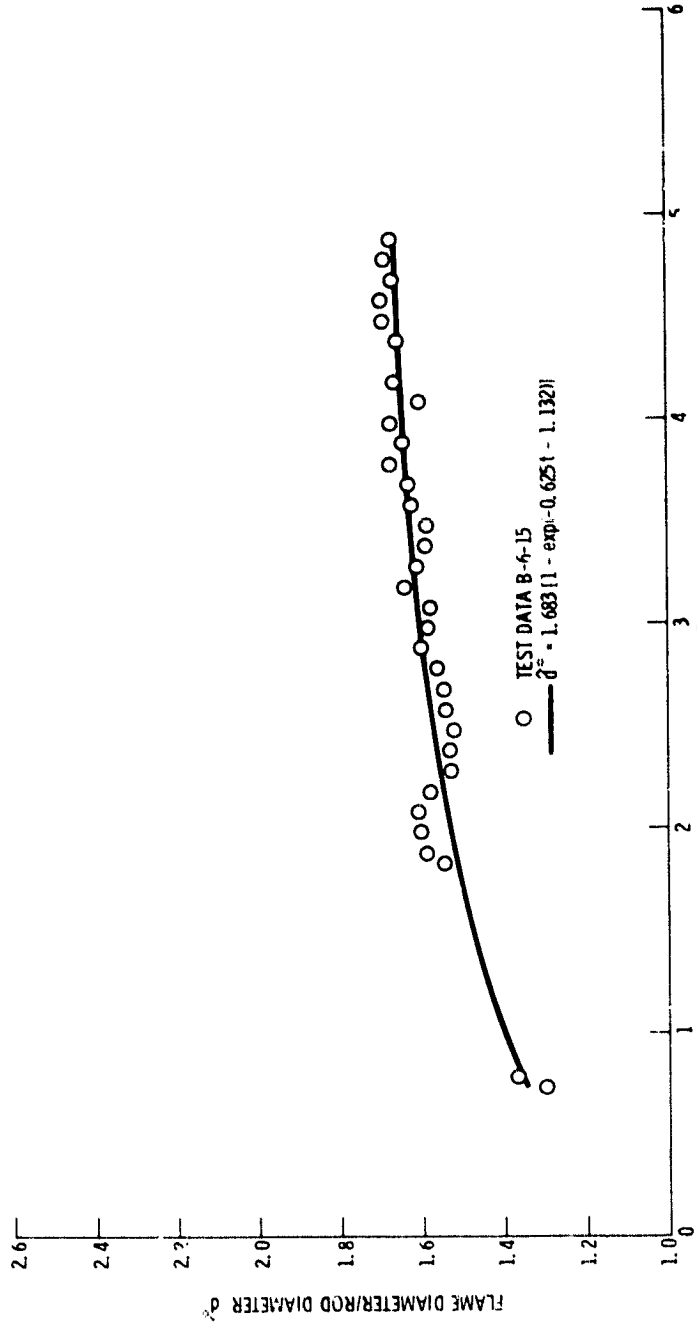

Figure 30. - Comparison of experimental data and curve fit for 0.457 cm (0.180 in.) diameter rod burned in 1.38×10^5 N/m^2 (20 psia) oxygen.

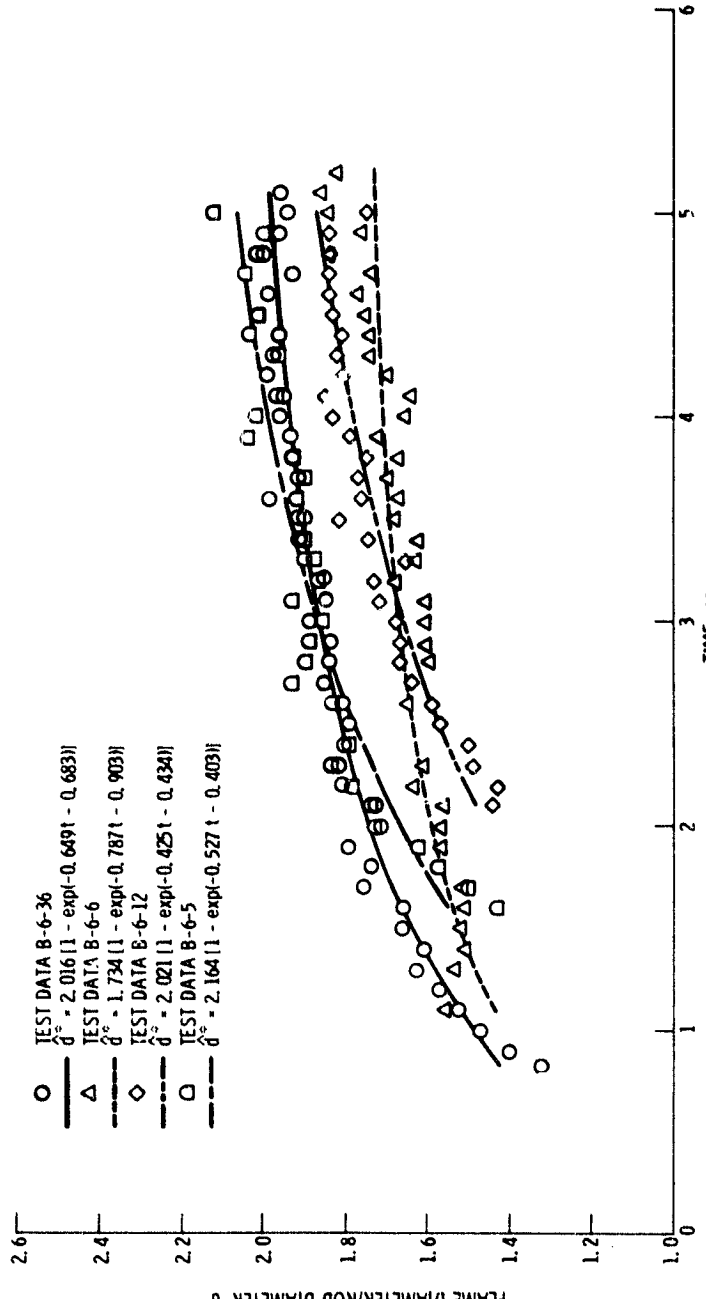

Figure 31. - Comparison of experimental data and curve fit for 0.615 cm (0.242 in.) diameter rod burned in 3.45x10^4 N/m^2 (5 psia) oxygen.

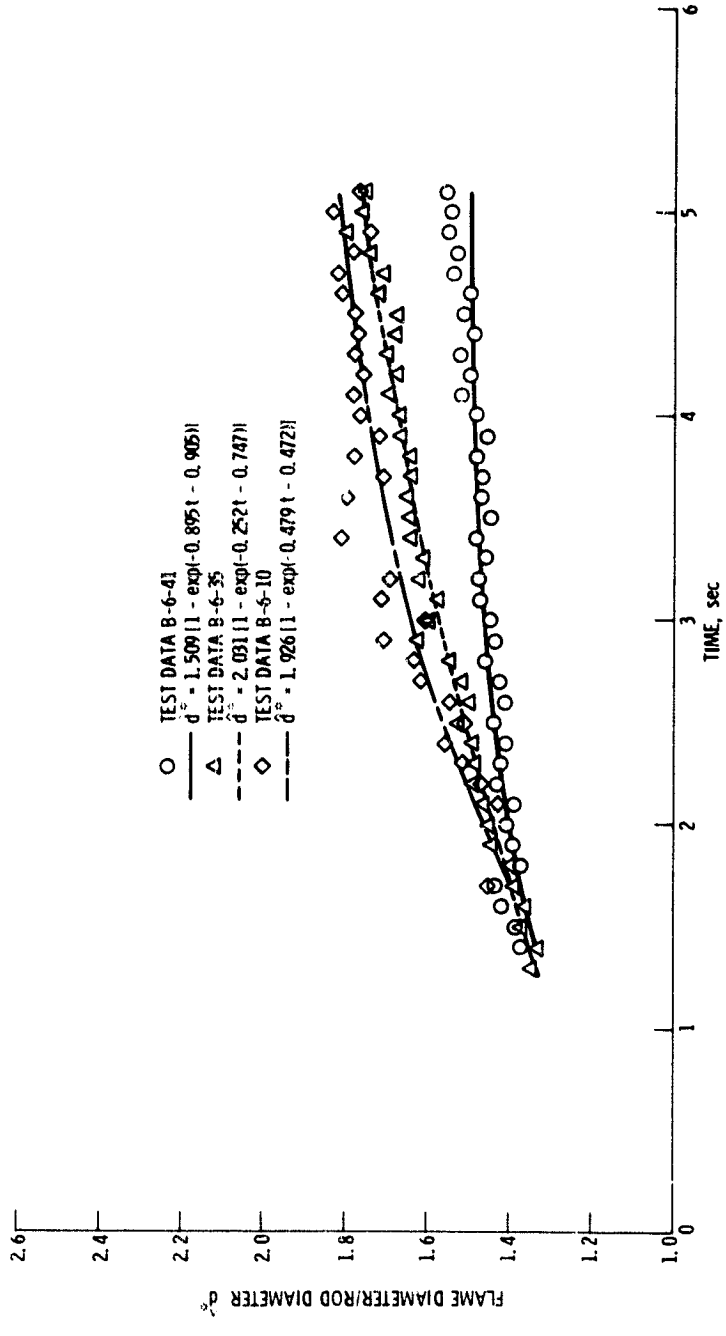

Figure 32. - Comparison of experimental data and curve fit for 0.615 cm (0.242 in.) diameter rod burned in 6.89×10^4 N/m^2 (10 psia) oxygen.

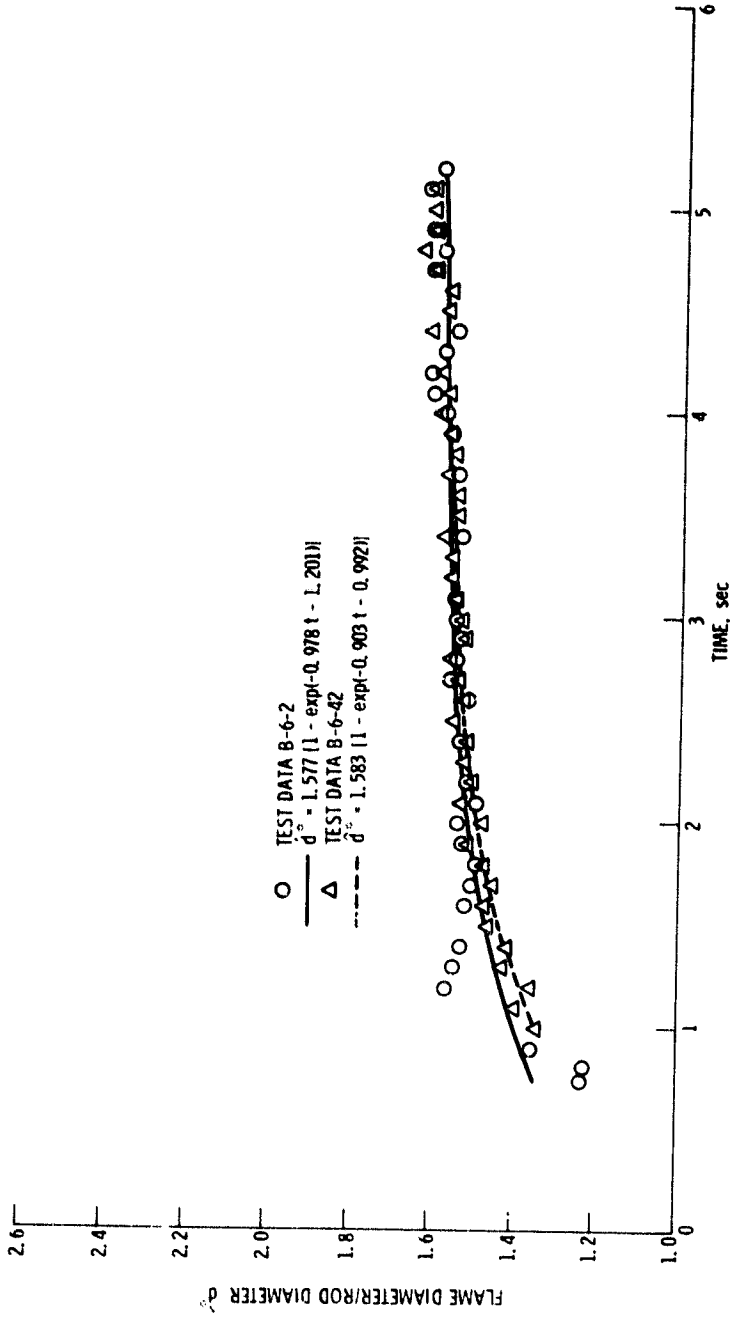

Figure 33. - Comparison of experimental data and curve fit for 0.615 cm (0.242 in.) diameter rod burned in 1.03x10^5 N/m^2 (15 psia) oxygen.

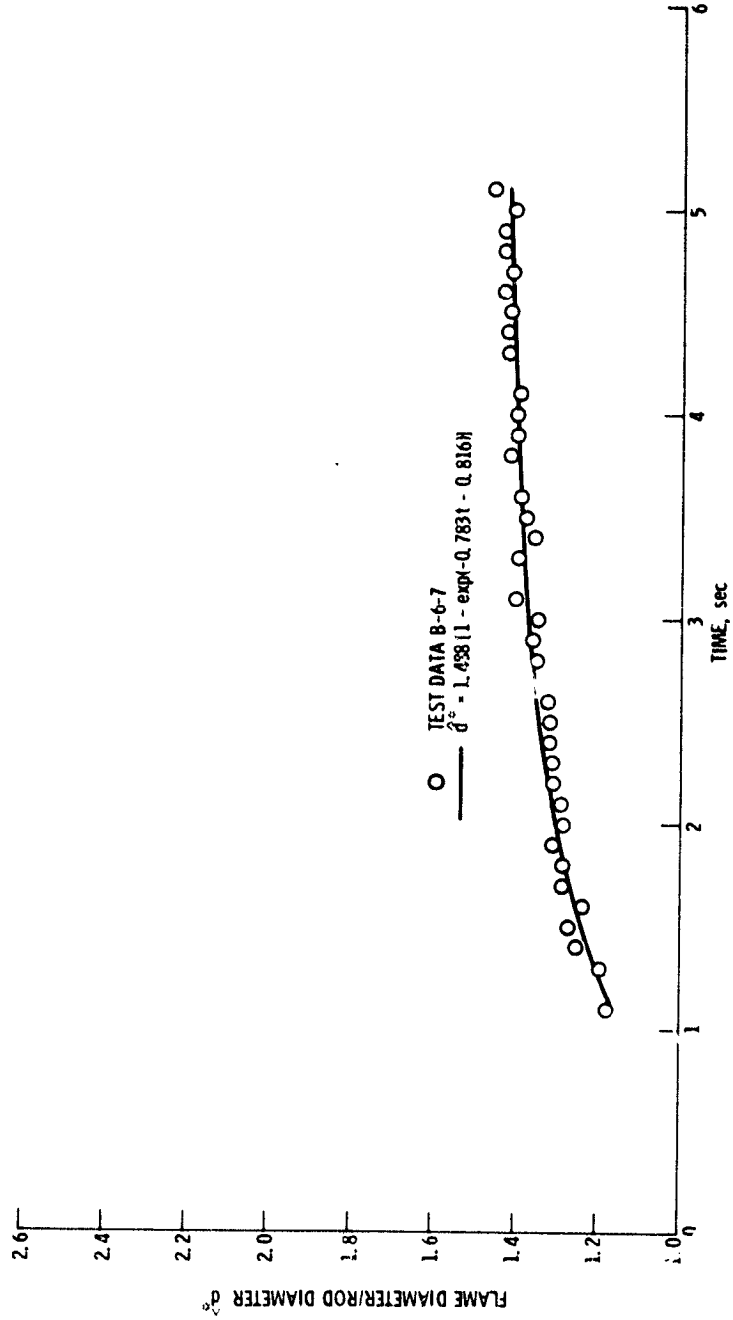

Figure 34. - Comparison of experimental data and curve fit for 0.615 cm (0.242 in.) diameter rod burned in 1.38x10^5 N/m^2 (20 psia) oxygen.

have the same ratio of flame diameter to rod diameter for tests conducted at the same pressure and with the same diameter rods.

The coefficients from the curve fit equations were used to obtain a correlation equation for all the data. The equation obtained is:

$$\hat{d}^* = \alpha(1 - e^{-\phi_1 t - \phi_2})$$

$$\text{where } \alpha = 1.943 - 6.599(d - 0.18) - 0.03517\,(P - 12.5) + 46.69(d - 0.18)^2$$

$$\phi_1 = 0.687$$

$$\phi_2 = 1.015 + 4.335(d - 0.18) + 0.0278(P - 12.5) - 119.4(d - 0.18)^2$$

The units of d (rod diameter), P (pressure), and t (time) are in., psia, and sec, respectively.

The standard deviations of α, ϕ_1, and ϕ_2 about the regression line are 0.201, 0.219, and 0.196, respectively. The coefficients in α and ϕ_2 are those that had a T ratio greater than 1.98. Only the 46.69 coefficient in α had a value this low, with all others being greater than two. The T ratio, which is the coefficient divided by the standard deviation, indicates if there is a relationship between the variables. The larger the value of T, the better the relationship. If T is less than 2, there is no relationship, and if it is greater than 2, there is a relationship. Because only the first coefficient in ϕ_1 had a T value greater than 2, the mean value of ϕ_1 was used.

The data along with the correlation equation are presented in Figures 35 through 38. The data on each of the figures is presented with a constant pressure and variable rod diameter. In Figure 35, it can be seen that at 3.45×10^4 N/m^2 (5 psia), the correlation equation fits the 0.305 cm (0.120 in.) diameter rod data, but is slightly higher than the 0.457 cm (0.180 in.) and the 0.615 cm (0.242 in.) diameter rod data. Figure 36 shows that at 6.89×10^4 N/m^2 (10 psia), the correlation equation fits the 0.305 cm (0.120 in.) and the 0.457 cm (0.180 in.) diameter rod data, while it is slightly higher than the 0.615 cm (0.242 in.) diameter rod data. In Figure 37, it can be seen that at 1.03×10^5 N/m^2 (15 psia), that the 0.305 cm (0.120 in.) diameter rod data does not exactly follow the correlation equation, and the correlation equation is slightly lower than the 0.457 cm (0.180 in.) diameter rod data. The correlation does fit the 0.615 cm (0.242 in.) diameter rod data for times grater than 2.5 seconds. Figure 38 shows that at 1.38×10^5 N/m^2 (20 psia), the correlation equation fits the 0.615 cm (0.242 in.) and the 0.457 cm (0.180 in.) diameter rod data, but the 0.305 cm (0.120 in.) diameter rod data falls below the correlation equation. From Figures 35 through 38, it can be concluded that, in general, the correlation equation predicts the ratio of flame diameter to rod diameter (d*) within approximately ± 0.1, except for the 1.38×10^5 N/m^2 (20 psia) data for the 0.305 cm (0.120 in.) rod where the correlation equation and the ratio of flame diameter to rod diameter vary by as much as ± 0.25.

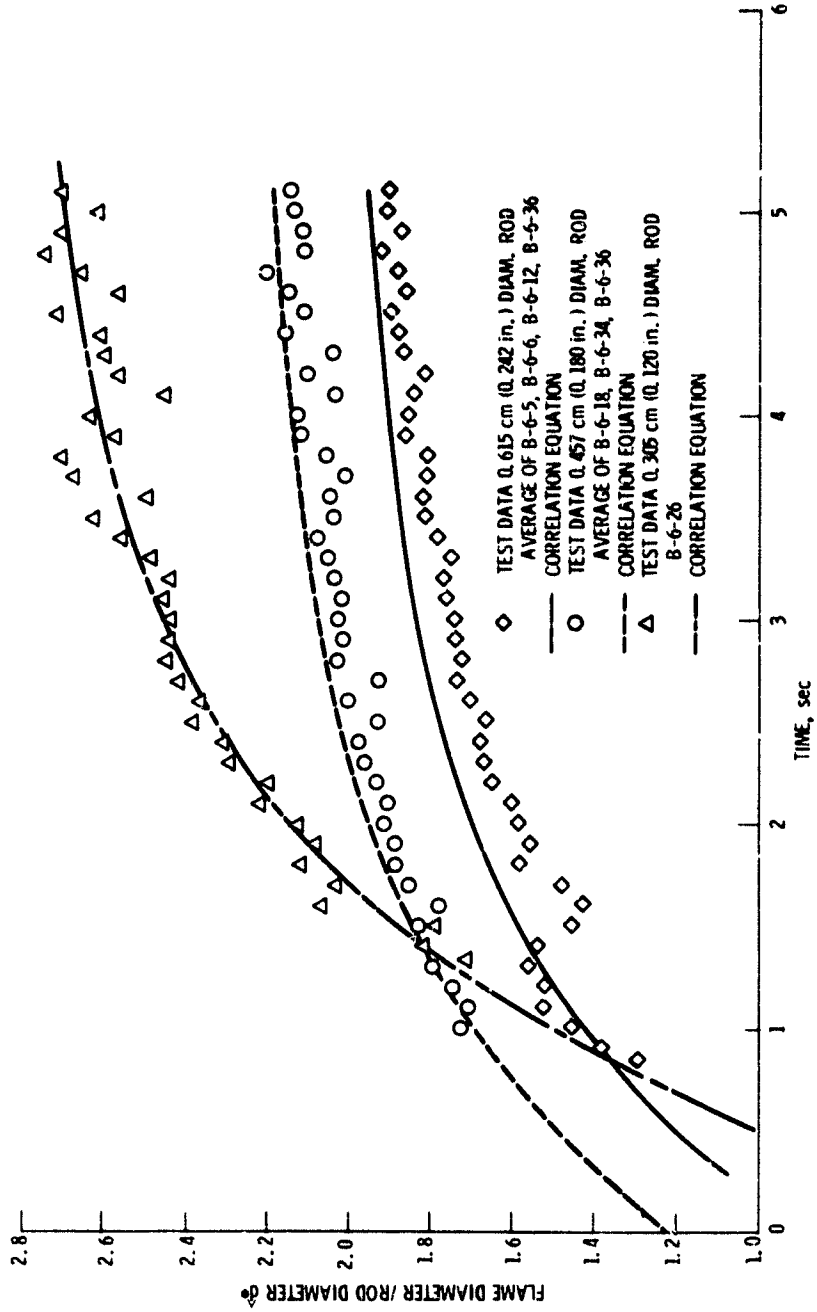

Figure 35. - Comparison of experimental data and correlation equation for rods burned in 3.45×10^6 N/m^2 (5 psia) oxygen.

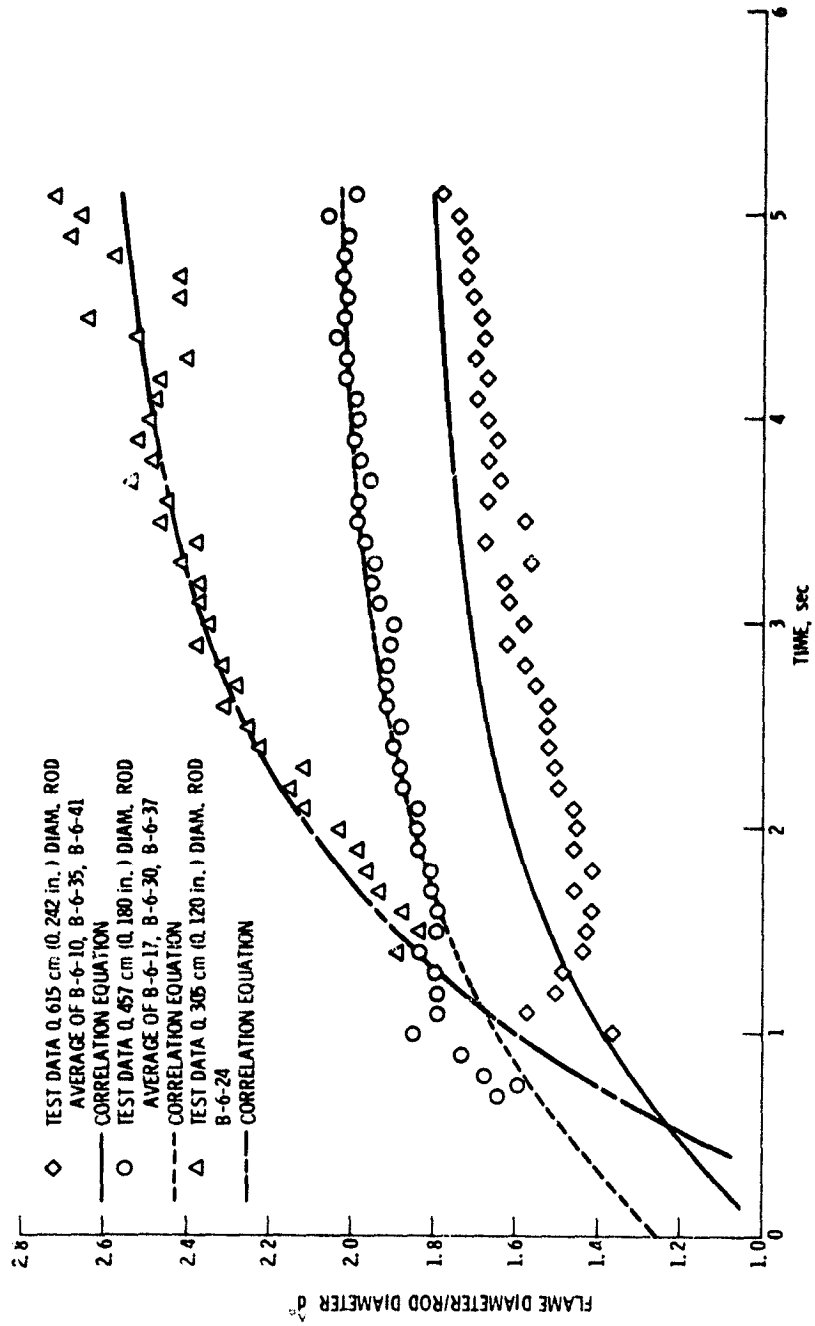

Figure 36. - Comparison of experimental data and correlation equation for rods burned in 6.89x10^4 N/m^2 (10 psia) oxygen.

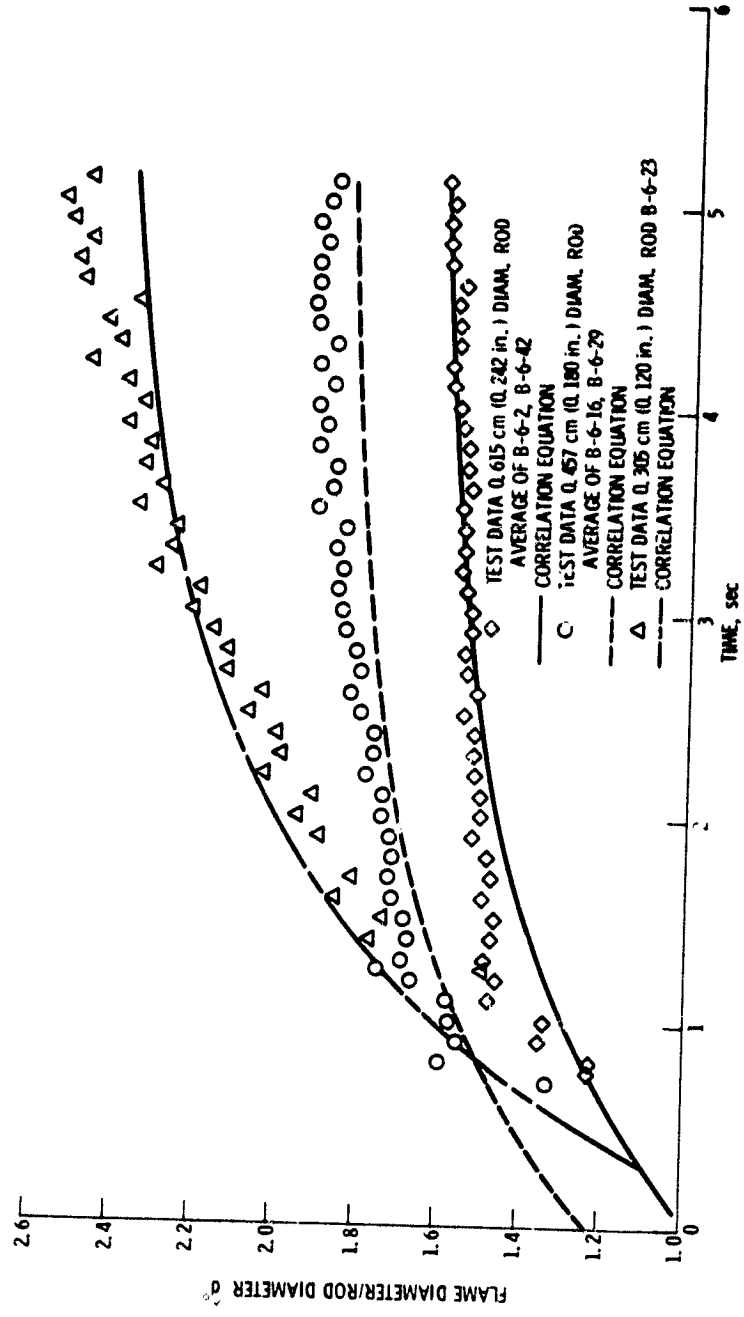

Figure 37. - Comparison of experimental data and correlation equation for rods burned in 1.03x10^5 N/m^2 (15 psia) oxygen.

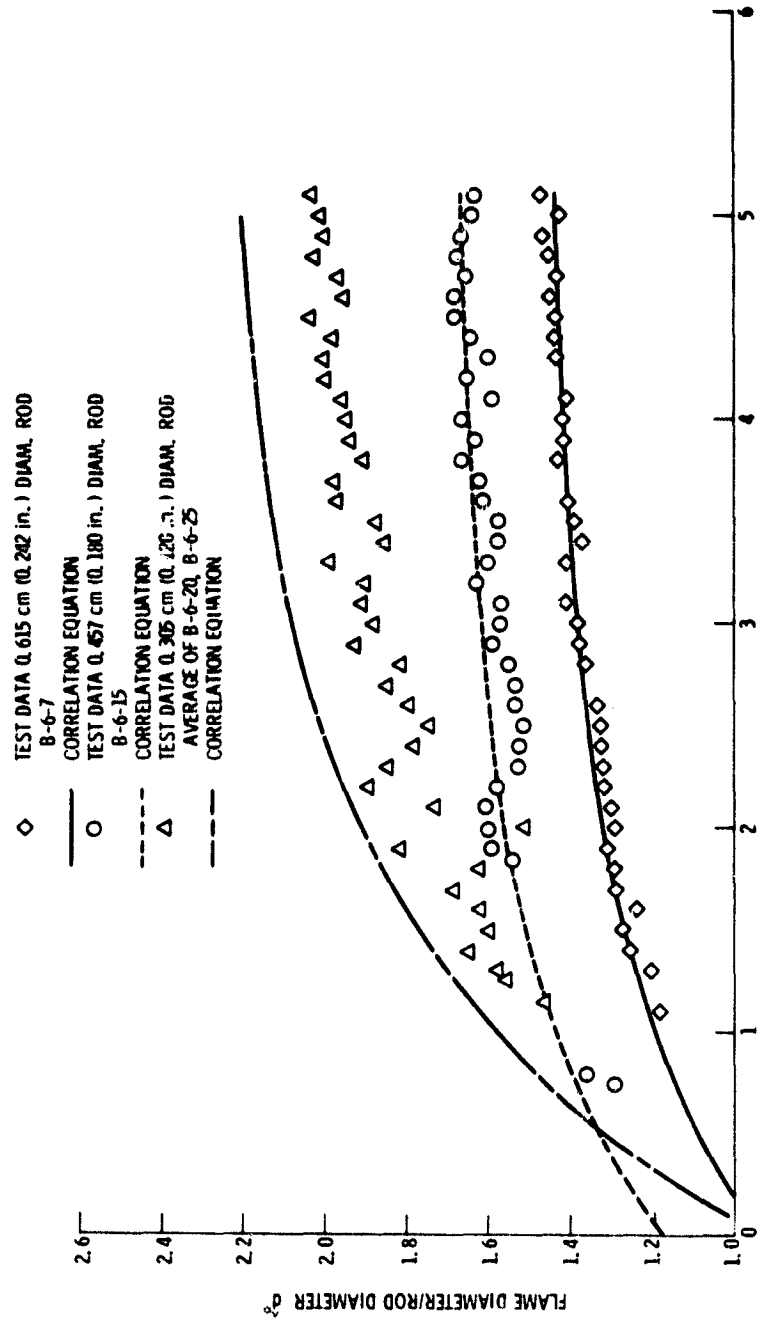

Figure 38. - Comparison of experimental data and correlation equation for rods burned in 1.38×10^5 N/m^2 (20 psia) oxygen.

G. Conclusions for Zero Gravity Tests

A blue flame surrounding the carbon rod under zero-gravity conditions showed that a gas phase reaction occurred, in which carbon monoxide was oxidized to carbon dioxide. This means that the carbon rod was burning according to one of the high temperature models that allows a gas phase reaction. Because the flame extended from the surface of the rod, the carbon would seem to be burning according to the models presented by Hugo, Wicke, and Wurzbacher [4] or Caram and Amundson [6]. If the flame had not extended from the surface, that is, if it stood off from the surface, the carbon would be burning according to the models presented by Spalding [7] or van der Held [8]. It was not possible to obtain the surface temperature in the zero-gravity tests. From the zero-gravity data, it was found that the ratio of flame diameter to rod diameter increased as the pressure decreased, and decreased as the rod diameter increased. The data was used to obtain the correlation equation:

$$\hat{d}^* = \alpha(1 - e^{-\phi_1 t - \phi_2})$$

where $\alpha = 1.943 - 6.599(d - 0.18) - 0.03517\ (P - 12.5) + 46.69(d - 0.18)^2$

and $\phi_1 = 0.687$

$\phi_2 = 1.015 + 4.335(d - 0.18) + 0.0278(P - 12.5) - 119.4(d - 0.18)^2$

The units of d (rod diameter), P (pressure), and t (time) are in., psia, and sec, respectively. In general, this equation predicts the ratio of flame diameter to rod diameter (d*) within approximately ± 0.1, except at 1.38×10^5 N/m^2 (20 psia) for a rod diameter of 0.305 cm (0.120 in.), where the deviation approaches ± 0.25. The information obtained from this experiment can be used to properly design an in-space experiment, such as for Spacelab, where long-term zero-gravity information on the combustion process can be obtained. The long-term zero-gravity data should include surface temperatures and temperature and concentration profiles, which are needed to accurately model the zero-gravity combustion process. The concentration profiles would confirm which carbon-burning model is correct. If the O_2 concentration extended to the surface of the rod, the models presented by Hugo, Wicke, and Wurzbacher [4] or Caram and Amundson [6] would be correct. If the O_2 concentration goes to zero before the surface of the rod is reached, the models presented by Spalding [7] or van der Held [8] would be correct.

IV. NORMAL GRAVITY EXPERIMENTATION

A. Apparatus

The experimental system used to study the products of combustion from a burning carbon rod in normal gravity consisted of a carbon rod igniter and a modulated beam mass spectrometric sampler.

The carbon rod igniter and holder is shown in Figure 39. In all of the normal gravity tests, 0.615 cm (0.242 in.) diameter by 5.08 cm (2.0 in.) long carbon rods were used. The carbon rod was held by two tungsten electrodes, which were 0.160 cm (0.063 in.) in diameter and extended through two copper poles. The center of the carbon rod was 6.1 cm (2.4 in.) above the flow straightener. A glass cylinder with a 10.80 cm (4.25 in.) inside diameter and a height of 11.43 cm (4.5 in.) covered the carbon rod holder.

The rods were burned at atmospheric pressure in oxygen with a water vapor content of 6 ppm. A volumetric flow rate of 0.15 l/sec (0.005 ft^3/sec) was set by a needle valve and measured with a calibrated rotameter. This volumetric flow rate, which had to be used to make up for the gases drawn off by the sampling probe, corresponded to a 4.35 cm/sec (0.159 ft/sec) flow rate past the rod. The oxygen entered through the bottom of the lower section of the carbon rod holder, which was a 7.62 cm (3.0 in.) long cylinder with a 6.86 cm (2.7 in.) inside diameter. The oxygen flowed through a screen and

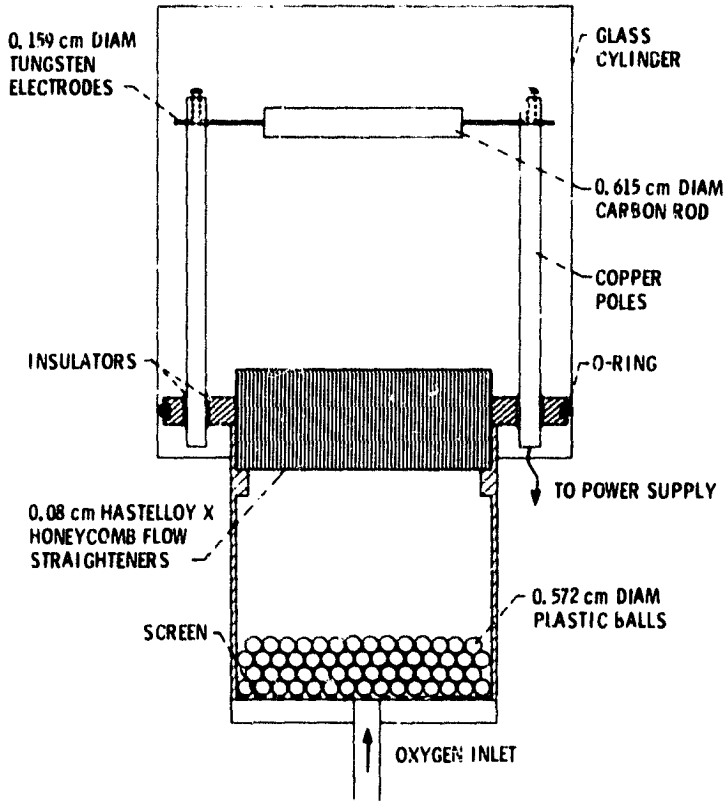

Figure 39. - Schematic of carbon rod burning apparatus.

then through a section containing plastic balls, 0.572 cm (0.225 in.) in diameter, in order to spread the flow. Finally, the oxygen passed through a Hastelloy X honeycomb flow straightener. The flow straightener had honeycomb openings 0.08 cm (0.031 in.) on a side with 135 openings/cm^2 (871 openings/$in.^2$), giving an open area of 29.31 cm^2 (4.543 $in.^2$). The burner was supported by mechanical devices which facilitated micrometer movement in three mutually perpendicular directions. Power to ignite the carbon rod was supplied by a 48 volt power supply.

Direct mass spectrometric analysis of the species in the atmospheric pressure flame surrounding the carbon rod was accomplished with a modulated molecular beam mass spectrometer sampler, shown in Figure 40. The sampler is described in more detail in Reference [38] and is shown schematically in Figure 41. Atmospheric pressure sampling was accomplished by drawing a gas sample through either a 0.20 mm (0.008 in.) diameter Pt-10% Rh orifice shown in Figure 41, or through a quartz sampling probe with a 0.20 mm (0.008 in.) diameter orifice shown in Figure 42. Quartz sampling probes with orifice diameters of 0.03 mm (0.001 in.), 0.13 mm (0.005 in.), and 0.25 mm (0.010 in.) were also tried. The smaller probes (0.03 mm and 0.13 mm) plugged up with small flakes from the carbon surface and the 0.25 mm orifice was so large that the sampling system could not be pumped down. The Pt-10% Rh orifice was used to obtain samples at the top of the rod (the 0^o position), and the quartz probe was used to obtain samples at positions of 45^o and 90^o from the top of the rod.

To sample the center portion of the flow from the sampling orifice or probe, the stream was passed through a skimmer cone with an

Figure 40. Mass spectrometric sampler.

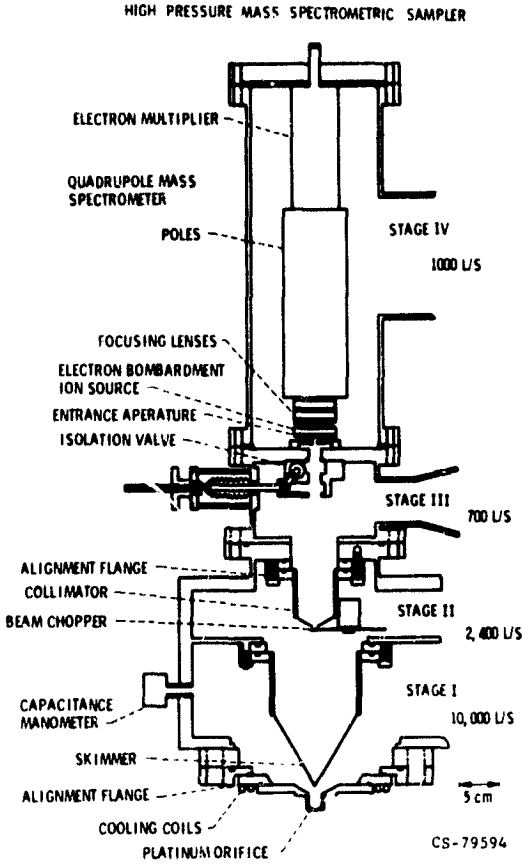

Figure 41. - Schematic of spectrometric sampler.

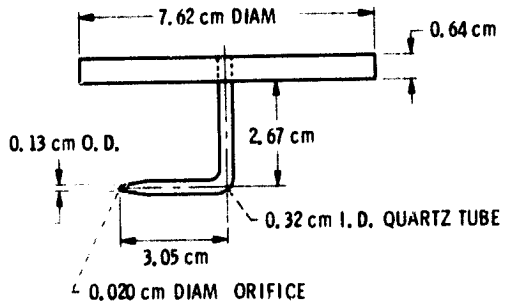

Figure 42. - Quartz gas sampling probe.

orifice diameter of 0.81 mm (0.032 in.) and an included angle of 60^{o}. The distance between the sampling orifice or the top plate of the quartz sampling probe and the skimmer orifice was 3.18 cm (1.25 in.). For this physical configuration with nominal pumping speeds indicated in Figure 41, first and second stage pressures were approximately 1.5×10^{-3} torr and 8×10^{-6} torr, respectively, when sampling room temperature, atmospheric pressure gas. When the gas temperature was increased to 1000° C, these pressures were 7×10^{-4} torr and 1×10^{-6} torr, respectively. Third and fourth stage pressures were always less than 10^{-7} and 10^{-8} torr, respectively, for all sampling conditions. Stage I pressures were read with a capacitance manometer, and the pressures in the other three stages were read with ion gauges. The molecular beam from the skimmer was chopped by a motor driven two-toothed chopper wheel located in Stage II. A chopping frequency of 150 Hertz was used and a reference signal at this frequency was derived from a light bulb and photodiode coupled to the chopper wheel. The chopped molecular beam then passed to the electron bombardment ion source of a quadrupole mass spectrometer. The quadrupole filter with 1.6 cm diameter poles had a mass range extending to over 600 AMU. A Channeltron electron multiplier was employed to multiply the ion current output of the ion source-quadrupole filter. Two channels of current output were measured as a function of quadrupole filter tuning. One channel measured the total chopped ion current, and the other channel measured only the component of the ion current signal in phase with the chopper. The second channel was driven by a lock-in amplifier-phase sensitive detector system tuned to the chopper frequency reference signal. The gaseous species in the flame were

measured by recording the in-phase component of the ion current for respective values of the mass to charge ratio. The accuracy of the mole fractions obtained is uncertain because the system was not calibrated for such mass dependent factors as quadrupole mass filter transmission, multiplier gain, or Mach number focusing. However, because the mass range used was narrow, 26 to 46 AMU, the errors associated with mass dependent factors are estimated to be less than 10 percent.

B. Test Procedure

The sampling orifice to be used in the test was attached to the mass spectrometric sampler. The sampling apparatus was pumped down and put into operation and the sampling orifice position was adjusted. The adjustment was made while ambient laboratory air was being sampled. The mass filter was set on the maximum of the nitrogen peak and the electrometer output on the recorder was observed while adjusting the sampling orifice centering screws. Adjustments were made to maximize the nitrogen signal. The quadrupole mass filter range was set for the range of 26 to 46 AMU with a rate of 0.2 sec/AMU, so spectra were recorded every four seconds.

The holes in the ends of the carbon rods were filled with silver brazing powder before the rod was put into the carbon rod holder in order to reduce the contact resistance between the electrodes and the rod.

For the tests where gas samples were taken at the top of the rod, the glass cylinder was moved up to the plate holding the orifice, and

the carbon rod was positioned 0.69 cm (0.27 in.) below the sampling orifice. After the rod was ignited, it was moved toward the sampling orifice. At least two spectra were taken at each position to which the carbon rod was moved. The distance the carbon rod was moved was measured with a dial indicator that had increments of 0.003 cm (0.001 in.). For the tests where the quartz probe was used to sample the gases, the probe was set 0.025 cm (0.010 in.) from the surface and left at this position while the rod burned. Because the quartz sampling probe was lower than the Pt-10% Rh probe, the glass cylinder was open at the top. To eliminate ambient air from entering the carbon rod holder, aluminum foil with a slot in it for the sampling probe was placed on top of the glass cylinder.

Before a rod was ignited, the carbon holder was purged with oxygen. The gas species in the carbon holder assembly were monitored with the mass spectrometer. The rod was ignited when oxygen was the only gas present in the assembly, with ignition obtained by passing an electric current through the rod. Power was supplied by a 48 volt power supply, and the power was left on until a flame appeared around the carbon rod.

C. Data Reduction

The ion intensities were corrected for relative ionization cross sections. Cross sections for atoms were taken from Mann [39] and estimated for molecules as 0.75 times the sum of the atomic values. Because it was impossible to photograph the center of the rod where the samples were taken while the carbon holder assembly was in position in

the mass spectrometer system, the carbon holder assembly was pulled out and three rods were burned in it and photographed from above and from the side. One of the rods had a flame only over the top surface. Of the other two rods, only one was photographed until it completely burned. A side view of the carbon rod burning is shown in Figure 43. The respective diameters of this rod as a function of time for the two viewing positions are presented in Figure 44. It can be seen that the sides of the rod (top view) burned faster than the top and bottom combined (side view). Also, the side view change of position of the horizontal centerline of the rod from its original position is shown in Figure 45. This figure shows that the bottom of the rod burned faster than the top. Based on the data in Figures 44 and 45, the rod became elliptical as it burned. To determine the probe distance from the surface, the diameters of the rod at the time the spectra were taken were used to determine the surface position of the ellipse. The change in surface position between the original carbon surface and the elliptical surface was added to the original probe position to get the horizontal distance between the probe and the surface.

D. Experimental Results and Discussion

Concentration profiles of the combustion products of a carbon rod as a function of distance from the surface were obtained for initial sampling probe positions of 90^{o}, 45^{o}, and 0^{o}, with 0^{o} being the top of the rod. As stated previously, the lower part of the rod burned faster than the top of the rod, so that the angle of the probe

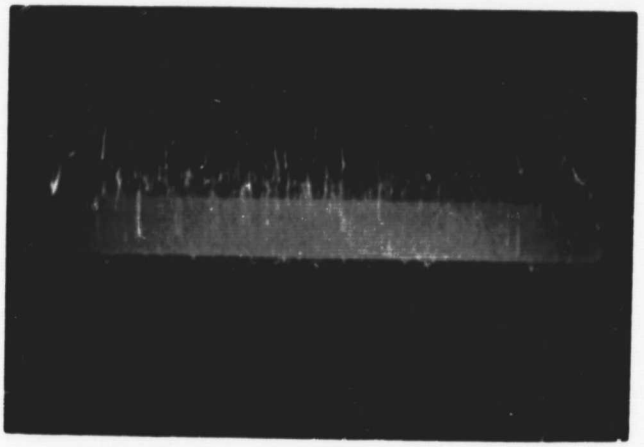

Figure 43. - Side view of carbon rod burning.

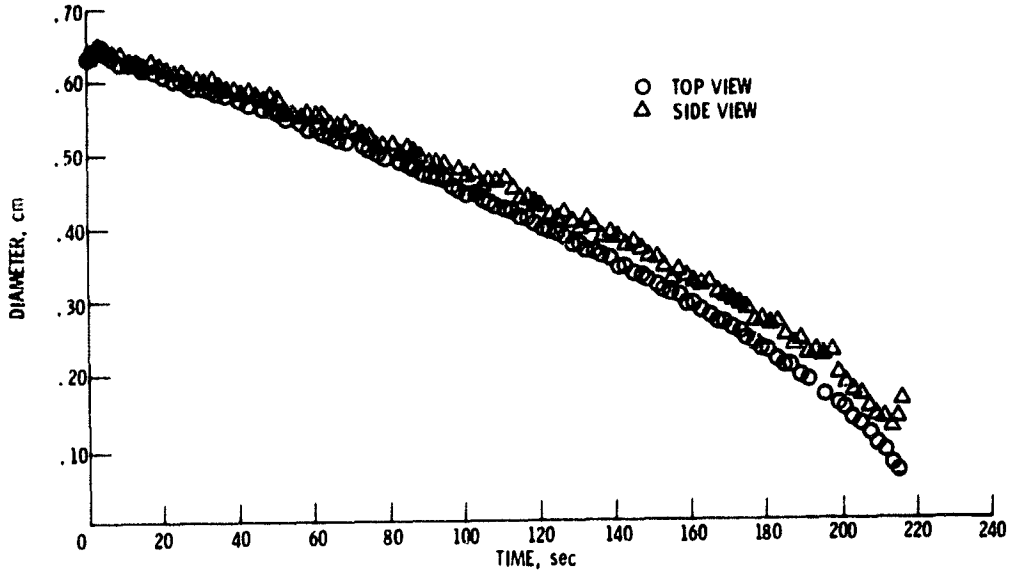

Figure 44. - Diameters of burning rod as a function of time.

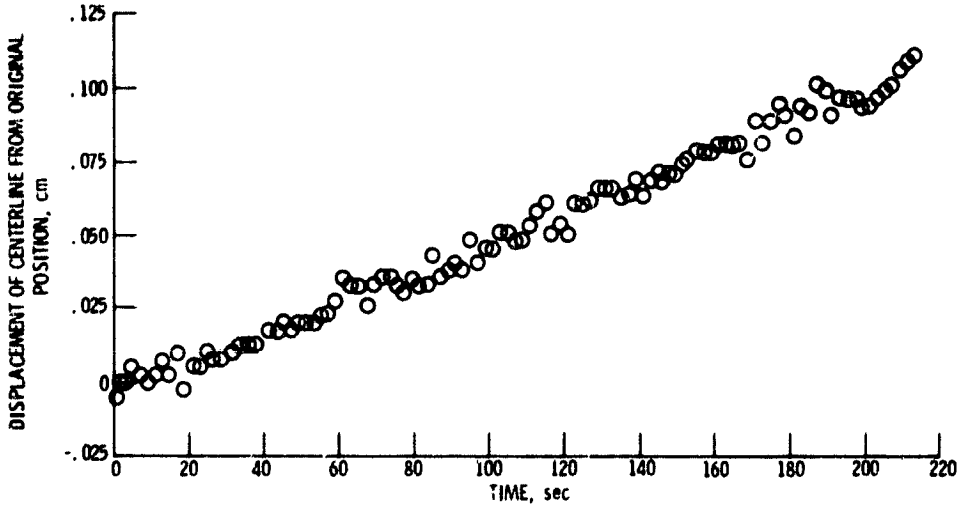

Figure 45. - Change in position of horizontal centerline of rod from its original position as a function of time.

initially positioned at 45^0 and 90^0 changed as the rod burned. In Figure 46, the concentrations of O_2, CO_2, and CO as a function of distance from the surface for the 90^0 quartz sampling probe are presented. The O_2 concentration increases with distance from the surface, while the CO concentration decreases with distance from the surface. The CO_2 concentration at first increases slightly and then decreases with distance. The concentration of CO is lower than the concentration of CO_2 except near the surface, that is, less than 0.05 cm (0.02 in.) from the surface. Also, at this distance the concentration of CO_2 can be seen to level off. None of the concentrations seem to go to zero at the surface, which indicates that the surface conversion process at this position was chemical process or, neglecting the chemisorption and desorption steps, chemical reaction rate controlled rather than mass transfer controlled.

The concentration profiles obtained with the quartz probe at the 45^0 position are presented in Figure 47. Again, the O_2 concentration increases with distance from the surface, while both the CO_2 and CO concentrations decrease with distance. The O_2 concentration is lower than the CO_2 and CO concentrations very close to the surface, and the CO concentration is always lower than the CO_2 concentration. The concentrations, if extrapolated to the surface, do not appear to equal zero, but the O_2 profile does indicate that it would have a low value. This again indicates a chemical reaction rate controlled surface conversion at the 45^0 probe position.

The concentration profiles obtained with the Pt-10% Rh probe at the top of the rod are presented in Figure 48. At this position, as at the other positions, the O_2 concentration increases with distance

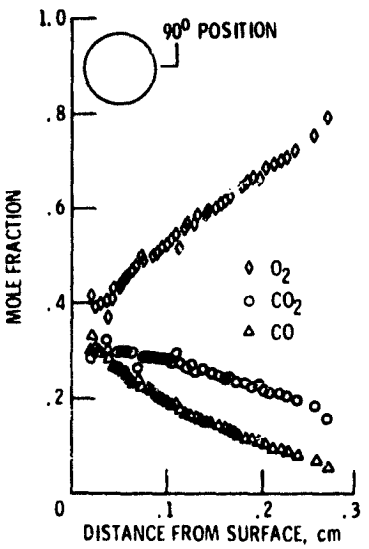

Figure 46. - Concentration as a function of diatance from surface-probe at 90°.

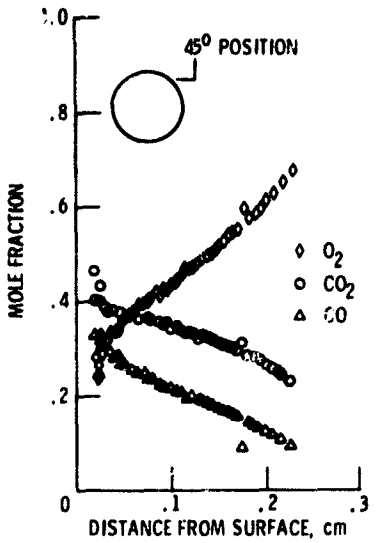

Figure 47. - Concentration as a function of distance from surface-probe at 45°.

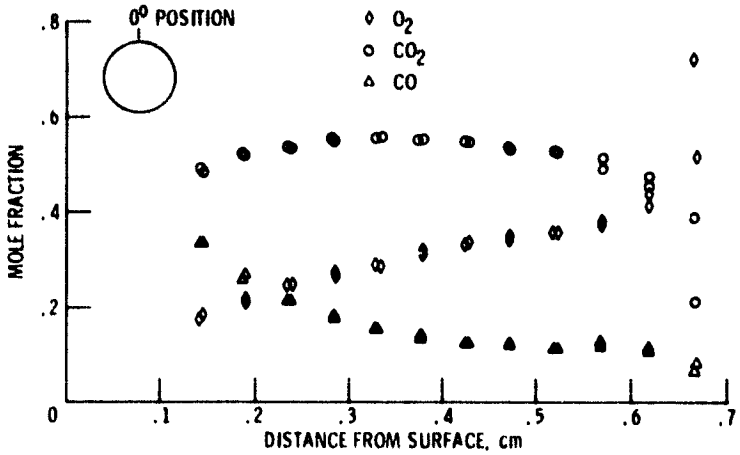

Figure 48. - Concentration as a function of distance from surface probe at 0°.

while the CO concentration decreases. The CO_2 at first increases with distance from the surface, reaching a maximum at approximately 0.36 cm (0.14 in.) from the surface, and then starts to decrease. The concentration of CO_2 is higher than that of the other species except for O_2 at large distances from the surface, greater than 0.64 cm (0.25 in.). The rate of CO concentration decrease is more rapid near the surface than away from the surface. The concentration of O_2 is lower than the concentration of CO or CO_2 near the surface, approximately 0.20 cm (0.08 in.) from the surface. Also, at 0.64 cm (0.25 in.), there is a rapid increase in the O_2 concentration and a corresponding rapid decrease in the CO_2 concentration, indicating that the ambient oxygen in the carbon rod holder assembly is mixing with the combustion products. Data at distances less than 0.1 cm from the surface for the 0^o probe position could not be obtained, because by the time sampling this close to the surface could be done, the rod diameter was so small that ambient gas was being drawn into the probe.

The O_2 concentration as a function of distance from the surface for the three sampling positions is presented in Figure 49. The O_2 concentration decreases with position from 90^o to 0^o. The O_2 profile tends to reach the same value for the 90^o and 45^o probe positions at an approximate distance of 0.23 cm (0.09 in.) from the surface. If the concentrations are extrapolated to the surface, it can be seen that the surface concentration decreases considerably from the 90^o position to the 45^o position. It would be difficult to extrapolate the 0^o position to the surface, but if the trend set up by the 90^o and 45^o probe positions holds, it is very likely that at the 0^o position the surface concentration would go to zero. This

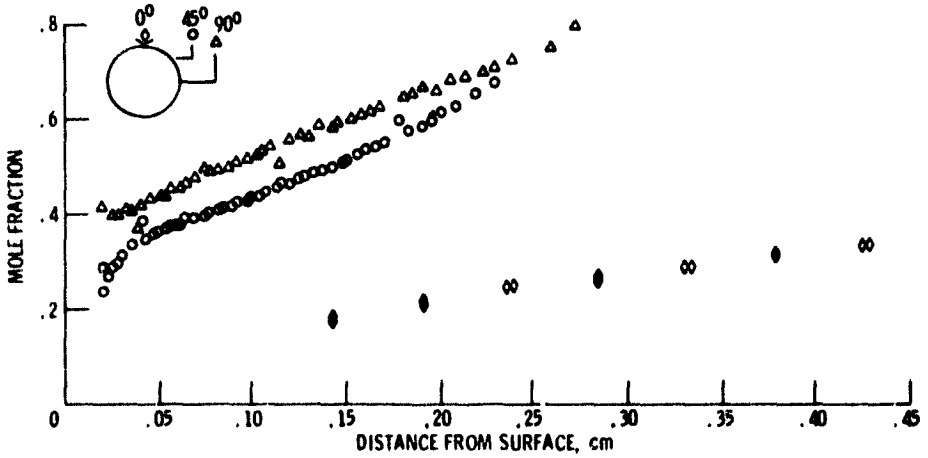

Figure 49. - O_2 concentration as a function of distance from surface for various gas sampling probe positions.

indicates that the oxygen conversion process at the surface is chemical reaction rate controlled at both the 90^0 and 45^0 probe positions, and that it is very possible that the process at the 0^0 probe position is mass transfer controlled.

The CO_2 concentration as a function of distance from the surface for the three probe positions is presented in Figure 50. The CO_2 concentration is higher for the 45^0 probe position than it is for the 90^0 probe position. The concentrations for these two positions tend to become equal to each other away from the surface, that is, at approximately 0.23 cm (0.09 in.) from the surface. The concentrations at the 0^0 probe position are greater than those at the other two probe positions. The positive slope of the CO_2 concentration profiles for the 90^0 and 0^0 probe positions indicates that the CO_2 is reacting at the surface to produce CO. The increase of CO_2 with position from the 90^0 to 0^0 indicates that the combustion products are being convected upward.

The CO concentration as a function of distance from the surface for the three sampling probe positions is shown in Figure 51. The concentrations of CO are approximately the same for the 90^0 and 45^0 probe positions, except at distances between 0.08 cm (0.03 in.) and 0.23 cm (0.09 in.) from the surface where the CO concentration is lower for the 90^0 probe position. The CO concentration at the 0^0 probe position is the highest. The data for the 45^0 and 90^0 positions are plotted in Figures 52(a) and (b). If the data are extrapolated to the surface, it can be seen that the surface concentration for the 45^0 probe position is greater than that at the 90^0 position. Therefore, the CO concentration at the surface increases with

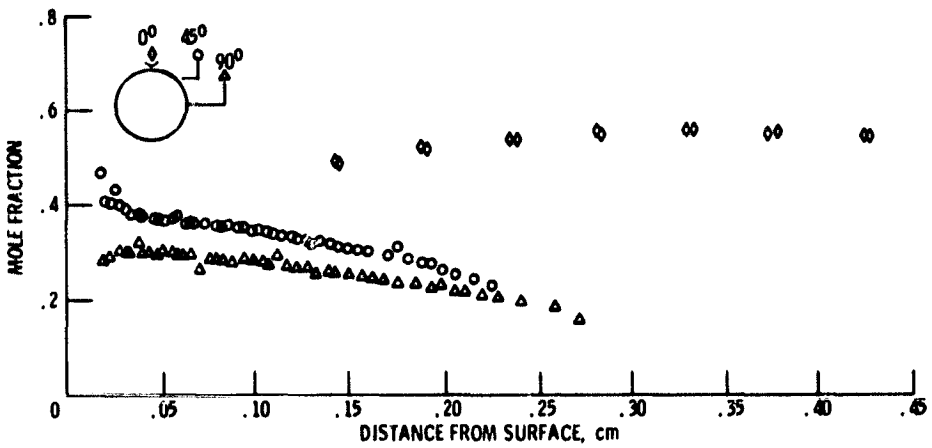

Figure 50. - CO_2 concentration as a function of distance from surface for various gas sampling probe positions.

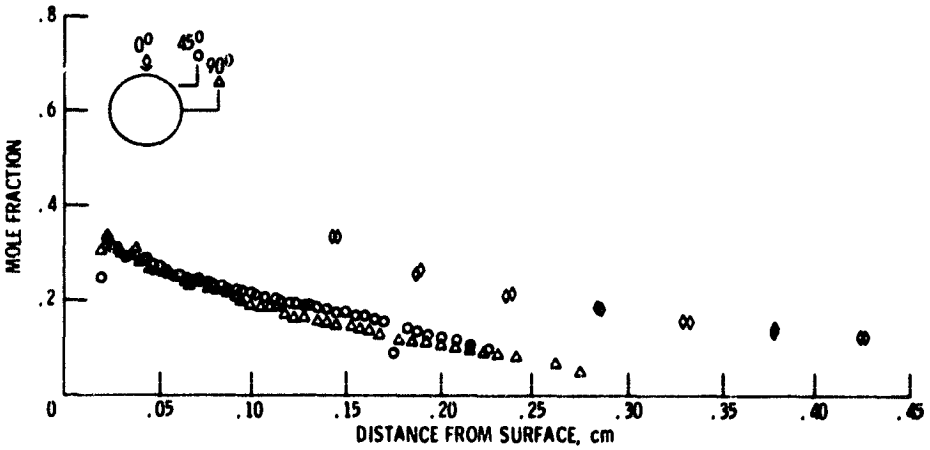

Figure 51. - CO concentration as a function of distance from surface for variuus gas sampling probe positions.

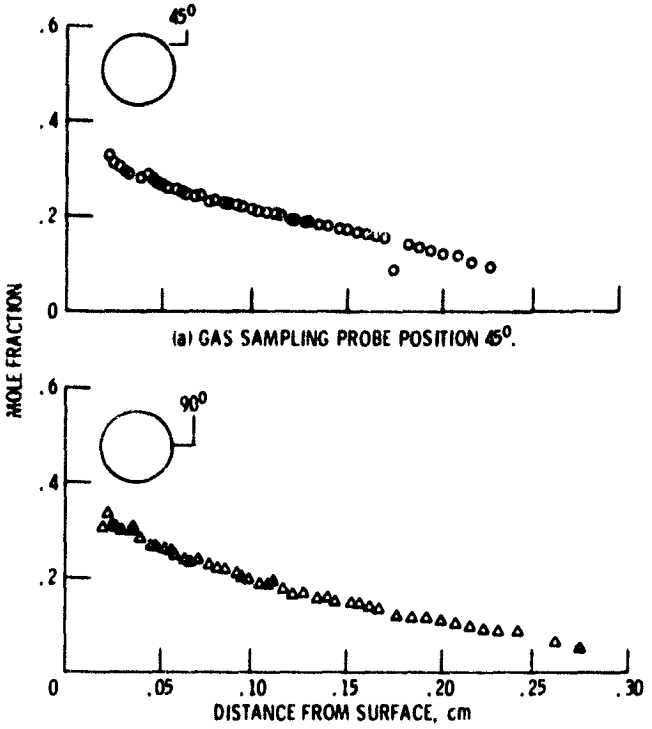

Figure 52. - CO concentration as a function of distance from surface.

position from the 90^{o} to 0^{o}. The increase in the CO concentration with decreasing angle can be attributed to convection of the combustion products upward and to the CO_2 reduction reaction with carbon, especially at the 0^{o} probe position.

The data from Figures 50 to 52 indicate that free convection played a major role in the combustion process. The decrease of O_2 with decreasing angle indicates that convected O_2 was reacting at the surface and that the O_2 could not be replenished by molecular diffusion. The increase in CO_2 with decreasing angle also shows this same result, even though it was reacting at the surface to produce CO. The data for the O_2 indicates a change in control mechanism from chemical reaction rate control at the lower sampling positions to mass transfer control at the top of the rod. This change of mechanism may also occur for the CO_2 at the 0^{o} position, but data near the surface that would be needed to verify this, could not be obtained.

Four tests were conducted in which a monochromatic optical pyrometer was used to determine the surface temperature. No gas samples were taken during these tests because the carbon rod holder assembly had to be removed from the mass spectrometer system. The same flow system was used and the conditions were kept the same as in the sampling tests. The time average surface temperature of the rod was found to be 1269° C, which is above the minimum surface temperature found in the literature for a gas phase reaction. There was only a few degree temperature difference between the bottom of the rod and the top of the rod.

E. Comparison with Previous Experimental Data

The concentration profiles obtained above for the horizontal rod can be compared to the concentration data of Wicke and Wurzbacher [5] for the midpoint of a 6 cm vertical rod with a surface temperature of 1230° C. In Figures 53 and 54 for the 90^{o} and 45^{o} probe positions, respectively, it can be seen that the CO_2 concentrations are considerably higher and the O_2 concentrations considerably lower for the vertical rod than for the horizontal rod. These differences are attributed to convective mass transfer. When compared to a diameter of 0.615 cm for the horizontal rod, the 6 cm length of the vertical rod allowed a greater distance for the build up of combustion products, especially CO_2. This would cause the increase in the CO_2 concentrations and the decrease in the O_2 concentrations. The CO concentrations for the vertical rod are higher than that for the horizontal rod, but the difference is considerably less than that for the CO_2 and O_2 concentrations. This indicates that CO is least affected by convective mass transfer. In Figure 55, the data taken at the 0^{o} probe position for the horizontal rod are compared to the data for the vertical rod. Since convective effects for the horizontal rod were maximized at this 0^{o} position, the data for the two rods should be more in agreement than for the 90^{o} and 45^{o} probe positions. This is seen to be true in Figure 55. For the vertical rod the CO_2 concentration rises more rapidly from the surface, reaching a maximum at approximately 0.25 cm from the surface, while the CO_2 concentration for the horizontal rod reaches a maximum at approximately 0.36 cm from the surface. For the vertical rod the

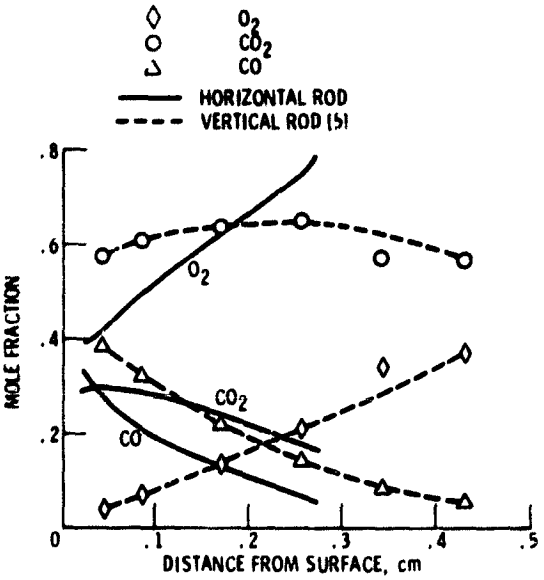

Figure 53. - Comparison of horizontal rod data with vertical rod data - 90^0 probe position.

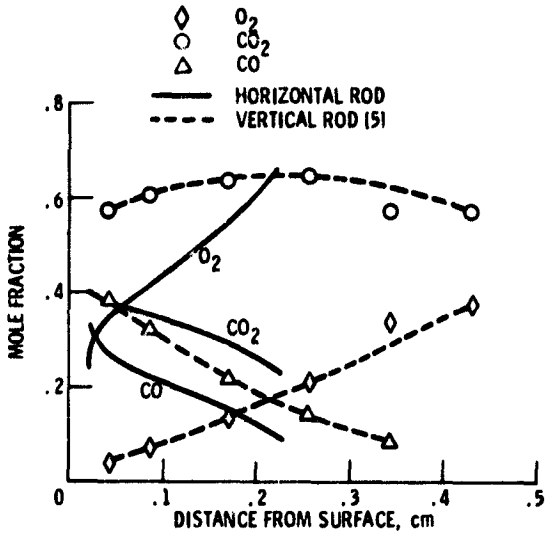

Figure 54. - Comparison of horizontal rod data with vertical rod data - 45° probe position.

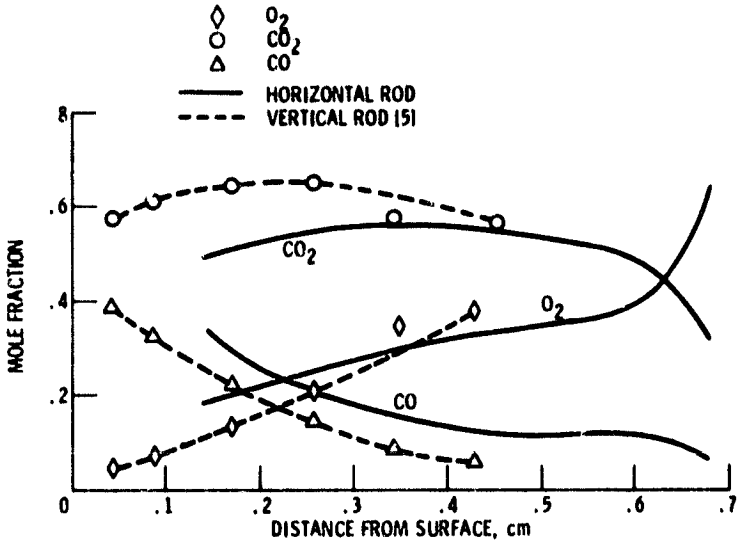

Figure 55. - Comparison of horizontal rod data with vertical rod data - 0^{0} probe position.

CO_2 concentrations were higher and the CO concentrations lower than for the horizontal rod. The O_2 concentrations for the vertical rod are initially lower than that for the horizontal rod, but become higher at approximately 0.36 cm from the surface. These differences in the data can be caused by the differences in the boundary layers for the two rod orientations. The boundary layer above the horizontal rod should be considerably thicker than the boundary layer for the vertical rod. This would cause the CO_2 maximum to shift to a greater distance from the surface, the CO and CO_2 concentrations to decrease less rapidly, and the O_2 concentration to increase less rapidly with distance for the horizontal rod. The large decrease in CO_2, the decrease in CO, and the large increase in O_2 for the horizontal rod at distances greater than 0.64 cm from the surface is attributed to ambient O_2 mixing with the combustion gases. In general, for both rod orientations, the CO_2 concentrations increase with distance from the surface, reach a maximum and then decrease. Correspondingly, the O_2 concentrations increases with distance, and the CO concentrations decrease with distance from the surface. Considering the geometrical differences between the two experiments, the comparison of the data shows very good agreement as to the phenomena occurring during the combustion process.

F. Conclusions for Normal Gravity Tests

For carbon rods burning in a dry oxygen environment, there was a gas phase reaction in which CO was burned to CO_2. From the 90^o probe position to the 0^o (top of the rod) probe position, the O_2

concentration decreased, the CO_2 concentration increased, but is expected to be lowest near the surface at the top of the rod, and the CO concentration, in general, increased. This means that convective effects were playing a considerable role in the combustion process, decreasing the oxygen supply to the rod by convecting up the combustion products. This convective mass transfer process was considerably faster than the radial mass transfer process.

From the data presented in Table 2, it can be concluded that for a 0.615 cm diameter rod with a surface temperature of 1269° C, the combustion process should be controlled by the mass transfer process. However, the normal gravity data obtained in this study indicates that the combustion of the carbon rod was controlled by the chemical process, except near the top of the rod where it was controlled by mass transfer. The change in control mechanism is caused, as mentioned above, by the combustion products being convected upward so the O_2 could not easily reach the surface at the 0^o probe position. It should be mentioned that previous investigators have used the carbon burning rate to determine the controlling mechanism, and did not use gas sampling techniques.

Good agreement, especially at the 0^o probe position, was obtained between the experimental data from this study and that of Wicke and Wurzbacher [5], showing that both studies have observed the same burning phenomena.

V. MATHEMATICAL MODEL

In order to compare the normal gravity data with a high temperature mathematical model that accounts for a gas phase reaction, the analysis of Caram and Amundson [6] for slabs and spheres was extended to cylindrical rods. The following assumptions were made: (1) a stagnant film of thickness δ surrounds the carbon rod; (2) axial end effects are neglected; (3) the rod does not react internally and is impervious to mass transfer; (4) the species present are CO, CO_2, and O_2; (5) gas properties are constant; (6) the Schwab-Zeldovich approximation (that is, the diffusion coefficients are the same and equal to $(\lambda/\rho c_p)$) holds; (7) the process is steady state; (8) effective binary diffusion; (9) the flow is only in the radial direction; and (10) there are two surface reactions, $2C + O_2 \rightarrow 2CO$, and $C + CO_2 \rightarrow 2CO$, and a gas phase reaction $CO + 1/2\ O_2 \rightarrow CO_2$. The model is shown in Figure 56. The complete mathematical model derivation is given in the Appendix, with only the essentials of the solution being presented here.

A. Governing Equations and Numerical Solution

The equations governing this combustion process are as follows:

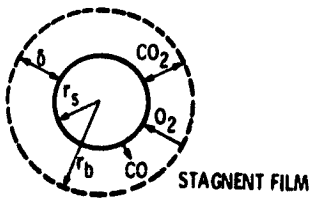

Figure 56. - Model of carbon combustion.

Mixture Continuity Equation:

$$\rho r v = \text{constant} = \dot{m} = M_c r_s (2\mathscr{R}_{O_{2S}} + \mathscr{R}_{CO_{2S}}) \qquad (1)$$

Species Continuity Equations:

$$\text{Oxygen: } \frac{\dot{m}}{r}\frac{dY_{O_2}}{dr} - \frac{\rho D_{O_2}}{r}\frac{d}{dr}\left(r\frac{dY_{O_2}}{dr}\right) = -R_{O_2} = -\frac{1}{2}M_{O_2}\mathscr{R}_{CO} \qquad (2)$$

$$\text{Carbon Dioxide: } \frac{\dot{m}}{r}\frac{dY_{CO_2}}{dr} - \frac{\rho D_{CO_2}}{r}\frac{d}{dr}\left(r\frac{dY_{CO_2}}{dr}\right) = R_{CO_2} = M_{CO_2}\mathscr{R}_{CO} \qquad (3)$$

$$\text{Carbon Monoxide: } \frac{\dot{m}}{r}\frac{dY_{CO}}{dr} - \frac{\rho D_{CO}}{r}\frac{d}{dr}\left(r\frac{dY_{CO}}{dr}\right) = -R_{CO} = -M_{CO}\mathscr{R}_{CO} \qquad (4)$$

and the Thermal Energy Equation:

$$\frac{\dot{m}c_p T_b}{r}\frac{d\tau}{dr} - \frac{\lambda T_b}{r}\frac{d}{dr}\left(r\frac{d\tau}{dr}\right) = \frac{H_{CO}\mathscr{R}_{CO}}{2} \qquad (5)$$

where ρ = density of the mixture;

r = radial distance from the center of the rod;

v = radial velocity;

$\dot{m}$ = carbon burning rate

M_C = molecular weight of carbon;

M_{O_2} = molecular weight of oxygen;

M_{CO_2} = molecular weight of carbon dioxide;

M_{CO} = molecular weight of carbon monoxide;

$\mathscr{R}_{O_{2S}}$ = surface molar reaction rate of oxygen;

$\mathscr{R}_{CO_{2S}}$ = surface molar reaction rate of carbon dioxide;

R_{O_2} = gas phase mass reaction rate of oxygen;

R_{CO_2} = gas phase mass reaction rate of carbon dioxide;

R_{CO} = gas phase mass reaction rate of carbon monoxide;

$\mathscr{R}_{CO}$ = gas phase molar reaction rate of carbon monoxide;

Y_{O_2} = mass fraction of oxygen;

Y_{CO_2} = mass fraction of carbon dioxide;

Y_{CO} = mass fraction of carbon monoxide;

D_{O_2} = effective binary diffusivity of oxygen;

D_{CO_2} = effective binary diffusivity of carbon dioxide;

D_{CO} = effective binary diffusivity of carbon monoxide;

c_p = specific heat of mixture;

T_b = temperature at the edge of the stagnant film;

τ = dimensionless temperature T/T_b;

λ = thermal conductivity; and

H_{CO} = heat of combustion of two moles of carbon monoxide.

The surface boundary conditions at $r = r_S$ assume that the flux of a species at the rod surface is equal to the surface reaction rate. The surface boundary conditions are

$$\text{Oxygen: } -\frac{\rho D_{O_2}}{M_{O_2}}\frac{dY_{O_2}}{dr}\bigg|_s + \frac{\dot{m}Y_{O_{2s}}}{M_{O_2}r_s} = -\mathcal{R}_{O_{2s}} \tag{6}$$

$$\text{Carbon Dioxide: } -\frac{\rho D_{CO_2}}{M_{CO_2}}\frac{dY_{CO_2}}{dr}\bigg|_s + \frac{\dot{m}Y_{CO_{2s}}}{M_{CO_2}r_s} = -\mathcal{R}_{CO_{2s}} \tag{7}$$

$$\text{Carbon Monoxide: } -\frac{\rho D_{CO}}{M_{CO}}\frac{dY_{CO}}{dr}\bigg|_s + \frac{\dot{m}Y_{CO}}{M_{CO}r_s} = 2\left(\mathcal{R}_{O_{2s}} + \mathcal{R}_{CO_{2s}}\right) \tag{8}$$

$$\text{Thermal Energy: } -\lambda T_b \frac{d\tau}{dr} = H_{O_2}\mathcal{R}_{O_{2s}} - H_{CO_2}\mathcal{R}_{CO_{2s}} \tag{9}$$

where H_{O_2} = heat produced by one mole of oxygen reacting with carbon to produce two moles of carbon monoxide; and

H_{CO_2} = heat absorbed by one mole of carbon dioxide reacting with carbon to produce two moles of carbon monoxide.

The boundary conditions at the edge of the stagnant film at $r = r_b$ are:

$$\text{Oxygen: } Y_{O_2} = Y_{O_{2b}} \tag{10}$$

$$\text{Carbon Dioxide: } Y_{CO_2} = Y_{CO_{2b}} = 1 - Y_{O_{2b}} \tag{11}$$

Carbon Monoxide: $Y_{CO} = 0$ (12)

Thermal Energy: $\tau = 1$ (13)

where $Y_{O_{2b}}$ and $Y_{CO_{2b}}$ are the ambient concentrations of oxygen and carbon dioxide, respectively. Equations (1) through (13) give a complete mathematical formulation of the problem.

Equations (2) and (3), (4) and (3), and (5) and (3) were combined to eliminate $\mathscr{R}_{CO}$. The equations were solved yielding

$$Y_{O_2} = -\frac{M_{O_2}}{2M_C} + \left(Y_{O_{2b}} + \frac{M_{O_2}}{2M_{CO_2}} Y_{CO_{2b}} + \frac{M_{O_2}}{2M_C}\right)\left(\frac{r}{r_b}\right)^{\gamma} - \frac{M_{O_2}}{2M_{CO_2}} Y_{CO_2} \quad (14)$$

$$Y_{CO} = \frac{M_{CO}}{M_C} + \left(\frac{M_{CO}}{M_{CO_2}} Y_{CO_{2b}} - \frac{M_{CO}}{M_C}\right)\left(\frac{r}{r_b}\right)^{\gamma} - \frac{M_{CO}}{M_{CO_2}} Y_{CO_2} \quad (15)$$

$$-2\beta\tau + Y_{CO_2} = \left[2\beta(\tau_S - 1) + \epsilon + Y_{CO_{2b}}\right]\left(\frac{r}{r_b}\right)^{\gamma} - 2\beta\tau_S - \epsilon \quad (16)$$

where

$$\gamma = \frac{\dot{m}}{\rho D} \qquad \beta = \frac{M_{CO_2} C_p T_b}{H_{CO}} \qquad \epsilon = \frac{M_{CO_2} H_{O_2}}{M_C H_{CO}}$$

If one of the variables Y_{O_2}, Y_{CO_2}, Y_{CO}, or τ is known, the other variables can be determined using equations (14), (15), and (16). In this case, the surface temperature was considered known, and the surface mass fractions $Y_{O_{2S}}$, $Y_{CO_{2S}}$, and Y_{CO_S} were determined. The gas phase reaction between carbon monoxide and oxygen was assumed to be first order with respect to both carbon monoxide and oxygen.

$$\mathscr{R}_{CO} = k_g C_{CO} C_{O_2} \exp(-E/RT) \tag{17}$$

where k_g = pre-exponential factor for the gas phase reaction, $CO + 1/2\ O_2 \rightarrow CO_2$;

C_{CO} = molar concentration of carbon monoxide;

C_{O_2} = molar concentration of oxygen;

E = activation energy for the gas phase reaction, $CO + 1/2\ O_2 \rightarrow CO_2$; and

R = universal gas constant.

This equation was substituted into equation (4) yielding

$$\frac{\dot{m}}{r}\frac{dY_{CO}}{dr} - \frac{\rho D_{CO}}{r}\frac{d}{dr}\left(r\frac{dY_{CO}}{dr}\right) = -M_{CO}k_g C_{CO} C_{O_2} \exp(-E/RT) \tag{18}$$

Equation (18) was solved using a Runge-Kutta technique. The solution of equation (18) along with equations (14), (15), and (16) yield-

ed carbon monoxide, carbon dioxide, and oxygen concentration profiles, and the temperature profile. To compare the results from the model with the normal gravity data, the mass fractions were converted to mole fractions using the equation

$$X_i = \frac{(Y_i/M_i)}{(Y_i/M_i) + (Y_j/M_j) + (Y_k/M_k)} \qquad (19)$$

where i represents oxygen, carbon dioxide, or carbon monoxide, and j and k represents the other two species.

The physical properties used in the equations are presented in Table 6. The binary diffusion coefficients used were obtained by averaging the coefficients obtained from the Stefan-Maxwell equations for an ideal gas. The activation energy for the gas phase reaction of carbon monoxide with oxygen was taken as 43800 cal/g mole [40]. The rate constants for the surface reactions, that is, for carbon with oxygen and carbon with carbon dioxide, were taken from Reference [41] and are listed in Table 7. Only the reaction rate constants that allowed physically reasonable solutions, that is, surface mass fractions equal to or greater than zero and less than or equal to one using equations (14), (15), and (16) are listed.

In the solution of the equations using the Runge-Kutta technique, the pre-exponential factor, k_g, for the gas phase reaction was varied so that the boundary conditions at the outer edge of the stagnant film were met. These were initially taken to be $Y_{O_{2b}} = 1$, $Y_{CO_{2b}} = 0$, and $\tau = 1$. The thickness of the stagnant film was varied from 0.302 cm (0.119 in.) to 0.759 cm (0.299 in.) to account for

Table 6. - Physical properties

ρ	$= 4.982 \times 10^{-4}$ g/cm^3
c_p	$= 0.273$ cal/g $^\circ$K
D	$= 1.23$ cm^2/sec
T_b	$= 294.44$ $^\circ$K
H_{CO}	$= 1.348 \times 10^5$ cal/g mole
H_{O_2}	$= 2.677 \times 10^4$ cal/g mole
H_{CO_2}	$= 4.063 \times 10^4$ cal/g mole
T_s	$= 1542$ $^\circ$K

Table 7. - Surface reaction rate constants

$$k_{O_2} = 1.1 \times 10^3 \exp(-25500/RT) \quad cm/sec \qquad 7\text{-}1$$

$$k_{O_2} = 1.0 \times 10^3 \exp(-20300/RT) \quad cm/sec \qquad 7\text{-}2$$

$$k_{CO_2} = 6.9 \times 10^6 \exp(-44250/RT) \quad cm/sec \qquad 7\text{-}3$$

$$k_{CO_2} = 1.6 \times 10^9 \exp(-52000/RT) \quad cm/sec \qquad 7\text{-}4$$

$$k_{CO_2} = 3.0 \times 10^6 \exp(-40400/RT) \quad cm/sec \qquad 7\text{-}5$$

$$k_{CO_2} = 3.16 \times 10^{10} \exp(-74000/RT) \quad cm/sec \qquad 7\text{-}6$$

$$k_{CO_2} = 7.9 \times 10^7 \exp(-51200/RT) \quad cm/sec \qquad 7\text{-}7$$

the increase in the free convective boundary layer around the circumference of the horizontal carbon rod. The stagnant film thickness and surface reaction rate constants used in the solution of the model equations, along with the resulting surface mole and mass fractions of oxygen, carbon dioxide, and carbon monoxide, the derivative of the mass fraction of CO at the surface, and the pre-exponential factor for the gas phase reaction are presented in Table 8. The computed mole fractions were compared to the normal gravity experimental data obtained at the 90^{o} and 45^{o} probe positions. The 0^{o} probe position data was not used for comparison, since it was not possible to obtain concentrations close to the surface at that probe position.

B. Comparison of Model with Normal Gravity Experimental Data

The cases where the model compared best with the normal gravity experimental data are presented in Figures 57 to 60. In Figures 57 and 58, the experimental data taken at the 90^{o} and 45^{o} probe positions, respectively, are compared to the mole fractions calculated using a stagnant layer thickness of 0.404 cm (0.159 in.). In Figure 57, it can be seen that the model does predict the mole fraction behavior of CO fairly well for the 90^{o} probe position, especially at distances greater than 0.071 cm (0.028 in.) from the surface. The model over predicts the mole fractions of O_2 and under predicts the mole fractions of CO_2. For the 45^{o} probe position, shown in Figure 58, the calculated mole fractions of CO are higher than the experimentally obtained mole fractions at distances less than 0.076 cm (0.03 in.) from the surface, and are lower than the experimental mole

Table 8. - Model parameters and results

δ cm	δ in.	$k^*_{O_2}$	$k^*_{CO_2}$	$Y_{O_{2s}}$	$Y_{CO_{2s}}$	Y_{CO_s}	$X_{O_{2s}}$	$X_{CO_{2s}}$	X_{CO_s}	a^1CO/dr 1/cm	a^1CO/dr (1/in)	γ	ξ_s cm^3/g mole sec
0.302	(0.119)	7-1	7-3	0.8095	0.1635	0.0210	0.8461	0.1288	0.0251	-0.943	(-2.394)	0.083	3.69×10^{14}
0.302	(0.119)	7-1	7-4	0.871	0.055	0.374	0.550	0.039	0.412	-3.711	(-9.426)	0.282	1.02×10^{12}
0.302	(0.119)	7-1	7-5	0.787	0.159	0.054	0.816	0.120	0.064	-1.200	(-3.049)	0.100	1.06×10^{14}
0.302	(0.119)	7-2	7-6	0.690	0.112	0.198	0.692	0.080	0.227	-1.301	(-3.304)	0.179	1.82×10^{11}
0.302	(0.119)	7-2	7-7	0.6693	0.1025	0.2283	0.6662	0.0742	0.2596	-1.573	(-3.995)	0.1964	1.80×10^{11}
0.353	(0.139)	7-1	7-3	0.799	0.165	0.036	0.832	0.125	0.043	-0.918	(-2.331)	0.081	1.39×10^{14}
0.353	(0.139)	7-1	7-4	0.5604	0.0505	0.3892	0.5379	0.0352	0.4268	-3.406	(-8.652)	0.2605	6.43×10^{11}
0.353	(0.139)	7-1	7-5	0.7763	0.1536	0.0701	0.8019	0.1154	0.0827	-1.161	(-2.949)	0.0976	5.60×10^{13}
0.353	(0.139)	7-2	7-6	0.671	0.104	0.225	0.669	0.075	0.256	-1.244	(-1.161)	0.174	1.22×10^{13}
0.353	(0.139)	7-2	7-7	0.651	0.094	0.255	0.644	0.068	0.288	-1.507	(-3.899)	0.190	1.19×10^{13}
0.404	(0.159)	7-1	7-3	0.7906	0.1605	0.0489	0.8208	0.1212	0.0580	-0.894	(-2.271)	0.0798	7.04×10^{13}
0.404	(0.159)	7-1	7-4	0.5527	0.0468	0.4005	0.5293	0.0326	0.4381	-3.158	(-8.022)	0.2431	4.44×10^{11}
0.404	(0.159)	7-1	7-5	0.766	0.149	0.085	0.789	0.112	0.100	-1.126	(-2.860)	0.095	3.38×10^{13}
0.404	(0.159)	7-2	7-6	0.656	0.096	0.248	0.650	0.069	0.281	-1.191	(-3.026)	0.169	3.28×10^{12}
0.404	(0.159)	7-2	7-7	0.6360	0.0865	0.2776	0.6260	0.0619	0.3121	-1.419	(-3.604)	0.1834	9.47×10^{12}
0.455	(0.179)	7-1	7-3	0.782	0.157	0.061	0.810	0.118	0.072	-0.875	(-2.222)	0.079	4.12×10^{13}
0.455	(0.179)	7-1	7-4	0.5463	0.0438	0.4100	0.5220	0.0304	0.4476	-2.972	(-7.549)	0.2290	3.13×10^{11}
0.455	(0.179)	7-1	7-5	0.758	0.145	0.097	0.778	0.108	0.114	-1.097	(-2.786)	0.093	2.58×10^{13}
0.455	(0.179)	7-2	7-6	0.6420	0.0894	0.2686	0.6312	0.0641	0.3027	-1.157	(-2.940)	0.1656	6.50×10^{12}
0.455	(0.179)	7-2	7-7	0.623	0.080	0.297	0.610	0.057	0.332	-1.359	(-3.452)	0.178	7.41×10^{12}
0.503	(0.198)	7-1	7-3	0.776	0.154	0.070	0.802	0.116	0.083	-0.859	(-2.182)	0.077	3.25×10^{13}
0.503	(0.198)	7-1	7-4	0.5428	0.0419	0.4154	0.5180	0.0291	0.4529	-2.836	(-7.204)	0.2168	2.27×10^{11}
0.503	(0.198)	7-1	7-5	0.751	0.142	0.107	0.769	0.106	0.125	-1.074	(-2.729)	0.092	1.48×10^{13}
0.503	(0.198)	7-2	7-6	0.630	0.084	0.286	0.619	0.060	0.321	-1.127	(-2.863)	0.162	4.37×10^{12}
0.503	(0.198)	7-2	7-7	0.611	0.075	0.314	0.597	0.053	0.350	-1.108	(-3.323)	0.174	5.74×10^{12}

$\delta = r_b - r_s$

k^* surface reaction rate constant listed in Table 7

Table 8.- Concluded

δ cm (in)		$k^*_{O_2}$	$k^*_{CO_2}$	$Y_{O_{2S}}$	$Y_{CO_{2S}}$	Y_{CO_S}	$X_{O_{2e}}$	$X_{CO_{2e}}$	X_{CO_e}	dY_{CO}/dr 1/cm	(1/in)	V	E_g cm^3/g mole sec
0.556	(0.219)	7-1	7-3	0.769	0.150	0.081	0.792	0.112	0.095	-0.839	(-2.131)	0.076	2.43×10^{13}
0.556	(0.219)	7-1	7-4	0.537	0.039	0.424	0.512	0.027	0.461	-2.646	(-6.722)	0.2069	1.96×10^{11}
0.556	(0.219)	7-1	7-5	0.743	0.138	0.199	0.694	0.094	0.212	-1.045	(-2.654)	0.090	1.37×10^{13}
0.556	(0.219)	7-2	7-6	0.618	0.078	0.303	0.605	0.056	0.339	-1.088	(-2.764)	0.159	3.97×10^{12}
0.556	(0.219)	7-2	7-7	0.6002	0.0694	0.3305	0.5837	0.0494	0.3672	-1.258	(-3.196)	0.1695	4.88×10^{12}
0.607	(0.239)	7-1	7-3	0.763	0.147	0.090	0.784	0.110	0.106	-0.823	(-2.091)	0.075	1.91×10^{12}
0.607	(0.239)	7-1	7-4	0.5328	0.0373	0.4300	0.5069	0.0258	0.4673	-2.527	(-6.419)	0.1984	1.57×10^{11}
0.607	(0.239)	7-1	7-5	0.736	0.135	0.129	0.750	0.100	0.150	-1.022	(-2.597)	0.089	1.03×10^{13}
0.607	(0.239)	7-2	7-6	0.609	0.073	0.318	0.594	0.052	0.354	-1.061	(-2.696)	0.156	3.45×10^{12}
0.607	(0.239)	7-2	7-7	0.591	0.065	0.345	0.572	0.046	0.382	-1.217	(-3.092)	0.166	4.12×10^{12}
0.658	(0.259)	7-1	7-3	0.757	0.145	0.098	0.777	0.108	0.115	-0.812	(-2.062)	0.074	1.56×10^{13}
0.658	(0.259)	7-1	7-4	0.5294	0.0357	0.4350	0.5031	0.0247	0.4723	-2.422	(-6.151)	0.1909	1.30×10^{11}
0.658	(0.259)	7-1	7-5	0.731	0.132	0.137	0.743	0.098	0.159	-1.002	(-2.545)	0.087	9.25×10^{12}
0.658	(0.259)	7-2	7-6	0.598	0.069	0.333	0.581	0.049	0.370	-1.031	(-2.619)	0.154	2.75×10^{12}
0.658	(0.259)	7-2	7-7	0.582	0.061	0.357	0.563	0.043	0.394	-1.180	(-2.996)	0.163	3.14×10^{12}
0.709	(0.279)	7-1	7-3	0.753	0.142	0.105	0.771	0.106	0.123	-0.798	(-2.026)	0.073	1.29×10^{13}
0.709	(0.279)	7-1	7-4	0.5263	0.0343	0.4395	0.4996	0.0237	0.4767	-2.330	(-5.917)	0.1843	1.03×10^{11}
0.709	(0.279)	7-1	7-5	0.726	0.129	0.145	0.737	0.095	0.168	-0.981	(-2.491)	0.086	7.37×10^{12}
0.709	(0.279)	7-2	7-6	0.591	0.065	0.344	0.573	0.046	0.381	-1.012	(-2.570)	0.151	2.51×10^{12}
0.709	(0.279)	7-2	7-7	0.575	0.057	0.368	0.555	0.040	0.405	-1.147	(-2.914)	0.159	3.29×10^{12}
0.759	(0.299)	7-1	7-3	0.748	0.140	0.112	0.765	0.104	0.131	-0.787	(-1.998)	0.073	9.00×10^{12}
0.759	(0.299)	7-1	7-4	0.524	0.033	0.443	0.497	0.023	0.480	-2.244	(-5.701)	0.178	7.95×10^{10}
0.759	(0.299)	7-1	7-5	0.720	0.127	0.153	0.729	0.094	0.177	-0.965	(-2.452)	0.085	6.29×10^{12}
0.759	(0.299)	7-2	7-6	0.583	0.061	0.356	0.564	0.043	0.393	-0.989	(-2.512)	0.149	2.13×10^{12}
0.759	(0.299)	7-2	7-7	0.5674	0.0537	0.379	0.5459	0.0376	0.4166	-1.115	(-2.833)	0.1567	2.67×10^{12}

$k_{O_2} = 1.1 \times 10^3 \exp(-25500/RT)$ cm/sec
$k_{CO_2} = 1.6 \times 10^9 \exp(-52000/RT)$ cm/sec
$E = 43800$ cal/g mole
$k_g = 4.44 \times 10^{11}$ cm^3/g mole sec
$X_{O_{2S}} = 0.5293$ $X_{O_{2b}} = 1.0$
$X_{CO_{2S}} = 0.0326$ $X_{CO_{2b}} = 0$
$X_{CO} = 0.4381$ $T_S = 1542$ K

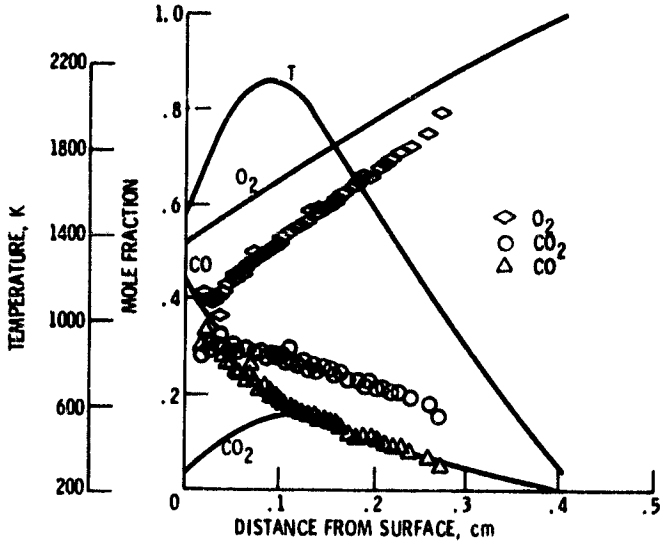

Figure 57. - Comparison of model with experimental data - 0.404 cm (0.159 in.) stagnant film thickness - probe position 90°.

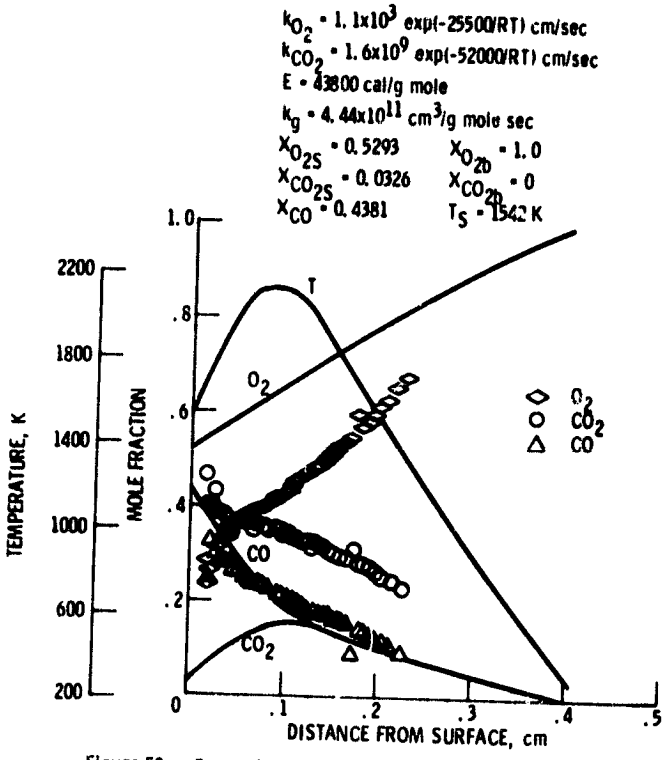

Figure 58. - Comparison of model with experimental data - 0.404 cm (0.159 in.) stagnant film thickness - probe position 45°.

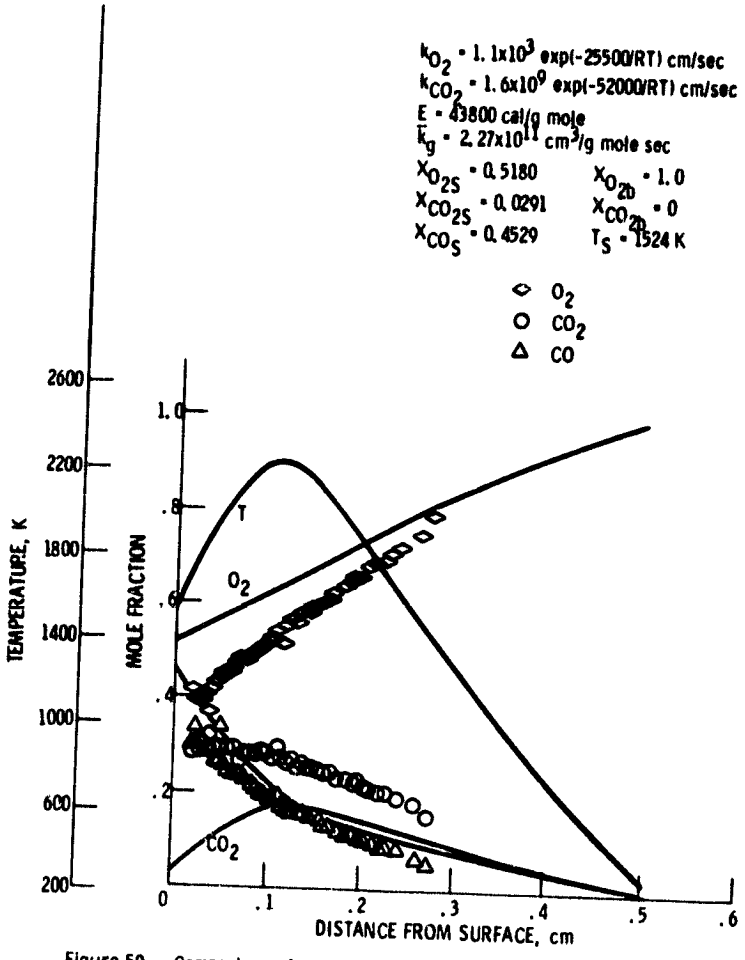

Figure 59. - Comparison of model with experimental data - 0.503 cm (0.198 in.) stagnant film thickness - probe position 90°.

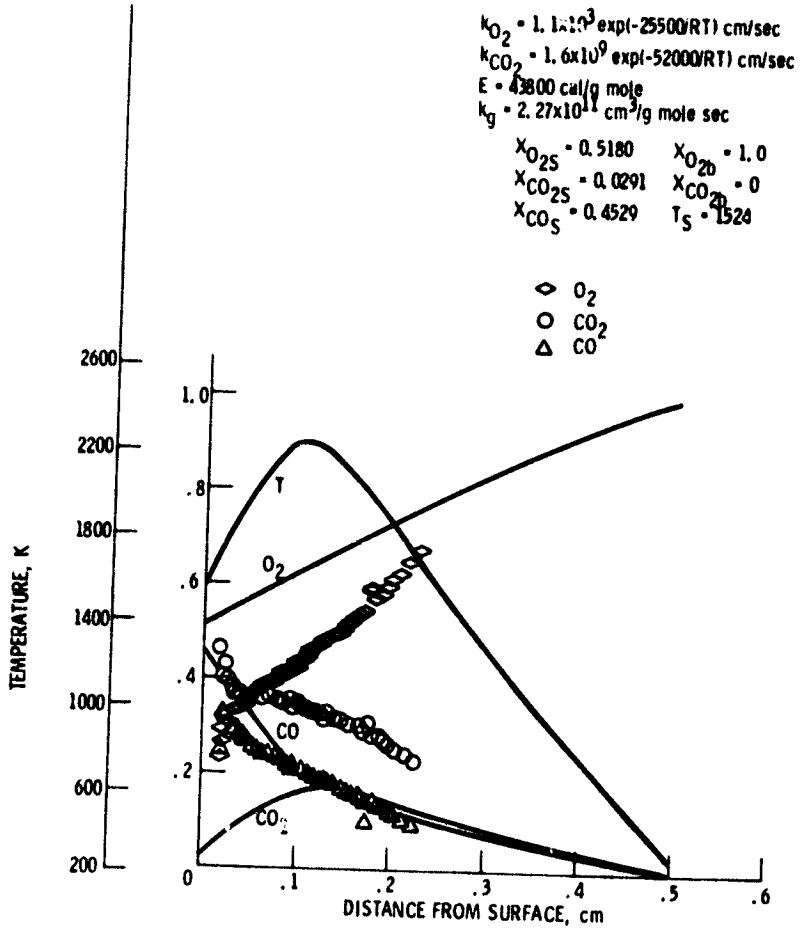

Figure 60. - Comparison of model with experimental data - 0.503 cm (0.198 in.) stagnant film thickness - probe position 45°.

fractions at greater distances. Again, the model over predicts the mole fractions of O_2 and under predicts the mole fractions of CO_2.

In Figures 59 and 60, the experimental data taken at the 90^o and 45^o probe positions are compared to the mole fractions calculated using a larger stagnant layer thickness of 0.503 cm (0.198 in.). Figure 59 shows that at the the 90^o probe position, the model predicts CO mole fractions slightly higher than those obtained experimentally. At the 45^o probe position, shown in Figure 60, the model predicts higher CO mole fractions than obtained experimentally at distances less than 0.107 cm (0.042 in.) from the surface, between distances of 0.107 cm (0.042 in.) and 0.203 cm (0.080 in.), there is good agreement in the mole fractions, and at distances greater than 0.203 cm (0.080 in.) the model predicts slightly higher CO mole fractions. At both probe positions the model over-predicts the O_2 mole fractions and under-predicts the CO_2 mole fractions.

In an attempt to obtain better agreement between the experimental data and the model, the mole fractions of O_2 and CO_2 at the outer edge of the stagnant film were changed to 0.925 and 0.075, respectively. The values were reasonable because of the design of the burning apparatus, which could have caused some recirculation of the combustion gases and thereby increased the mole fraction of CO_2 in the ambient atmosphere. In the solution of the equations only the surface reaction rate constants $k_{O_2} = 1.1 \times 10^3$ cm/sec exp [-25500/RT] and $k_{CO_2} = 1.6 \times 10^9$ cm/sec exp [-52000/RT] were used because these gave the closest agreement for the case of an oxygen mole fraction of 1.0 at the outer edge of the stagnant film. The thickness of the stagnant film was again varied from 0.302 cm (0.119 in.) to 0.709

cm (0.279 in.). The stagnant film thickness and the surface reaction rate constants used in the solution of the model equations, along with the resulting surface mole and mass fractions of oxygen, carbon dioxide, and carbon monoxide, the derivative of the mass fraction of CO at the surface, and the pre-exponential factor for the gas phase reaction are presented in Table 9. The cases where the model and the experimental data compare the best are presented in Figures 61 to 64.

In Figures 61 and 62, the experimental data taken at the 90^{o} and 45^{o} probe positions are compared to the mole fractions calculated using a stagnant layer thickness of 0.353 cm (0.139 in.). Figure 61 shows that at the 90^{o} probe position, the calculated mole fractions of CO and CO_2 and the experimental data are in good agreement at distances greater than 0.117 cm (0.046 in.) from the surface. The calculated and experimentally obtained O_2 mole fractions are in fair agreement over the whole distance experimental data was taken. At the 45^{o} probe position, shown in Figure 62, the model predicts O_2 mole fractions that are higher and CO and CO_2 mole fractions that are lower than the experimentally obained mole fractions.

In Figures 63 and 64, the data obtained at the 90^{o} and 45^{o} probe positions are compared to the mole fractions calculated using a stagnant layer thickness of 0.429 cm (0.169 in.). For the 90^{o} probe position, shown in Figure 63, the model predicts O_2 mole fractions that are lower and CO and CO_2 mole fractions that are higher than the experimentally obtained mole fractions. Figure 64 shows that at the 45^{o} probe position, the calculated O_2 mole fractions are in good agreement with the experimentally obtained data at distances greater than approximately 0.051 cm (0.02 in.) from the surface. The

Table 9. - Model parameters and results

δ cm	δ (in.)	$k^*_{O_2}$	$k^*_{CO_2}$	$Y_{O_{2s}}$	$Y_{CO_{2s}}$	Y_{CO_b}	$X_{O_{2s}}$	$X_{CO_{2s}}$	X_{CO_s}	dY_{CO}/dr 1/cm	dY_{CO}/dr (1/in.)	β	E_a cm^3/g mole sec
0.302	(0.119)	7-1	7-4	0.3837	0.0793	0.5370	0.3637	0.0547	0.5816	-5.008	(-12.721)	0.3838	1.80×10^{11}
0.353	(0.139)	7-1	7-4	0.372	0.073	0.555	0.351	0.050	0.599	-4.595	(-11.672)	0.354	1.15×10^{11}
0.404	(0.159)	7-1	7-4	0.362	0.068	0.570	0.341	0.047	0.613	-4.268	(-10.841)	0.331	7.90×10^{10}
0.429	(0.169)	7-1	7-4	0.3585	0.0658	0.5748	0.3379	0.0450	0.6179	-4.129	(-10.488)	0.320	6.745×10^{10}
0.455	(0.179)	7-1	7-4	0.3557	0.0638	0.5805	0.3339	0.0435	0.6226	-3.996	(-10.149)	0.3109	5.85×10^{10}
0.503	(0.198)	7-1	7-4	0.3497	0.0604	0.5900	0.3275	0.0411	0.6313	-3.780	(-9.600)	0.2956	4.54×10^{10}
0.505	(0.199)	7-1	7-4	0.3496	0.0604	0.5900	0.3275	0.0411	0.6314	-3.781	(-9.604)	0.2947	4.42×10^{10}
0.556	(0.219)	7-1	7-4	0.3442	0.0574	0.5984	0.3218	0.0390	0.6392	-3.588	(-9.114)	0.2811	3.47×10^{10}
0.607	(0.239)	7-1	7-4	0.3396	0.0548	0.6056	0.3170	0.0372	0.6458	-3.422	(-8.691)	0.2698	2.89×10^{10}
0.658	(0.259)	7-1	7-4	0.3357	0.0562	0.6117	0.3122	0.0380	0.6498	-3.282	(-8.336)	0.2591	2.36×10^{10}
0.709	(0.279)	7-1	7-4	0.3224	0.0508	0.6168	0.3030	0.0347	0.6623	-3.169	(-8.050)	0.2499	1.93×10^{10}

$\delta = r_b - r_s$

k^* surface reaction rate constants listed in Table 7

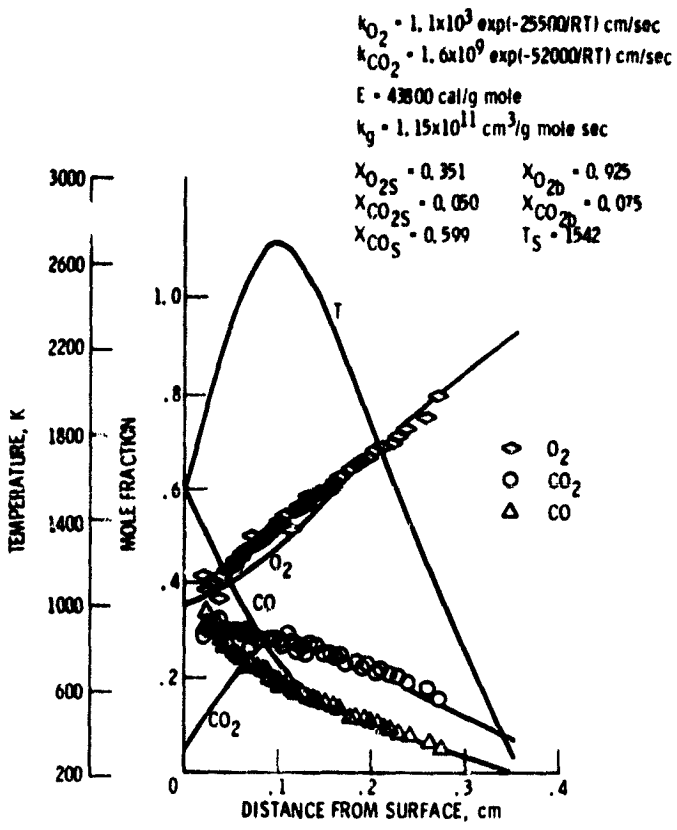

Figure 61. - Comparison of model with experimental data - 0.353 cm (0.139 in.) stagnant film thickness - probe position 90°.

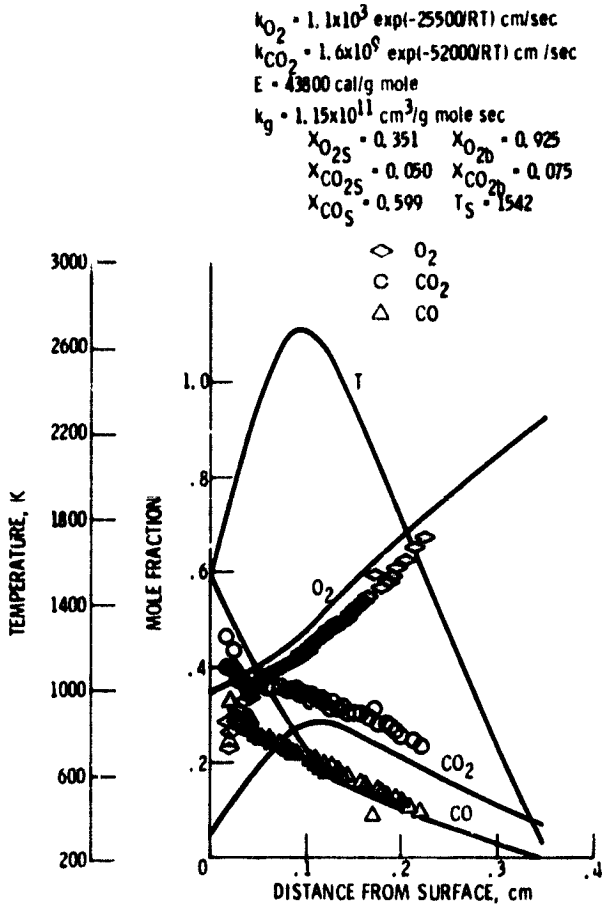

Figure 62. - Comparison of model with experimental data - 0.353 cm (0.139 in.) stagnant film thickness - probe position 45°.

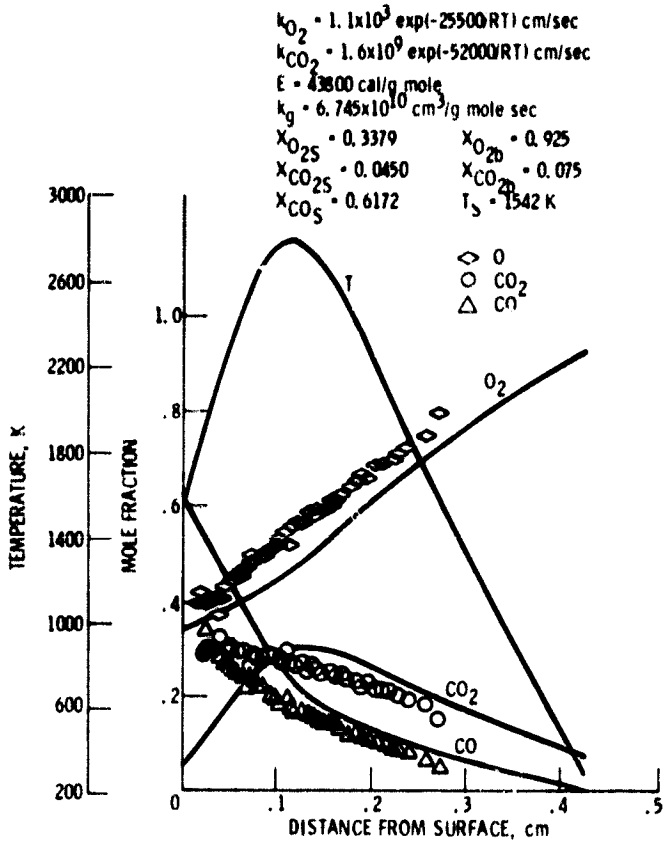

Figure 63. - Comparison of model with experimental data - 0.429 cm (0.169 in.) stagnant film thickness - probe position 90°.

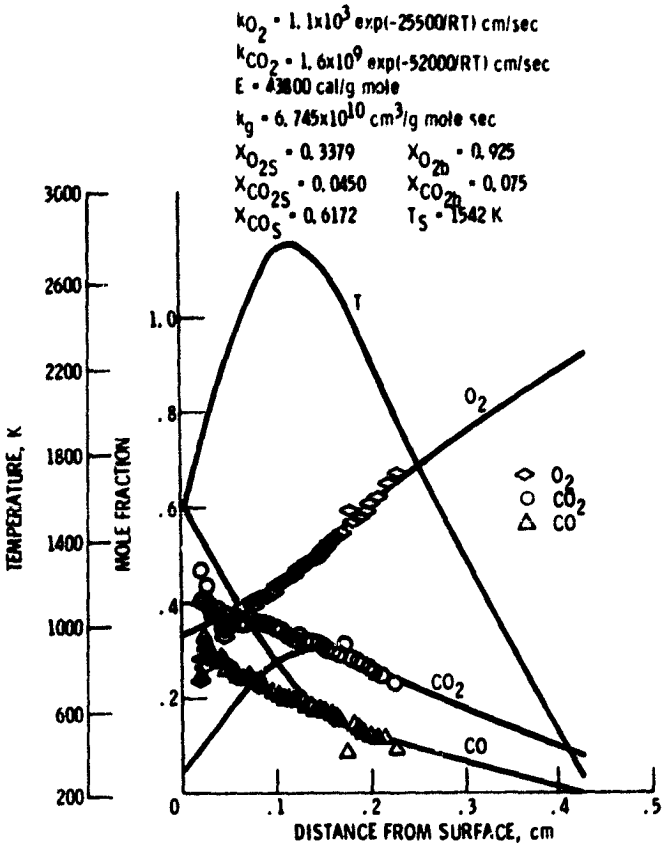

Figure 64. - Comparison of model with experimental data - 0.429 cm (0.169 in.) stagnant film thickness - probe position 45°.

calculated mole fractions of CO and CO_2 are in good agreement with the experimental data for distances greater than approximately 0.140 cm (0.055 in.) from the surface.

It is consistent with the boundary layer concept that the boundary layer thickness should increase from the 90^o to the 45^o probe positions. This fact is reflected in Figures 61 and 64, which show that the 90^o data is best fit with a film thickness of 0.353 cm, while the 45^o data is best fit with a film thickness of 0.429 cm.

To summarize the model comparison with the experimental data, the model with an O_2 mole fraction equal to 1 at the outer edge of the stagnant layer predicted the mole fractions of CO over the distance from the surface better than the model with mole fractions of O_2 equal to 0.925 and CO_2 equal to 0.075 at the outer edge of the stagnant film. However, it did not accurately predict the mole fractions of CO_2 and O_2. The model with mole fractions of O_2 equal to 0.925 and CO_2 equal to 0.075 predicted the mole fractions of O_2 reasonably well over the distance from the surface where data was taken. Also, it predicted the CO_2 and CO mole fractions at distances greater than approximately 0.129 cm (0.051 in.) from the surface. Using either outer edge boundary condition, the model was unable to predict the experimentally obtained CO_2 mole fractions at distances less than approximately 0.1 cm (0.039 in.) from the surface. This is most probably due to free convective effects, which caused the combustion products to rise. The experimental data taken at the 90^o and 45^o probe positions show that the largest difference in both the O_2 and CO_2 mole fractions occurs near the surface and decreases with distance from the surface. This means free convec-

tion mass and heat transfer effects would be greatest near the surface and would decrease with distance from the surface. The stagnant layer thickness was varied in the model in order to somewhat account for the convective effects, and did improve the model agreement with the data. The model thus qualitatively describes the carbon rod combustion process, and should either be compared with zero-gravity combustion data or modified to more fully include convective effects.

VI. CONCLUSIONS AND RECOMMENDATIONS

Experiments were conducted in zero and normal gravity in which horizontally mounted spectroscopic carbon rods were burned in dry oxygen environments.

In the zero gravity experiments 0.615 cm (0.242 in.), 0.457 cm (0.180 in.), and 0.305 cm (0.120 in.) diameter carbon rods were burned in oxygen at pressures of 3.45×10^4 N/M^2 (5 psia), 6.89×10^4 N/M^2 (10 psia), 1.03×10^5 N/M^2 (15 psia), and 1.38×10^5 N/M^2 (20 psia). The oxygen had a maximum water vapor content of 0.5 ppm. The photographs of the zero-gravity combustion process showed that in all the cases where sustained burning occurred, a blue flame extending from the surface surrounded the rod. This means that a gas phase reaction was taking place in which carbon monoxide was being oxidized to carbon dioxide. Mathematical models describing the carbon combustion process which account for a gas phase reaction are those of Hugo, Wicke, and Wurzbacher [4] and Caram and Amundson [6]. It was not possible to test these models since concentration profiles and surface temperature measurements could not be obtained in the zero gravity tests. From the zero gravity data, it was found that the ratio of flame diameter to rod diameter, d*, increased as the pressure decreased, and decreased as the rod diameter increased. The data was used to obtain the correlation equation:

$$\hat{d}^* = \alpha(1 - e^{-\phi_1 t - \phi_2})$$

where $\alpha = 1.943 - 6.599(d - 0.18) - 0.03517\,(P - 12.5) + 46.69(d - 0.18)^2$

$\phi_1 = 0.687$

$\phi_2 = 1.015 + 4.335(d - 0.18) + 0.0278(P - 12.5) - 119.4(d - 0.18)^2$

and d (rod diameter) is in inches, P (pressure) is in psia, and t (time) is in seconds. The zero gravity data obtained in this study can be used to properly design a long duration Spacelab experiment on carbon combustion, in which complete information on concentrations and temperatures can be obtained.

In the normal gravity experiments, 0.615 cm (0.242 in.) diameter carbon rods were burned in oxygen at atmospheric pressure. The oxygen had a moisture content of less than 6 ppm. A concentration sampling probe was positioned near the circumference of the rod at either the top or at angles of 45^0 or 90^0 from the top, and yielded concentration profiles of CO_2, CO, and O_2 as a function of distance from the surface. At all the sampling probe positions, the O_2 concentration increased with distance from the surface, while the CO concentration decreased with distance. At the 90^0 position the CO_2 concentration first increased slightly with distance from the surface and then decreased, whereas at the 45^0 probe position, it decreased with distance from the surface. At the 0^0 probe postion, the CO_2 concentration increased to a maximum away from the surface, and then

decreased. Moving from the 90^0 probe position to the top probe position, the O_2 concentration in the gas surrounding the rod decreased, the CO_2 concentration increased, but is expected to be lowest near the surface at the top of the rod, and the CO concentration in general increased. This meant that convective effects were playing a considerable role in the combustion process, decreasing the oxygen supply to the rod by convecting up the combustion products. The data also indicates that the surface reactions at 90^0 and 45^0 from the top of the rod were controlled by the chemical process, while the surface reaction at the top of the rod may have been controlled by mass transfer. The data shows that there was a gas phase reaction in which CO was burned to CO_2, as was the case in the zero-gravity experiments. The time averaged surface temperature of the rod was found to be 1269° C, which is above the minimum temperature found in the literature for a gas phase reaction to occur.

The carbon dioxide mole fraction increasing with distance from the surface and then decreasing at the 90^0 and 0^0 probe positions means that CO_2 was being reduced to CO at the surface. This reduction reaction was probably occurring at the 45^0 probe position also, but was masked by free convective effects which caused the combustion products, especially CO_2, to rise. The CO_2 reduction reaction occurring in these experiments with a carbon surface temperature of 1269° C is in agreement with the finding of other investigators, who determined the minimum temperaure at which this reaction would occur to be 1100^0C.

Good qualitative agreement between the carbon combustion data obtained in the present investigation at the 90^0 and 45^0 probe posi-

tions and that obtained experimentally by Wicke and Wurzbacher [5] indicates that the same physical phenomena was being observed in both studies. This conclusion is justified by quantitative agreement of the data at the 0^{o} probe position, where convective effects were of similar importance in both studies.

The normal gravity experimental data were also compared to the stagnant film mathematical model proposed by Caram and Amundson [6]. The model, with ambient mole fractions of O_2 equal to 0.925 and CO_2 equal to 0.075, predicted the mole fractions of O_2 reasonably well over the complete distance from the rod surface, and the mole fractions of CO_2 and CO at distances greater than approximately 0.129 cm (0.051 in.) from the surface. The stagnant film thickness was varied in the model in order to somewhat account for the convective effects, and did improve the model agreement with the data. The model thus qualitatively describes the carbon rod combustion process, and should either be compared with more complete zero-gravity data or modified to more fully include convective effects.

It is therefore concluded, in agreement with other investigators, that carbon combustion is complex. Under the experimental conditions used in the present study, the combustion process was characterized by two surface reactions, $2C + O_2 \rightarrow 2CO$ and $C + CO_2 \rightarrow 2CO$, and a gas phase reaction, $CO + 1/2\ O_2 \rightarrow CO_2$. The process controlling step changed from chemical process control to mass transfer control as probe measurements went from 90^{o} to 0^{o} in the normal gravity experiments. In both zero and normal gravity, the carbon combustion is best described mathematically by the model of Caram and Amundson [6], although modification for convective effects is needed.

To learn more about the role of convection as it affects the mechanisms of carbon combustion, a long-term zero gravity experiment is needed. This would eliminate the strong normal gravity convective effects and allow for long term gas sampling and temperature measurements. The obtained surface temperature, concentration profiles, and temperature profiles would completely describe the zero-gravity combustion process and confirm the zero-gravity combustion model. By comparing normal gravity and zero-gravity data, the extent that free convection affects the O_2, CO_2, and CO concentrations can be determined. This information can be used to obtain a correction factor for the stagnant film model so that it could predict the concentration profiles when convection is present. Also, the zero-gravity data can be used to obtain information concerning the relationship between mass transfer and chemical process control. Additional supplementary experimental work is needed to obtain accurate reaction rate constants for the carbon-oxygen and carbon-carbon dioxide surface reactions and for the oxygen-carbon monoxide gas phase reaction.

APPENDIX

MATHEMATICAL MODEL DERIVATION

The model presented by Caram and Amundson [6] was extended to a cylindrical rod. The following assumptions were used: (1) a stagnant film of thickness δ surrounds the carbon rod; (2) axial end effects are neglected; (3) the rod does not react internally and is impervious to mass transfer; (4) the species present are CO, CO_2, and O_2; (5) gas properties are constant; (6) the Schwab-Zeldovich approximation (that is, the diffusion coefficients are the same and equal to $(\lambda/\rho c_p)$) holds; (7) the process is at steady state; (8) effective binary diffusion; (9) the flow is only in the radial direction; and (10) there are two surface reactions, $2C + O_2 \rightarrow 2CO$, and $C + CO_2 \rightarrow 2CO$, and a gas phase reaction, $CO + 1/2\ O_2 \rightarrow CO_2$.

A. Governing Equations

The equations governing this combustion process are the Species Continuity Equations:

$$\frac{\partial \rho_i}{\partial t} + \frac{1}{r}\frac{\partial}{\partial r}(rn_{ir}) = R_i \qquad i = O_2, CO_2, CO \tag{A1}$$

where

$$n_{ir} = -\sum_{j=1}^{2} D_{ij} \frac{\partial \rho_i}{\partial r} + \rho_i v \qquad \text{(A2)}$$

and the Thermal Energy Equation:

$$\rho c_p \left(\frac{\partial T}{\partial t} + v \frac{\partial T}{\partial r}\right) = \frac{1}{r} \frac{\partial}{\partial r} \left(\lambda r \frac{\partial T}{\partial r}\right) + q' \qquad \text{(A3)}$$

where ρ_i = mass concentration of species i;

t = time;

r = radial distance from the center of the rod;

n_{ir} = mass flux of species i in the radial direction;

R_i = gas phase mass reaction rate of species i;

D_{ij} = effective binary diffusivity;

v = radial velocity;

ρ = density of mixture;

c_p = specific heat of mixture;

T = temperature;

λ = thermal conductivity of the mixture;

$q' = \frac{H_{CO} \mathscr{R}_{CO}}{2}$ = the heat generated by the combustion of carbon monoxide;

H_{CO} = heat of combustion of two moles of carbon monoxide; and

$\mathscr{R}_{CO}$ = gas phase molar reaction rate of carbon monoxide.

By using the assumptions of steady state, constant physical properties, and binary diffusion, and combining equations (A1) and (A2), the Species Continuity and Thermal Energy Equations become

$$\frac{1}{r}\frac{d}{dr}(\rho r v Y_i) - \frac{\rho D_i}{r}\frac{d}{dr}\left(r\frac{dY_i}{dr}\right) = R_i \tag{A4}$$

$$\rho c_p v \frac{dT}{dr} = \frac{\lambda}{r}\frac{d}{dr}\left(r\frac{dT}{dr}\right) + q' \tag{A5}$$

where Y_i = mass fraction of species i; and

D_i = effective binary diffusivity.

At steady state conservation of mass for the mixture yields $(d/dr)(r\rho v) = 0$. Therefore $\rho r v = \text{constant} = \dot{m}$ is the carbon burning rate.

Using equation (A4) and the fact that $\rho r v = \dot{m}$ is a constant, the individual Species Continuity Equations can be written as

$$\frac{\dot{m}}{r}\frac{dY_{O_2}}{dr} - \frac{\rho D_{O_2}}{r}\frac{d}{dr}\left(r\frac{dY_{O_2}}{dr}\right) = -R_{O_2} \tag{A6}$$

$$\frac{\dot{m}}{r}\frac{dY_{CO_2}}{dr} - \frac{\rho D_{CO_2}}{r}\frac{d}{dr}\left(r\frac{dY_{CO_2}}{dr}\right) = R_{CO_2} \tag{A7}$$

$$\frac{\dot{m}}{r}\frac{dY_{CO}}{dr} - \frac{\rho D_{CO}}{r}\frac{d}{dr}\left(r\frac{dY_{CO}}{dr}\right) = -R_{CO} \qquad (A8)$$

The Thermal Energy Equation, (A5), can be written as

$$\frac{\dot{m}c_p}{r}\frac{dT}{dr} - \frac{\lambda}{r}\frac{d}{dr}\left(r\frac{dT}{dr}\right) = \frac{H_{CO}\mathscr{R}_{CO}}{?} \qquad (A9)$$

Because mass must be conserved, the gas phase mass reaction rates in equations (A6) to (A8) must add up to zero, that is

$$-R_{O_2} - R_{CO} + R_{CO_2} = 0 \qquad (A10)$$

From the gas phase reaction formula, $CO + 1/2\ O_2 \rightarrow CO_2$, it can be seen that for every mole of CO_2 formed, one mole of CO and 1/2 mole of O_2 are consumed. Therefore, in molar units,

$$\mathscr{R}_{CO_2} = \mathscr{R}_{CO} \qquad (A11)$$

and

$$\mathscr{R}_{O_2} = \frac{1}{2}\mathscr{R}_{CO} \qquad (A12)$$

The mass reaction rates, R_i, and the molar reaction rates, $\mathscr{R}_i$, are related by the equation

$$R_i = \mathscr{R}_i M_i$$

where M_i = molecular weight of species i.

Equations (A11) and (A12) can thus be written as

$$R_{CO_2} = M_{CO_2} \mathscr{R}_{CO} \tag{A13}$$

$$R_{O_2} = \frac{1}{2} M_{O_2} \mathscr{R}_{CO} \tag{A14}$$

and, in the same manner, R_{CO} can be written as

$$R_{CO} = M_{CO} \mathscr{R}_{CO} \tag{A15}$$

Substituting equations (A14) into (A6), (A13) into (A7), and (A15) into (A8), and substituting $\tau = T/T_b$, where T_b = temperature at the edge of the stagnant film, into (A9), the following equations are obtained.

$$\frac{\dot{m}}{r} \frac{dY_{O_2}}{dr} - \frac{\rho D_{O_2}}{r} \frac{d}{dr}\left(r \frac{dY_{O_2}}{dr}\right) = -\frac{1}{2} M_{O_2} \mathscr{R}_{CO} \tag{A16}$$

$$\frac{\dot{m}}{r} \frac{dY_{CO_2}}{dr} - \frac{\rho D_{CO_2}}{r} \frac{d}{dr}\left(r \frac{dY_{CO_2}}{dr}\right) = M_{CO_2} \mathscr{R}_{CO} \tag{A17}$$

$$\frac{\dot{m}}{r}\frac{dY_{CO}}{dr} - \frac{\rho D_{CO}}{r}\frac{d}{dr}\left(r\frac{dY_{CO}}{dr}\right) = -M_{CO}\mathscr{R}_{CO} \qquad \text{(A18)}$$

$$\frac{\dot{m}c_p T_b}{r}\frac{d\tau}{dr} - \frac{\lambda T_b}{r}\frac{d}{dr}\left(r\frac{d\tau}{dr}\right) = \frac{H_{CO}\mathscr{R}_{CO}}{2} \qquad \text{(A19)}$$

B. Determination of the Burning Rate.

To determine the burning rate of carbon, the surface reactions must be considered. From Figure A1, it can be seen that for every molecule of O_2 that reacts at the surface, two molecules of CO are formed. Therefore, two atoms of carbon are removed from the surface. The molar rate of formation of CO at the surface is equal to twice the molar consumption rate of O_2 at the surface. Therefore, the mass of carbon removed from the surface by O_2 is $M_c 2\mathscr{R}_{O_{2S}}$. From Figure A2, it can be seen that for every molecule of CO_2 that reacts at the surface, two molecules of CO are formed. But, because one carbon atom is carried to the surface by the CO_2 molecule, only one carbon atom is removed from the surface in forming two CO molecules. Therefore, the mass of carbon removed form the surface by CO_2 is $M_C\mathscr{R}_{CO_{2S}}$. The total mass flow from the surface is, therefore,

$$\dot{m}_1 = M_C\left(2\mathscr{R}_{O_{2S}} + \mathscr{R}_{CO_{2S}}\right) \qquad \text{(A20)}$$

or

$$\dot{m} = M_C r_s\left(2\mathscr{R}_{O_{2S}} + \mathscr{R}_{CO_{2S}}\right) \qquad \text{(A21)}$$

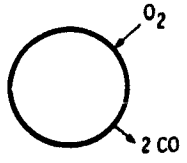

Figure A1. - Surface reaction for $2C + O_2 \cdot 2CO$.

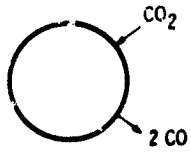

Figure A2. - Surface reaction for $C + CO_2 - 2CO$.

where M_C = molecular weight of carbon;

$\mathscr{R}_{O_{2S}}$ = molar surface reaction rate of oxygen;

$\mathscr{R}_{CO_{2S}}$ = molar surface reaction rate of carbon dioxide; and

r_S = radius of carbon rod.

C. Determination of Boundary Conditions.

At the surface of the rod, it is assumed that all the CO_2 molecules that hit the surface react. Therefore, in terms of the molar flux $N_{CO_{2S}}$,

$$-N_{CO_{2S}} = \mathscr{R}_{CO_{2S}} \tag{A22}$$

Because the molar flux and the mass flux are related by

$$\frac{n_i}{M_i} = N_i,$$

equation (A22) can be written as

$$n_{CO_{2S}} = -M_{CO_2}\mathscr{R}_{CO_{2S}} \tag{A23}$$

Using equation (A2), equation (A23) can be written as

$$-\rho D_{CO_2}\left.\frac{dY_{CO_2}}{dr}\right|_S + \rho Y_{CO_{2S}} v = -M_{CO_2}\mathscr{R}_{CO_{2S}}$$

Using $\rho r v = \dot{m}$ this equation becomes

$$-\left.\frac{\rho D_{CO_2}}{M_{CO_2}}\frac{dY_{CO_2}}{dr}\right|_S + \frac{\dot{m} Y_{CO_{2S}}}{r_S M_{CO_2}} = -\mathscr{R}_{CO_{2S}} \tag{A24}$$

All the O_2 molecules that reach the surface react, so

$$-N_{O_{2S}} = \mathscr{R}_{O_{2S}} \tag{A25}$$

By following the same procedure it can be shown that

$$-\frac{\rho D_{O_2}}{M_{O_2}} \frac{dY_{O_2}}{dr}\bigg|_S + \frac{\dot{m} Y_{O_{2S}}}{r_S M_{O_2}} = -\mathscr{R}_{O_{2S}} \tag{A26}$$

Because every molecule of O_2 that reaches the surface forms two molecules of CO, and every molecule of CO_2 that reaches the surface forms two CO molecules, the molar reaction rates are related by the equation

$$\mathscr{R}_{CO_S} = 2\left(\mathscr{R}_{O_{2S}} + \mathscr{R}_{CO_{2S}}\right)$$

Therefore, at the surface of the carbon, the flux of CO is

$$N_{CO_S} + 2\left(\mathscr{R}_{O_{2S}} + \mathscr{R}_{CO_{2S}}\right)$$

or

$$n_{CO_S} = 2M_{CO}\left(\mathscr{R}_{O_{2S}} + \mathscr{R}_{CO_{2S}}\right) \tag{A27}$$

Using equation (A2) and $\rho r v = \dot{m}$, equation (A27) can be written as

$$-\frac{\rho D_{CO}}{M_{CO}} \frac{dY_{CO}}{dr}\bigg|_S + \frac{\dot{m} Y_{CO_S}}{r_S M_{CO}} = 2\left(\mathscr{R}_{O_{2S}} + \mathscr{R}_{CO_{2S}}\right) \tag{A28}$$

At the surface the heat flux is equal to the heat produced by the reaction, $2C + O_2 \rightarrow 2CO$ (H_{O_2}), and the heat absorbed by the reaction, $C + CO_2 \rightarrow 2CO$ (H_{CO_2}), or

$$-\lambda \left.\frac{dT}{dr}\right|_S = H_{O_2} \mathscr{R}_{O_{2S}} - H_{CO_2} \mathscr{R}_{CO_{2S}}$$

where H_{O_2} = heat produced by one mole of oxygen reacting with carbon to produce two moles of carbon monoxide; and

H_{CO_2} = heat absorbed by one mole of carbon dioxide reacting with carbon to produce two moles of carbon monoxide.

Using $\tau = T/T_b$ this equation becomes

$$-\lambda T_b \left.\frac{d\tau}{dr}\right|_S = H_{O_2} \mathscr{R}_{O_{2S}} - H_{CO_2} \mathscr{R}_{CO_{2S}} \qquad \text{(A29)}$$

At the outer edge of the stagnant film, the following conditions are assumed. At $r = r_b$,

$$Y_{O_2} = Y_{O_{2b}} \qquad \text{(A30)}$$

$$Y_{CO_2} = Y_{CO_{2b}} \qquad \text{(A31)}$$

$$Y_{CO} = 0 \qquad \text{(A32)}$$

$$\tau = 1 \tag{A33}$$

C. Solution of Covering Equations.

The equations to be solved are (A16), (A17), (A18), and (A19), and can be written as:

$$\frac{\dot{2m}}{rM_{O_2}} \frac{dY_{O_2}}{dr} - \frac{2\rho D_{O_2}}{rM_{O_2}} \frac{d}{dr}\left(r \frac{dY_{O_2}}{dr}\right) = -\mathscr{R}_{CO} \tag{A16}$$

$$\frac{\dot{m}}{rM_{CO_2}} \frac{dY_{CO_2}}{dr} - \frac{\rho D_{CO_2}}{rM_{CO_2}} \frac{d}{dr}\left(r \frac{dY_{CO_2}}{dr}\right) = \mathscr{R}_{CO} \tag{A17}$$

$$\frac{\dot{m}}{rM_{CO}} \frac{dY_{CO}}{dr} - \frac{\rho D_{CO}}{rM_{CO}} \frac{d}{dr}\left(r \frac{dY_{CO}}{dr}\right) = -\mathscr{R}_{CO} \tag{A18}$$

$$\frac{\dot{2mc}_p T_b}{rH_{CO}} \frac{d\tau}{dr} - \frac{2\lambda T_b}{rH_{CO}} \frac{d}{dr}\left(r \frac{d\tau}{dr}\right) = \mathscr{R}_{CO} \tag{A19}$$

The boundary conditions at the surface are equations (A24), (A26), (A28), and (A29), at $r = r_s$:

$$-\left.\frac{\rho D_{CO_2}}{M_{CO_2}} \frac{dY_{CO_2}}{dr}\right|_s + \frac{\dot{m} Y_{CO_{2S}}}{r_s M_{CO_2}} = -\mathscr{R}_{CO_{2S}} \tag{A24}$$

$$-\frac{\rho D_{O_2}}{M_{O_2}}\frac{dY_{O_2}}{dr}\bigg|_s + \frac{\dot{m}Y_{O_{2S}}}{r_s M_{O_2}} = -\mathscr{R}_{O_{2S}} \tag{A26}$$

$$-\frac{\rho D_{CO}}{M_{CO}}\frac{dY_{CO}}{dr}\bigg|_s + \frac{\dot{m}Y_{CO_S}}{r_s M_{CO}} = 2\left(\mathscr{R}_{O_{2S}} + \mathscr{R}_{CO_{2S}}\right) \tag{A28}$$

$$-\lambda T_b \frac{d\tau}{dr}\bigg|_s = H_{O_2}\mathscr{R}_{O_{2S}} - H_{CO_2}\mathscr{R}_{CO_{2S}} \tag{A29}$$

The boundary conditions at the outer edge of the stagnant layer are at $r = r_b$:

$$Y_{O_2} = Y_{O_{2b}} \tag{A30}$$

$$Y_{CO_2} = Y_{CO_{2b}} \tag{A31}$$

$$Y_{CO} = 0 \tag{A32}$$

$$\tau = 1 \tag{A33}$$

By combining equations (A16) with (A17), (A17) with (A18), and (A17) with (A19), the CO molar reaction rate term, $\mathscr{R}_{CO}$, was eliminated from the equations. The resulting equations were multiplied through by r, yielding

$$\frac{2\dot{m}}{M_{O_2}} \frac{dY_{O_2}}{dr} - \frac{2\rho D_{O_2}}{M_{O_2}} \frac{d}{dr}\left(r \frac{dY_{O_2}}{dr}\right) + \frac{\dot{m}}{M_{CO_2}} \frac{dY_{CO_2}}{dr} - \frac{\rho D_{CO_2}}{M_{CO_2}} \frac{d}{dr}\left(r \frac{dY_{CO_2}}{dr}\right) = 0 \tag{A34}$$

$$\frac{\dot{m}}{M_{CO}} \frac{dY_{CO}}{dr} - \frac{\rho D_{CO}}{M_{CO}} \frac{d}{dr}\left(r \frac{dY_{CO}}{dr}\right) + \frac{\dot{m}}{M_{CO_2}} \frac{dY_{CO_2}}{dr} - \frac{\rho D_{CO_2}}{M_{CO_2}} \frac{d}{dr}\left(r \frac{dY_{CO_2}}{dr}\right) = 0 \tag{A35}$$

$$\frac{2\dot{m}c_p T_b}{H_{CO}} \frac{d\tau}{dr} - \frac{2\lambda T_b}{H_{CO}} \frac{d}{dr}\left(r \frac{d\tau}{dr}\right) - \frac{\dot{m}}{M_{CO_2}} \frac{dY_{CO_2}}{dr} + \frac{\rho D_{CO_2}}{M_{CO_2}} \frac{d}{dr}\left(r \frac{dY_{CO_2}}{dr}\right) = 0 \tag{A36}$$

The equations for the boundary conditions were also combined. Equation (A26) was multiplied by two and combined with equation (A24), equations (A28) and (A24) were combined, and equation (A29) was multiplied by $2/H_{CO}$ and combined with equation (A24) yielding

$$-\frac{2D_{O_2}\rho}{M_{O_2}}\frac{dY_{O_2}}{dr}\bigg|_s + \frac{2\dot{m}Y_{O_{2S}}}{r_s M_{O_2}} - \frac{\rho D_{CO_2}}{M_{CO_2}}\frac{dY_{CO_2}}{dr}\bigg|_s + \frac{\dot{m}Y_{CO_{2S}}}{r_s M_{CO_2}} = -\left(2\mathscr{R}_{O_{2S}} + \mathscr{R}_{CO_{2S}}\right) \tag{A37}$$

$$-\frac{\rho D_{CO}}{M_{CO}}\frac{dY_{CO}}{dr}\bigg|_s + \frac{\dot{m}Y_{CO_S}}{r_s M_{CO}} - \frac{\rho D_{CO_2}}{M_{CO_2}}\frac{dY_{CO_2}}{dr}\bigg|_s + \frac{\dot{m}Y_{CO_{2S}}}{r_s M_{CO_2}} = 2\mathscr{R}_{O_{2S}} + \mathscr{R}_{CO_{2S}} \tag{A38}$$

$$-\frac{2\lambda T_b}{H_{CO}}\frac{d\tau}{dr}\bigg|_s + \frac{\rho D_{CO_2}}{M_{CO_2}}\frac{dY_{CO_2}}{dr}\bigg|_s - \frac{\dot{m}Y_{CO_{2S}}}{r_s M_{CO_2}}$$

$$= \frac{2}{H_{CO}}\left(H_{O_2}\mathscr{R}_{O_{2S}} - H_{CO_2}\mathscr{R}_{CO_{2S}}\right) + \mathscr{R}_{CO_2} \tag{A39}$$

The boundary conditions at the outer edge of the stagnant film were likewise combined. The equations containing mass fractions were divided through by the respective molecular weights, and the equation containing τ was multiplied through by $-2c_pT_b/H_{CO}$. Also, the equation containing Y_{O_2}, that is, equation (A30), was multiplied by two. Performing the above steps, then combining equations (A30) and (A31), (A31) and (A32), and (A31) and (A33) yields

$$\frac{2Y_{O_2}}{M_{O_2}} + \frac{Y_{CO_2}}{M_{CO_2}} = \frac{2Y_{O_{2b}}}{M_{O_2}} + \frac{Y_{CO_{2b}}}{M_{CO_2}} \tag{A40}$$

$$\frac{Y_{CO_2}}{M_{CO_2}} + \frac{Y_{CO}}{M_{CO}} = \frac{Y_{CO_{2b}}}{M_{CO_2}} \tag{A41}$$

$$\frac{Y_{CO_2}}{M_{CO_2}} - \frac{2c_pT_b}{H_{CO}}\tau = \frac{Y_{CO_{2b}}}{M_{CO_2}} - \frac{2c_pT_b}{H_{CO}} \tag{A42}$$

Equation (A34) was integrated, yielding

$$\frac{2\dot{m}Y_{O_2}}{M_{O_2}} - \frac{2\rho D_{O_2}}{M_{O_2}} r \frac{dY_{O_2}}{dr} + \frac{\dot{m}Y_{CO_2}}{M_{CO_2}} - \frac{\rho D_{CO_2}}{M_{CO_2}} r \frac{dY_{CO_2}}{dr} = A \tag{A43}$$

This equation, evaluated at the surface, gives

$$\frac{2\dot{m}Y_{O_{2S}}}{M_{O_2}} - \frac{2\rho D_{O_2}}{M_{O_2}} r_S \left.\frac{dY_{O_2}}{dr}\right|_S + \frac{\dot{m}Y_{CO_{2S}}}{M_{CO_2}} - \frac{\rho D_{CO_2}}{M_{CO_2}} r_S \left.\frac{dY_{CO_2}}{dr}\right|_S = A$$

and, compared to the surface boundary condition, equation (A37), written as

$$\frac{2\dot{m}Y_{O_{2S}}}{M_{O_2}} - \frac{2D_{O_2}\rho}{M_{O_2}} r_S \left.\frac{dY_{O_2}}{dr}\right|_S + \frac{\dot{m}Y_{CO_{2S}}}{M_{CO_2}} - \frac{\rho D_{CO_2}}{M_{CO_2}} r_S \left.\frac{dY_{CO_2}}{dr}\right|_S$$

$$= -\left(2\mathscr{R}_{O_{2S}} + \mathscr{R}_{CO_{2S}}\right) r_S,$$

the value of the constant A is determined as

$$A = -\left(2\mathscr{R}_{O_{2S}} + \mathscr{R}_{CO_{2S}}\right) r_S \tag{A44}$$

Using the Schwab-Zeldovich approximation $D_{O_2} = D_{CO_2} = D$, equation (A43) can be written as

$$\frac{2}{M_{O_2}}\left(-\frac{\dot{m}}{\rho D r} Y_{O_2} + \frac{dY_{O_2}}{dr}\right) + \frac{1}{M_{CO_2}}\left(-\frac{\dot{m}}{\rho D r} Y_{CO_2} + \frac{dY_{CO_2}}{dr}\right) = -\frac{A}{\rho D r}$$

Using the integrating factor $e^{-\int(\dot{m}/\rho D r)dr} = r^{-\dot{m}/\rho D}$, this equation was integrated, yielding

$$\frac{2}{M_{O_2}}\left(Y_{O_2} r^{-\dot{m}/\rho D}\right) + \frac{1}{M_{CO_2}}\left(Y_{CO_2} r^{-\dot{m}/\rho D}\right) = -\int \frac{A}{\rho D}\frac{1}{r} r^{-\dot{m}/\rho D}\, dr$$

or

$$\frac{2}{M_{O_2}}\left(Y_{O_2} r^{-\dot{m}/\rho D}\right) + \frac{1}{M_{CO_2}}\left(Y_{CO_2} r^{-\dot{m}/\rho D}\right) = \frac{A}{\rho D\left(\frac{\dot{m}}{\rho D}\right)} r^{-\dot{m}/\rho D} + C_1$$

which reduces to

$$\frac{2}{M_{O_2}} Y_{O_2} + \frac{1}{M_{CO_2}} Y_{CO_2} = \frac{A}{\dot{m}} + C_1 r^{\dot{m}/\rho D} \qquad \text{(A45)}$$

Evaluating equation (A45) at $r = r_b$ and using equation (A40), yields

$$\frac{2}{M_{O_2}} Y_{O_{2b}} + \frac{1}{M_{CO_2}} Y_{CO_{2b}} = \frac{A}{\dot{m}} + C_1 r_b^{\dot{m}/\rho D}$$

Therefore the constant C_1 is

$$C_1 = \left(\frac{2Y_{O_{2b}}}{M_{O_2}} + \frac{Y_{CO_{2b}}}{M_{CO_2}} - \frac{A}{\dot{m}}\right)\frac{1}{r_b^{\dot{m}/\rho D}}$$

Substituting equation (A44) for the constant A in this equation, and substituting the resulting equation for the constant C_1 and equation (A44) into equation (A45), yields

$$\frac{2}{M_{O_2}} Y_{O_2} + \frac{1}{M_{CO_2}} Y_{CO_2} = - \frac{r_s}{\dot{m}} \left(2\mathscr{R}_{O_{2S}} + \mathscr{R}_{CO_{2S}} \right)$$

$$+ \left[\frac{2Y_{O_{2b}}}{M_{O_2}} + \frac{Y_{CO_{2b}}}{M_{CO_2}} + \frac{r_s}{\dot{m}} \left(2\mathscr{R}_{O_{2S}} + \mathscr{R}_{CO_{2S}} \right) \right] \left(\frac{r}{r_b} \right)^{\dot{m}/\rho D} \qquad \text{(A46)}$$

Using equation (A21), $\dot{m} = M_C r_s (2\mathscr{R}_{O_{2S}} + \mathscr{R}_{CO_{2S}})$, equation (A46) can be written as

$$\frac{2Y_{O_2}}{M_{O_2}} + \frac{Y_{CO_2}}{M_{CO_2}} = - \frac{1}{M_C} + \left(\frac{2Y_{O_{2b}}}{M_{O_2}} + \frac{Y_{CO_{2b}}}{M_{CO_2}} + \frac{1}{M_C} \right) \left(\frac{r}{r_b} \right)^{\dot{m}/\rho D} \qquad \text{(A47)}$$

Equation (A35) was solved exactly like (A34). Because the equations and the boundary conditions are basically the same, only the result is presented:

$$\frac{Y_{CO}}{M_{CO}} + \frac{Y_{CO_2}}{M_{CO_2}} = \frac{1}{M_C} + \left(\frac{Y_{CO_{2b}}}{M_{CO_2}} - \frac{1}{M_C} \right) \left(\frac{r}{r_b} \right)^{\dot{m}/\rho D} \qquad \text{(A48)}$$

Equation (A36) was integrated, yielding

$$\frac{2\dot{m} c_p T_b}{H_{CO}} \tau - \frac{2\lambda T_b}{H_{CO}} r \frac{d\tau}{dr} - \frac{\dot{m}}{M_{CO_2}} Y_{CO_2} + \frac{\rho D_{CO_2}}{M_{CO_2}} r \frac{dY_{CO_2}}{dr} = A'' \qquad \text{(A49)}$$

Writing this equation at the surface

$$\frac{2\dot{m} c_p T_b}{H_{CO}} \tau_s - \frac{2\lambda T_b}{H_{CO}} r_s \left. \frac{d\tau}{dr} \right|_s - \frac{\dot{m}}{M_{CO_2}} Y_{CO_{2S}} + \frac{\rho D_{CO_2}}{M_{CO_2}} r_s \left. \frac{dY_{CO_2}}{dr} \right|_s = A''$$

and comparing it with boundary condition (A39) multiplied through by r_s,

$$-\frac{2\lambda T_b r_s}{H_{CO}}\frac{d\tau}{dr}\bigg|_s + \frac{\rho D_{CO_2} r_s}{M_{CO_2}}\frac{dY_{CO_2}}{dr}\bigg|_s - \frac{\dot{m} Y_{CO_2 s}}{M_{CO_2}}$$

$$= \frac{2r_s}{H_{CO}}\left(H_{O_2}\mathscr{R}_{O_2 s} - H_{CO_2}\mathscr{R}_{CO_2 s}\right) + \mathscr{R}_{CO_2} r_s,$$

shows that

$$A'' = \frac{2\dot{m} c_p T_b}{H_{CO}}\tau_s + \frac{2r_s}{H_{CO}}\left(H_{O_2}\mathscr{R}_{O_2 s} - H_{CO_2}\mathscr{R}_{CO_2 s}\right) + \mathscr{R}_{CO_2 s} r_s$$

or

$$A'' = \frac{2\dot{m} c_p T_b}{H_{CO}}\tau_s + \frac{r_s}{H_{CO}}\left(2H_{O_2}\mathscr{R}_{O_2 s} - 2H_{CO_2}\mathscr{R}_{CO_2 s} + \mathscr{R}_{CO_2 s} H_{CO}\right) \qquad \text{(A50)}$$

The chemical formulae with the heat of reaction for the CO_2 surface reaction and the gas phase reaction can be written as

$$2C + 2CO_2 \rightarrow 4CO,\ 2H_{CO_2}$$

$$2CO + O_2 \rightarrow 2CO_2,\ H_{CO}$$

Adding these equations yields

$$2C + O_2 \rightarrow 2CO,\ \left(H_{CO} - 2H_{CO_2}\right)$$

Comparing this formula to the chemical formula with the heat of reaction for the O_2 reaction at the surface,

$$2C + O_2 \rightarrow 2CO,\ H_{O_2},$$

shows that

$$H_{O_2} = \left(H_{CO} - 2H_{CO_2}\right) \tag{A51}$$

Rewriting equation (A50) as

$$A'' = \frac{2\dot{m}c_p T_b}{H_{CO}} \tau_S + \frac{r_S}{H_{CO}} \left[2H_{O_2} \mathscr{R}_{O_{2S}} + \mathscr{R}_{CO_{2S}} \left(-2H_{CO_2} + H_{CO}\right)\right]$$

and substituting equation (A51) into it, yields

$$A'' = \frac{2\dot{m}c_p T_b}{H_{CO}} \tau_S + \frac{r_S}{H_{CO}} \left(2H_{O_2} \mathscr{R}_{O_{2S}} + \mathscr{R}_{CO_{2S}} H_{O_2}\right)$$

or

$$A'' = \frac{2\dot{m}c_p T_b}{H_{CO}} \tau_S + \frac{r_S H_{O_2}}{H_{CO}} \left(2\mathscr{R}_{O_{2S}} + \mathscr{R}_{CO_{2S}}\right) \tag{A52}$$

Using the Schwab-Zeldovich approximation, $D_{CO_2} = \lambda/\rho c_p = D$, equation (A49) can be written as

$$\frac{2\dot{m}c_p T_b}{H_{CO}} \tau - \frac{2D\rho c_p T_b}{H_{CO}} r \frac{d\tau}{dr} - \frac{\dot{m}}{M_{CO_2}} Y_{CO_2} + \frac{\rho D}{M_{CO_2}} r \frac{dY_{CO_2}}{dr} = A''$$

or

$$-\frac{2c_p T_b}{H_{CO}} \left(-\dot{m}\tau + \rho D r \frac{d\tau}{dr}\right) + \frac{1}{M_{CO_2}} \left(-\dot{m}Y_{CO_2} + \rho D r \frac{dY_{CO_2}}{dr}\right) = A''$$

Dividing this equation through by ρDr yields

$$-\frac{2c_pT_b}{H_{CO}}\left(-\frac{\dot{m}}{\rho Dr}\tau+\frac{d\tau}{dr}\right)+\frac{1}{M_{CO_2}}\left(-\frac{\dot{m}}{\rho Dr}Y_{CO_2}+\frac{dY_{CO_2}}{dr}\right)=\frac{A''}{\rho Dr}$$

Using the integrating factor $e^{-\int(\dot{m}/\rho Dr)dr}=r^{-\dot{m}/\rho D}$, this equation was integrated, yielding

$$-\frac{2c_pT_b}{H_{CO}}\left(\tau r^{-\dot{m}/\rho D}\right)+\frac{1}{M_{CO_2}}\left(Y_{CO_2}r^{-\dot{m}/\rho D}\right)=\int\frac{A''}{\rho D}\frac{1}{r}r^{-\dot{m}/\rho D}\,dr$$

or

$$-\frac{2c_pT_b}{H_{CO}}\left(\tau r^{-\dot{m}/\rho D}\right)+\frac{1}{M_{CO_2}}\left(Y_{CO_2}r^{-\dot{m}/\rho D}\right)=-\frac{A''}{\rho D\left(\frac{\dot{m}}{\rho D}\right)}r^{-\dot{m}/\rho D}+C_2$$

which reduces to

$$-\frac{2c_pT_b}{H_{CO}}\tau+\frac{Y_{CO_2}}{M_{CO_2}}=-\frac{A''}{\dot{m}}+C_2r^{\dot{m}/\rho D} \qquad \text{(A53)}$$

Evaluating equation (A53) at $r=r_b$ and using equation (A42), yields

$$-\frac{2c_pT_b}{H_{CO}}+\frac{Y_{CO_{2b}}}{M_{CO_2}}=-\frac{A''}{\dot{m}}+C_2r_b^{\dot{m}/\rho D}$$

Therefore the constant C_2 is

$$C_2=\left(-\frac{2c_pT_b}{H_{CO}}+\frac{Y_{CO_{2b}}}{M_{CO_2}}+\frac{A''}{\dot{m}}\right)\frac{1}{r_b^{\dot{m}/\rho D}} \qquad \text{(A54)}$$

Substituting equation (A52) for the constant A" into (A54), and substituting the resulting equation for C_2 along with equation (A52) into (A53), yields

$$-\frac{2c_pT_b}{H_{CO}}\tau+\frac{Y_{CO_2}}{M_{CO_2}}=-\frac{2c_pT_b}{H_{CO}}\tau_S-\frac{r_sH_{O_2}}{\dot{m}H_{CO}}\left(2\mathscr{R}_{O_{2S}}+\mathscr{R}_{CO_{2S}}\right)$$

$$+\left[-\frac{2c_pT_b}{H_{CO}}+\frac{Y_{CO_{2b}}}{M_{CO_2}}+\frac{2c_pT_b}{H_{CO}}\tau_S+\frac{r_sH_{O_2}}{\dot{m}H_{CO}}\left(2\mathscr{R}_{O_{2S}}+\mathscr{R}_{CO_{2S}}\right)\right]\left(\frac{r}{r_b}\right)^{\dot{m}/\rho D} \quad \text{(A55)}$$

Using equation (A21), equation (A55) can be written as

$$-\frac{2c_pT_b}{H_{CO}}\tau+\frac{Y_{CO_2}}{M_{CO_2}}=-\frac{2c_pT_b}{H_{CO}}\tau_S-\frac{H_{O_2}}{M_cH_{CO}}$$

$$+\left(-\frac{2c_pT_b}{H_{CO}}+\frac{Y_{CO_{2b}}}{M_{CO_2}}+\frac{2c_pT_b}{H_{CO}}\tau_S+\frac{H_{O_2}}{M_cH_{CO}}\right)\left(\frac{r}{r_b}\right)^{\dot{m}/\rho D}$$

or

$$-\frac{2c_pT_bM_{CO_2}}{H_{CO}}\tau+Y_{CO_2}=-\frac{2c_pT_bM_{CO_2}}{H_{CO}}\tau_S-\frac{H_{O_2}M_{CO_2}}{H_{CO}M_c}$$

$$+\left(\frac{2c_pT_bM_{CO_2}}{H_{CO}}\tau_S+\frac{H_{O_2}M_{CO_2}}{M_cH_{CO}}+Y_{CO_{2b}}-\frac{2c_pT_bM_{CO_2}}{H_{CO}}\right)\left(\frac{r}{r_b}\right)^{\dot{m}/\rho D} \quad \text{(A56)}$$

Letting

$$\beta = \frac{M_{CO_2} c_p T_b}{H_{CO}} \tag{A57}$$

$$\varepsilon = \frac{M_{CO_2} H_{O_2}}{M_C H_{CO}}, \tag{A58}$$

equation (A56) can be written as

$$-2\beta\tau + Y_{CO_2} = -2\beta\tau_S - \varepsilon + \left(2\beta\tau_S + \varepsilon + Y_{CO_{2b}} - 2\beta\right)\left(\frac{r}{r_b}\right)^{\dot{m}/\rho D} \tag{A59}$$

Letting

$$\gamma = \frac{\dot{m}}{\rho D}, \tag{A60}$$

the solution to equations (A34), (A35), and (A36), which are equations (A47), (A48), and (A59), can be written as

$$Y_{O_2} = -\frac{M_{O_2}}{2M_C} + \left(Y_{O_{2b}} + \frac{M_{O_2}}{2M_{CO_2}} Y_{CO_{2b}} + \frac{M_{O_2}}{2M_C}\right)\left(\frac{r}{r_b}\right)^{\gamma} - \frac{M_{O_2}}{2M_{CO_2}} Y_{CO_2} \tag{A61}$$

$$Y_{CO} = \frac{M_{CO}}{M_C} + \left(\frac{M_{CO}}{M_{CO_2}} Y_{CO_{2b}} - \frac{M_{CO}}{M_C}\right)\left(\frac{r}{r_b}\right)^{\gamma} - \frac{M_{CO}}{M_{CO_2}} Y_{CO_2} \tag{A62}$$

$$-2\beta\tau = -Y_{CO_2} - 2\beta\tau_S - \varepsilon + \left(2\beta\tau_S + \varepsilon + Y_{CO_{2b}} - 2\beta\right)\left(\frac{r}{r_b}\right)^{\gamma} \tag{A63}$$

Assuming the gas phase reaction $2CO + O_2 \rightarrow 2CO_2$ is first order with respect to CO and O_2, the volume rate of consumption of CO can be written as

$$\mathscr{R}_{CO} = k_g C_{CO} C_{O_2} \exp(-E/RT) \tag{A64}$$

where k_g = frequency or pre-exponential factor for the gas phase reaction $CO + 1/2\ O_2 \rightarrow CO_2$;

C_{CO} = molar concentration of carbon monoxide;

C_{O_2} = molar concentration of oxygen;

E = activation energy for the gas phase reaction; $CO + 1/2\ O_2 \rightarrow CO_2$; and

R = universal gas constant.

Letting

$$\delta_1 = \frac{E}{RT_b} \tag{A65}$$

and using the relationship

$$C_i = \frac{\rho Y_i}{M_i},$$

equation (A64) can be written as

$$\mathscr{R}_{CO} = k_g \frac{\rho^2}{M_{CO} M_{O_2}} Y_{CO} Y_{O_2} \exp(-\delta_1/\tau) \tag{A66}$$

Equation (A61), (A62), and (A63) can be substituted into equation (A66). The resulting equation can be substituted into the differential equation for CO_2, (A17), which then can be solved using a Runge-Kutta technique to obtain the CO_2 concentration as a function

of distance from the surface. However, because the CO_2 concentration should first increase with distance from the surface and then decrease, it was found that equation (A18) for the CO concentration, which just decreases with distance from the surface, would be better to use in the Runge-Kutta technique.

Equations (A61), (A62), and (A63) were solved so that $Y_{CO_2} = f(Y_{CO}, r)$, $Y_{O_2} = f(Y_{CO}, r)$, and $\tau = f(Y_{CO}, r)$. The resulting equations are

$$Y_{O_2} = \left(Y_{O_{2b}} + \frac{M_{O_2}}{M_C}\right)\left(\frac{r}{r_b}\right)^{\gamma} + \frac{M_{O_2}}{2M_C} Y_{CO} - \frac{M_{O_2}}{M_C} \tag{A67}$$

$$Y_{CO_2} = -\frac{M_{CO_2}}{M_{CO}} Y_{CO} + \left(Y_{CO_{2b}} - \frac{M_{CO_2}}{M_C}\right)\left(\frac{r}{r_b}\right)^{\gamma} + \frac{M_{CO_2}}{M_C} \tag{A68}$$

$$\tau = \tau_S + \frac{1}{2\beta}\left\{\epsilon + \frac{M_{CO_2}}{M_C} - \frac{M_{CO_2}}{M_{CO}} Y_{CO} - \left[2\beta(\tau_S - 1) + \epsilon + \frac{M_{CO_2}}{M_C}\right]\left(\frac{r}{r_b}\right)^{\gamma}\right\} \tag{A69}$$

The differential equation for the concentration of CO, equation (A18), can be written as

$$\frac{\dot{m}}{r}\frac{dY_{CO}}{dr} - \frac{\rho D}{r}\frac{dY_{CO}}{dr} - \rho D \frac{d^2 Y_{CO}}{dr^2} = -M_{CO}\mathscr{R}_{CO}$$

or

$$\left(\frac{\dot{m}}{r\rho D} - \frac{1}{r}\right)\frac{dY_{CO}}{dr} - \frac{d^2 Y_{CO}}{dr^2} = -\frac{M_{CO}}{\rho D}\mathscr{R}_{CO}$$

Using

$$\gamma = \frac{\dot{m}}{\rho D}$$

and rearranging, this equation becomes

$$\frac{d^2 Y_{CO}}{dr^2} = \frac{M_{CO}}{\rho D} \mathscr{R}_{CO} - \frac{(1 - \gamma)}{r} \frac{dY_{CO}}{dr} \tag{A70}$$

Denoting equation (A67) and (A69) by $Y_{O_2} = Y_{O_2}(Y_{CO}, r)$ and $\tau = \tau(Y_{CO}, r)$, respectively, and substituting these into equation (A66), and substituting the result into equation (A70), yields

$$\frac{d^2 Y_{CO}}{dr^2} = k_g \frac{\rho}{DM_{O_2}} Y_{CO} Y_{O_2}(Y_{CO,r}) \exp\left[-\delta_1/\tau(y_{CO,r})\right] - \frac{(1 - \gamma)}{r} \frac{dY_{CO}}{dr} \tag{A71}$$

If one of the variables Y_{O_2}, Y_{CO_2}, Y_{CO}, or τ is known, the others can be determined using equations (A61), (A62), and (A63). In this case, the surface temperature is considered to be known; therefore, $Y_{O_{2S}}$, $Y_{CO_{2S}}$, and Y_{CO_S} can be determined.

To determine these variables, first the consumption rates of O_2 and CO_2 at the surface are written as

$$\mathscr{R}_{O_2} = k_{O_2} C_{O_2}$$

and

$$\mathscr{R}_{CO_2} = k_{CO_2} C_{CO_2}$$

where k_{O_2} = rate constant for the reaction, $2C + O_2 \rightarrow 2CO$;

k_{CO_2} = rate constant for the reaction, $C + CO_2 \rightarrow 2CO$;

C_{O_2} = molar concentration of oxygen; and

C_{CO_2} = molar concentration of carbon dioxide.

Using the relationship

$$C_i = \frac{\rho Y_i}{M_i},$$

these equations become

$$\mathscr{R}_{O_{2S}} = \frac{\rho}{M_{O_2}} k_{O_2} Y_{O_{2S}} \tag{A72}$$

and

$$\mathscr{R}_{CO_{2S}} = \frac{\rho}{M_{CO_2}} k_{CO_2} Y_{CO_{2S}} \tag{A73}$$

Substituting equations (A72) and (A73) into (A21) yields

$$\dot{m} = \rho M_C r_S \left(2k_{O_2} \frac{Y_{O_{2S}}}{M_{O_2}} + k_{CO_2} \frac{Y_{CO_{2S}}}{M_{CO_2}} \right)$$

and, therefore,

$$\gamma = \frac{\dot{m}}{\rho D} = \frac{M_C r_S}{D} \left(2k_{O_2} \frac{Y_{O_{2S}}}{M_{O_2}} + k_{CO_2} \frac{Y_{CO_{2S}}}{M_{CO_2}} \right) \tag{A74}$$

Next equations (A61) and (A63) are evaluated at the surface, yielding

$$Y_{O_{2S}} = - \frac{M_{O_2}}{2M_C} - \frac{M_{O_2}}{2M_{CO_2}} Y_{CO_{2S}} + \left(Y_{O_{2b}} + \frac{M_{O_2}}{2M_{CO_2}} Y_{CO_{2b}} + \frac{M_{O_2}}{2M_C} \right) \left(\frac{r_S}{r_b} \right)^{\gamma} \tag{A75}$$

and

$$Y_{CO_{2S}} = -\varepsilon + \left[2\beta(\tau_S - 1) + \varepsilon + Y_{CO_{2b}} \right] \left(\frac{r_S}{r_b} \right)^{\gamma} \tag{A76}$$

Letting

$$\left(Y_{O_{2b}} + \frac{M_{O_2}}{2M_{CO_2}} Y_{CO_{2b}} + \frac{M_{O_2}}{2M_C} \right) = C_1$$

and

$$\left[2\beta(\tau_s - 1) + \varepsilon + Y_{CO_{2b}}\right] = C_2,$$

equations (A75) and (A76) can be written as

$$Y_{O_{2S}} = -\frac{M_{O_2}}{2M_C} - \frac{M_{O_2}}{2M_{CO_2}} Y_{CO_{2S}} + C_1 \left(\frac{r_s}{r_b}\right)^{\gamma} \tag{A77}$$

$$Y_{CO_{2S}} = -\varepsilon + C_2 \left(\frac{r_s}{r_b}\right)^{\gamma} \tag{A78}$$

Rewriting these equations as

$$\frac{Y_{O_{2S}}}{C_1} = -\frac{M_{O_2}}{2C_1 M_C} - \frac{M_{O_2}}{2C_1 M_{CO_2}} Y_{CO_{2S}} + \left(\frac{r_s}{r_b}\right)^{\gamma}$$

and

$$\frac{Y_{CO_{2S}}}{C_2} = -\frac{\varepsilon}{C_2} + \left(\frac{r_s}{r_b}\right)^{\gamma}$$

and subtracting, yields

$$\frac{Y_{O_{2S}}}{C_1} - \frac{Y_{CO_{2S}}}{C_2} = -\frac{M_{O_2}}{2C_1 M_C} - \frac{M_{O_2}}{2C_1 M_{CO_2}} Y_{CO_{2S}} + \frac{\varepsilon}{C_2}$$

or

$$Y_{O_{2S}} = \left(\frac{C_1}{C_2} - \frac{M_{O_2}}{2M_{CO_2}}\right) Y_{CO_{2S}} - \frac{M_{O_2}}{2M_C} + \frac{C_1}{C_2}\varepsilon \tag{A79}$$

Substituting equation (A79) into (A74), yields

$$\gamma = \frac{M_C r_S}{D}\left[\left(\frac{2k_{O_2}}{M_{O_2}}\frac{C_1}{C_2} - \frac{k_{O_2}}{M_{CO_2}} + \frac{k_{CO_2}}{M_{CO_2}}\right)Y_{CO_{2S}} + \frac{2k_{O_2}}{M_{O_2}}\left(\frac{C_1}{C_2}\varepsilon - \frac{M_{O_2}}{2M_C}\right)\right] \qquad \text{(A80)}$$

Letting

$$\frac{M_C r_S}{D}\left(\frac{2k_{O_2}}{M_{O_2}}\frac{C_1}{C_2} - \frac{\nu_{O_2}}{M_{CO_2}} + \frac{k_{CO_2}}{M_{CO_2}}\right) = C_3$$

and

$$\frac{2k_{O_2} M_C r_S}{M_{O_2} D}\left(\frac{C_1}{C_2}\varepsilon - \frac{M_{O_2}}{2M_C}\right) = C_4,$$

equation (A80) can be written as

$$\gamma = C_3 Y_{CO_{2S}} + C_4 \qquad \text{(A81)}$$

Substituting equation (A81) into (A78) yields

$$Y_{CO_{2S}} = -\varepsilon + C_2\left(\frac{r_S}{r_b}\right)^{\left(C_3 Y_{CO_{2S}} + C_4\right)} \qquad \text{(A82)}$$

which was solved by trial and error for $Y_{CO_{2S}}$. Once $Y_{CO_{2S}}$ was obtained, equations (A61) and (A62) were evaluated at the surface and solved for $Y_{O_{2S}}$ and Y_{CO_S}.

The derivative of the mass fraction at the surface with respect to r can be obtained using equations (A24), (A26), and (A28). This will be illustrated using equation (A28). Substituting equations (A72) and (A73) into equation (A28) yields

$$-\frac{\rho D}{M_{CO}}\frac{dY_{CO}}{dr}\bigg|_S + \frac{\dot{m} Y_{CO_S}}{r_S M_{CO}} = \frac{2\rho}{M_{O_2}} k_{O_2} Y_{O_{2S}} + \frac{2\rho}{M_{CO_2}} k_{CO_2} Y_{CO_{2S}}$$

or

$$\left.\frac{dY_{CO}}{dr}\right|_S = \frac{\dot{m}}{r_S \rho D} Y_{CO_S} - \frac{2M_{CO}}{D}\left(\frac{k_{O_2} Y_{O_{2S}}}{M_{O_2}} + \frac{k_{CO_2} Y_{CO_{2S}}}{M_{CO_2}}\right) \qquad \text{(A83)}$$

This equation was solved to obtain the derivative of the mass fraction of CO at the surface.

With the mass fraction of CO, Y_{CO}, and its derivatave at the surface, $dY_{CO}/dr\big|_S$, being known, equation (A71) can be written as

$$F = k_g \frac{\rho}{DM_{O_2}} Y_{CO} Y_{O_2}(Y_{CO}, r) \exp\left[-\delta_1/\tau(Y_{CO}, r)\right] - \frac{(1-\gamma)}{r}\frac{dY_{CO}}{dr} \qquad \text{(A84)}$$

This equation was solved using a Runge-Kutta technique, by defining

$$K1 = \Delta r F\left(R,\ Y_{CO},\ \frac{dY_{CO}}{dr}\right)$$

$$K2 = \Delta r F\left(R + \frac{\Delta r}{2},\ Y_{CO} + \frac{\Delta r}{2}\frac{dY_{CO}}{dr} + \frac{\Delta r K1}{8},\ \frac{dY_{CO}}{dr} + \frac{K1}{2}\right)$$

$$K3 = \Delta r F\left(R + \frac{\Delta r}{2},\ Y_{CO} + \frac{\Delta r}{2}\frac{dY_{CO}}{dr} + \frac{\Delta r K1}{8},\ \frac{dY_{CO}}{dr} + \frac{K2}{2}\right)$$

$$K4 = \Delta r F\left(R + \Delta r,\ Y_{CO} + \Delta r\frac{dY_{CO}}{dr} + \frac{\Delta r K3}{2},\ \frac{dY_{CO}}{dr} + K3\right)$$

$$Y_{CO} = Y_{CO} + \Delta r\left[\frac{dY_{CO}}{dr} + (K1 + K2 + K3)/6\right]$$

$$\frac{dY_{CO}}{dr} = \frac{dY_{CO}}{dr} + (K1 + 2K2 + 2K3 + K4)/6$$

The solution of equation (A84) gave values of the mass fraction of CO as a function of distance from the surface. The mass fractions of CO were then used in equations (A67), (A68), and (A69) to obtain the mass fractions of O_2 and CO_2 and the dimensionless temperature, τ, as a function of distance from the surface.

VII. BIBLIOGRAPHY

1. Fendell, F.E.: "The Burning of Spheres Gasified by Chemical Attack"; Combustion Science and Technology, Vol. 1, 1969, p. 3.
2. Ubhayakar, S.H. and Williams, F.A.: "Combustion and Extinction of Single Carbon Particles in Quiesent O_2/N_2 Mixtures"; Eastern States Section, The Combustion Institute, John Hopkins University, Maryland. November 12-13, 1979.
3. Ubhayakar, S.H. and Williams, F.A.: "Burning and Extinction of a Laser-Ignited Carbon Particle in Quiesent Mixture of Oxygen and Nitrogen"; Department of Applied Mechanices and Engineering Science, University of California, San Diego, La Jolla, California, 1978.
4. Hugo, P.; Wicke, E.; and Wurzbacher, G.: "Konzentrationsprofile vor Einer im Sauerstoffstrom Verbrennenden Kohlenstoffoverfläche - II. Berechnung der Konzentrationsprofile" ("Concentration Profiles in Front of a Carbon Surface Burning in a Flow of Oxygen. II. Calculation of the Concentration Profiles"); Int. J. Heat and Mass Transfer; Vol. 5, 1962, p. 929. (NASA TT F-16, 814, 1975.)
5. Wicke, E. and Wurzbacher, G.: "Konzentrationsprofile vor einer im Sauerstoffstrom verbrennenden Kohlenstoffoberflache. I. Experimentelle Ergebnisse" ("Concentration Profiles in Front of a Carbon Surface Burning in a Flow of Oxygen. I. Experimental

Results"; Int. J. Heat and Mass Transfer; Vol. 5, 1962, p. 277. (NASA TT F-16, 813, 1975).

6. Caram, H.S. and Amundson, H.R.: "Diffusion and Reaction in a Stagnant Boundary Layer About a Carbon Particle"; Ind. Eng. Chem. Fundam., Vol. 16, No. 2, 1977, p. 171.
7. Spalding, D.B.: "Combustion of Fuel Particles"; Fuel, Vol. 30, No. 6, 1951, p. 121.
8. van der Held, E.F.M.: "The Reaction Between a Surface of Solid Carbon and Oxygen"; Chem. Engng. Sci., Vol. 14, 1961, p. 300.
9. Field, M.A.; Gill, D.W.; Morgan, B.B.; and Hawksley, P.G.W.: Combustion of Pulverized Coal; The British Coal Utilization Research Association; Leatherhead, England, 1967.
10. Tu, C.M.; Davis, H.; and Hottel, H.C.: "Combustion Rate of Carbon, Combustion of Spheres in Flowing Gas Streams"; Industrial and Engineering Chemistry; Vol. 26, No. 7, July, 1934, p. 749.
11. Davies, T.W.; Beer, J.M.; and Siddall, R.G.: "The Use of a Mathematical Model for the Prediction of the Burn Out of Char Suspensions"; Chemical Engineering Science, Vol. 24, 1969, p. 1553.
12. Essenhigh, R.H.; Forberg, R.; and Howard, J.B.: "Combustion Behavior of Small Particles"; Industrial and Engineering Chemistry, Vol. 57, No. 9, September, 1965, p. 32.
13. Golovina, E.S. and Khaustovich, G.P.: "The Interaction of Carbon with Carbon Dioxide and Oxygen at Temperatures up to 3000^{o}K"; Eighth Symposium (International) on Combustion, pp. 784-792; The Williams and Wilkins Co., Baltimore, 1962.

14. Parker, A.S. and Hottel, H.C.: "Combustion Rate of Carbon, Study of Gas-Film Structure by Microsampling"; Industrial and Engineering Chemistry, Vol. 28, No. 11, November, 1936, p. 1334.

15. Kuchta, J.M.; Kant, A.: and Damon, G.H.: "Combustion of Carbon in High Temperature, High Velocity Air Streams"; Industrial and Engineering Chemistry; Vol. 44, No. 7, July, 1952, p. 1559.

16. Mulcahy, M.F.R. and Smith, I.W.: "Kinetics of Combustion of Pulverized Fuel: A Review of Theory and Experiment"; Rev. Pure and Appl. Chem., Vol. 19, 1969, p. 81.

17. Nettleton, M.A.: "Burning Rates of Devolatilized Coal Particles; Industrial and Engineering Chemistry Fundamentals"; Vol. 6, No. 1, February, 1967, p. 20.

18. Thring, M.W. and Essenhigh, R.H.: "Thermodynamics and Kinetics of Solid Combustion" in Chemistry of Coal Utilization, Supplementary Volume, H.H. Lowey, ed., Chapter 17. John Wiley and Sons, New York, 1963.

19. Froberg, R.: "The Carbon-Oxygen Reaction; An Experimental Study of Oxidation of Suspended Carbon Spheres"; Ph.D. Thesis, 1967, Penn. State University.

20. Matsui, K.; Koyama, A.: and Uehara, K.: "Fluid-Mechanical Effects on the Combustion Rate of Solid Carbon"; Combustion and Flame, Vol. 25, 1975, p. 57.

21. Arthur, J.R.: "Reactions Between Carbon and Oxygen"; Transaction of the Faraday Society, Vol. 47, 1951, p. 167.

22. Rhead, T.F.E. and Wheeler, R.V.: "The Combustion of Carbon"; Journal of the Chemical Society, Vol. 101.1, 1912, p. 846.

23. Blyholder, G. and Eyring, H.: "Kinetics of Graphite Oxidation"; J. Phy. Chem., Vol. 61, May, 1957, p. 682.

24. Kurylko, L.: "The Unsteady and Steady Combustion of Carbon"; 1969, Ph.D. Thesis, Penn State University.

25. Roberts, O.C. and Smith, I.W.: "Measured and Calculated Burning Histories of Large Carbon Spheres in Oxygen"; Combustion and Flame, Vol. 1, 1973, p. 123.

26. Gulbransen, E.A. and Andrew, K.F.: "Reactions of Artificial Graphite. Kinetics of Oxidation of Artificial Graphite at Temperatures of 425° to 575°C. and Pressures of 0.15 to 9.8 cm of Mercury of Oxygen"; Industrial and Engineering Chemistry, Vol. 44, No. 5, May, 1962, p. 1035.

27. Lewis, W.K.; Gilliland, E.R.; and Paxton, R.R.: "Low-Temperature Oxidation of Carbon"; Industrial and Engineering Chemistry, Vol. 46, No. 6, June, 1954, p. 1327.

28. Phillips, R.; Vastola, F.J.; and Walker, P.L., Jr.: "Factors Affecting the Product Ratio of the Carbon-Oxygen Reaction-II. Reaction Temperature"; Carbon, Vol. 8, 1970, p. 205.

29. Laine, N.R.; Vastola, F.J.; and Walker, P.L., Jr.: "The Importance of Active Surface Area in the Carbon-Oxygen Reaction"; Journal of Physical Chemistry, Vol. 67, October, 1963, p. 2030.

30. Wicke, E.: "Contribution to the Combustion Mechanism of Carbon"; Fifth Symposium (International) on Combustion, pp. 245-252; Reinhold Publishing Corp., New York, 1955.

31. Arthur, J.R.: "Combustion of Carbon"; Nature, Vol. 157, June 1, 1946, p. 732.

32. van Loom, W. and Smeets, H.H.: "Combustion of Carbon"; Fuel, Vol. 29, No. 5, 1950, p. 119.

33. Phillips, R.; Vastola, F.J.; and Walker, P.L., Jr.: "The Effect of Oxygen Pressure and Carbon Burn-off on the Product Ratio of the Carbon-Oxygen Reaction"; Carbon, Vol. 7, 1969, p. 479.

34. Walker, P.L., Jr.; Rusinko, F., Jr.; and Austin, L.G.: "Gas Reaction of Carbon"; Advance in Catalysis, Vol. 11, p. 133, Academic Press Inc., New York, 1959.

35. Kisch, D.: "Über den Temperaturverlauf vor im Sauerstoffstrom brennenden Graphitoberflächen" ("Temperature Profile of Graphite Surface Burning in a Stream of Oxygen"); Bunsengellschaft fuer physikalische chemie - berichte; v. 71, n. 1, 1967, p. 60. (NASA Technical Translation; NASA TM 75271, March, 1978).

36. de Graaf, J.G.A.: "Uber den Mechanismus der Verbrennung von festem Kohlenstoff" ("Mechanism of Combustion of Solid Carbon"); Brennstoff-Waerme-Kraft; vol. 17, no. 5, May, 1965, p. 227. (NASA Technical Translation; NASA TM 75274, March, 1978).

37. Draper, N.R. and Smith, H.: Applied Regression Analysis; John Wiley and Sons, Inc., New York, 1967.

38. Stearn, C.A. et al.: "A High Pressure Modulated Molecular Beam Mass Spectrometric Sampling System"; NASA TM 73720 (1977).

39. Mann, J.B.: "Ionization Cross Sections of the Elements" in Recent Developments in Mass Spectrometry, K. Ogata and T. Hoyakawa, Eds., pp 814-819, University Park Press, Baltimore, 1971.

40. Brabbs, T.A. et al.: "Shock Tube Measurements of Specific Reaction Rates in the Branched Chain H_2-CO-O_2 System"; Interna-

tional Symposium on Combustion, 13th; pp. 129–135, The Combustion Institute, Pittsburg, 1971.

41. Frank-Kamenetskii, D.A.: Diffusion and Heat Exchange in Chemical Kinetics; Princeton University Press, Princeton, New Jersey, 1955.